WAGENINGEN
UNIVERSITY & RESEARCH

Msc Thesis Meteorology and Air Quality

Evaluation of 1D and 3D simulations with CICE: sea ice thermodynamics and dynamics during the SHEBA expedition.

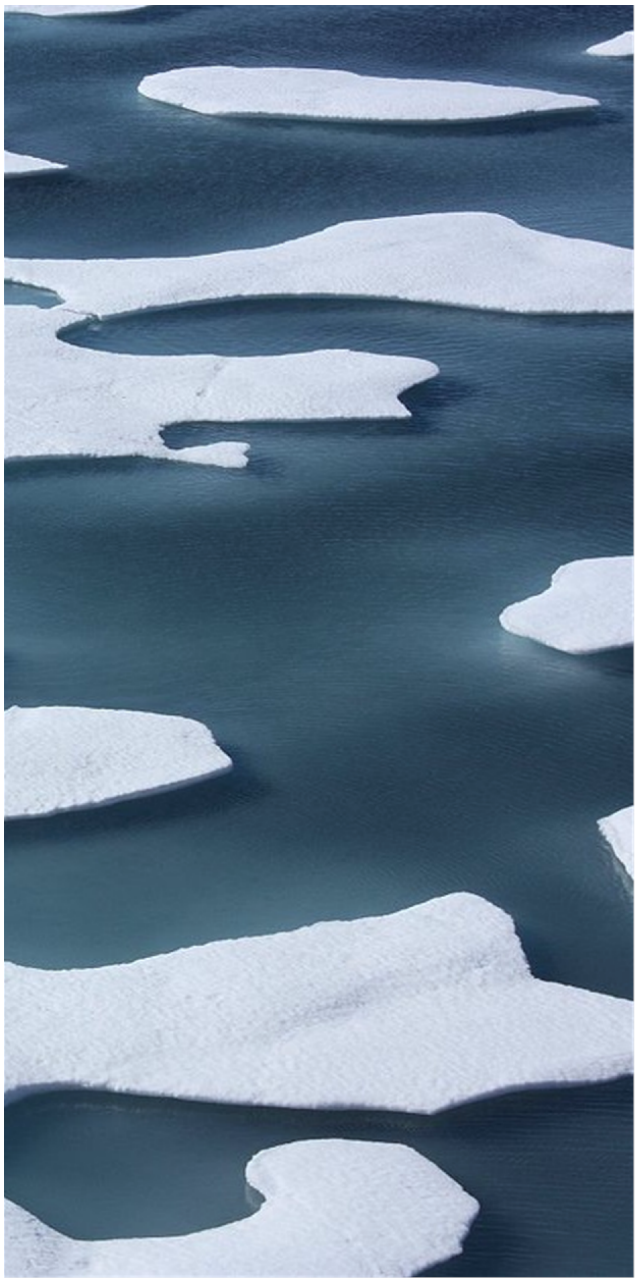

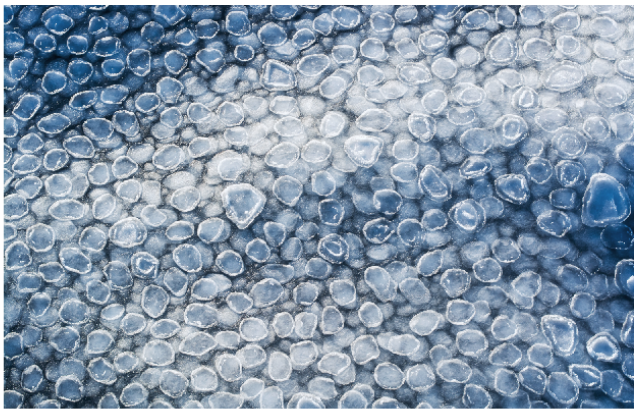

Author: Marte Hofsteenge
Supervisor: Laurens Ganzeveld

April 2020

Abstract

Observations in the Arctic have shown that sea ice plays a pivotal role in Arctic and global climate change, not only affecting sea-air interactions but also biochemistry. The already observed and further anticipated decline in sea ice will also affect the exchange of climate-active trace gases (CO_2, CH_4, O_3 and DMS), which is one of the foci of the Multidisciplinary drifting Observatory for the Study of Arctic Climate (MOSAiC) project. In this thesis we present a modelling study of sea ice processes that are relevant for climate-active trace gas exchange. We perform an evaluation and sensitivity study of the state-of-the-art Los Amalos Sea Ice Model (CICE) with a focus on the essential thermodynamic and dynamic processes driving this exchange. The simulated one- and three-dimensional ice fields are evaluated for the period of the Surface Heat Budget of the Arctic Ocean (SHEBA). The 1D simulations show a simulated ice thickness evolution that agrees well with the SHEBA observations (RMSE 0.34 m), however they also show their sensitivity to the atmospheric forcing data. Using climate-model derived forcing data instead of local observations shows the strong impact of snowfall on ice growth, albedo, onset of the melt season and, consequently, total surface melt. Besides, including ice opening rates in the 1D simulation increased the bottom and lateral melt with 11 and 30 cm/yr respectively. Subsequently, the 3D simulated Arctic ice field agrees on average well with satellite-derived ice concentrations (RMSE of 0.1), but shows larger differences in the marginal ice zone around Svalbard and Greenland. The ice concentration shows a strong sensitivity to the oceanic forcing data where the restoring timescale of sea surface temperature strongly controls the formation of new ice. Both the 1D and 3D simulations show that simulated melt pond areas are significantly different when using different parameterizations, influencing in turn the summer albedo and surface melt. Our results show that important features for climate-active trace gas exchange such a open water fractions and ponds are represented well in CICE, though being very sensitive to the forcing data sets and choice of parameterizations. As such, this study has provided valuable information regarding the required data to optimally constrain CICE simulations for its potential follow-up application studying sea ice biogeochemistry and climate-active trace gas exchange as observed in the MOSAiC field campaign.

Contents

1 Introduction

The fast decline in sea ice is one of the clearest indicators of global climate change. Passive microwave satellite records from 1978 show us a linear decreasing trend in sea ice extent for all months, but strongest for September (Serreze and Stroeve, 2015). The average sea ice thickness is decreasing with a similar trend, due to strong loss of the thickest and oldest ice (Maslanik et al., 2007). The thicker multiyear sea ice is increasingly replaced by thinner, young sea ice (Maslanik et al., 2007). These changes in sea ice thickness affect the surface energy balance and melt and growth rates of the sea ice (Hunke et al., 2010). Additionally, since sea ice forms the interface between the ocean and the atmosphere in the Arctic region, changes in the sea ice distribution, age and thickness have possible effects on the exchange of gas between the Arctic Ocean and atmosphere.

Sea ice was in the past yet wrongly seen as a uniform cover that acts a barrier for gas exchange between the Arctic ocean and the atmosphere. However, observations and modelling studies from the last decade show a different picture with an important role of sea ice in exchange of active climate trace gases. Not only is sea ice itself permeable to gases under warm enough temperatures (Geilfus et al., 2012), but also increased gas fluxes were observed over cracks and small leads in the ice (Steiner et al., 2013). Also Else et al. (2011) found that gas exchange is enhanced in polynyas as a result of rapid sea ice formation in these persistent open area in the ice pack.

In addition to the ice pack that can provide pathways for gases, also active processes in the sea ice play a role in the climate-active trace gas exchange. For example, different studies discuss the role that sea ice might play in the carbon cycle. Observations give indication of release of CO_2 from sea ice in summer (Miller et al., 2011) and a uptake in winter/fall (Else et al., 2008; Vancoppenolle et al., 2013). A conceptual model was introduced by Rysgaard et al. (2011) that involved active processes in a biogeochemical sea-ice carbon pump that affect the net ocean-atmosphere CO_2 exchange. In this sea-ice carbon pump, dissolved inorganic carbon is released by brine drainage into the sea water, which is transported by dense waters to the deeper ocean, causing changes in surface water pCO_2 and consequently the CO_2 fluxes into the atmosphere from open leads and other exposed ocean surface (Fig 1.1).

Besides the role of sea ice in the carbon cycle, sea ice processes appear to play a role in the sulfur cycling in the Arctic as well. High concentrations of dimethylsulfoniopropionate (DMSP) in ice were found with ice-core measurements in the Arctic and Antarctica (Kirst et al., 1991; Levasseur et al., 1994). Micro-algae in the sea ice produce these high concentrations of DMSP, the precursor of dimethyl sulfide (DMS), which has an effect on the oceanic emission of DMS into the atmosphere (Fig 1.1). DMS is a precursor of sulphate aerosol that can have a cooling effect on earth. More recent research by Gourdal et al. (2018) in the Canadian Arctic Archipelago and by Park et al. (2019) in the Northern Arctic Ocean show high DMS observations in melt ponds, which are strongly linked to seawater intrusion in the ponds. How large the contribution of sea ice to the global DMS emissions is still unknown. (Vancoppenolle et al., 2013)

A third important compound for which we need to consider the anticipated changes in Arctic sea ice cover is the strong green house gas methane (CH_4). It is emitted from the Arctic Ocean, released from the thawing permafrost in the East Siberian Arctic Shelf (ESAS) (Shakhova et al., 2015). In the shallow ocean at the ESAS ($\sim$50m), methane bubbles have a short distance to travel to the surface and are released to the atmosphere under conditions of open water and increased mixing (Shakhova et al., 2015). Kort et al. (2012) found another source of methane with comparable emission rates in the Chuckchi and Beaufort Sea, far away from the ESAS. Kort et al. (2012) found highest concentrations of methane over fractional sea ice and open water. That this methane could have been advected from the ESAS was not excluded. Damm et al. (2018) denotes the Transpolar Drift as crucial for the transport of methane from the ESAS to other polar surface waters, where they are released when the ice cover melts.

Finally, another important climate-active trace gas for which we also need to consider changes in sea ice cover is ozone (O_3). Ozone is the third most significant greenhouse gas, but also a key atmospheric oxidant affecting the concentration of many atmospheric compounds such as DMS (Forster et al., 2007; Boucher et al., 2003). The Arctic Ocean is deemed posing a sink for O_3 through the effective uptake by ocean water as a function of its reaction with halogen compounds such as Iodide, but also reacting with Dissolved Organic Matter (DOM) and other reactants including DMS (Ganzeveld et al., 2009). Sea ice cover inhibits this ocean deposition process but instead offers a reactive chemistry vessel associated with the processing and release of reactive nitrogen and halogen species that can very efficiently destroy ozone (so-called Ozone Depletion Events, ODEs). The exponential increase in these reactive halogen compounds resulting in ODEs is known to be associated to a strong source of bromine monoxide (BrO) in spring from first-year sea ice, because of it's high content in brine (Simpson et al., 2007; Vancoppenolle et al., 2013).

To further understand the biochemical cycling in sea ice, several scientist coupled biochemical ocean and sea ice models. Jin et al. (2012) used a coupled set-up of an ecosystem model with the 3D ocean-ice POP-CICE model to understand the sea-ice primary

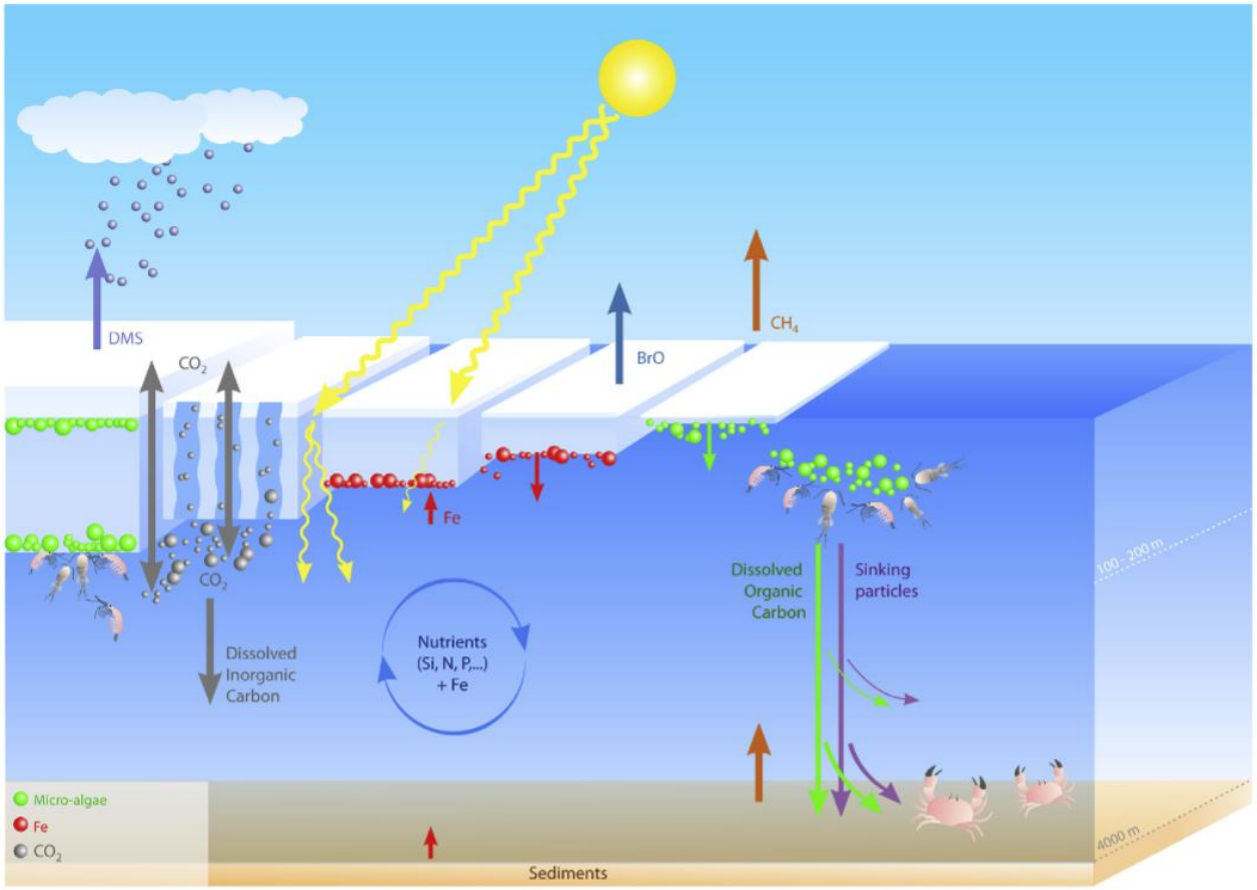

Figure 1.1 | Schematic overview of biogeochemical processes in Arctic sea ice. (Vancoppenolle et al., 2013)

production. The earlier mentioned sea-ice carbon pump introduced by Rysgaard et al. (2011) was tested in two different model set-ups; Moreau et al. (2016) confirmed the carbon pump using the coupled NEMO-LIM-PISCES[1] model, but found much smaller amounts of carbon that were transported to the deep ocean. A related study by Grimm et al. (2016) using another ocean-sea-ice-biogeochemical model (MPIOM/HAMOCC[2]) gave comparable results. Both studies show that the sea-ice carbon sink is small compared to the global ocean CO_2 sink, but can be relatively large on the regional scale.

Not only the carbon biochemistry, but also the sulfur cycling in sea ice is studied with coupled biochemical ice-ocean models. Elliott et al. (2012) coupled geochemical and ecological cycles to the CICE model to study the impact of the bottom ice-layers on the surface ocean DMS. Hayashida et al. (2017) used a 1D model set-up to study the DMS cycling in sea ice and found that including the sea-ice sulfur cycle resulted in 20-26% increase of sea-air DMS fluxes during melt.

No modelling studies have been published yet on the simulation of methane bubbles and their release through the sea ice zone.

While ice-ocean coupled models are used to study sea ice biochemistry and resulting exchange fluxes, little studies use coupled sea ice and atmospheric chemistry models to study the impact on regional and global climate. To understand the impact of changes in Arctic sea ice and biochemistry on regional and global climate, we need models with coupled atmosphere, ocean, sea ice and land components. Global chemistry-climate models can be used for this purpose, but have as disadvantage that they resolve all relevant processes at a rather coarse resolution (~200 km). Mesoscale models such as WRF (Weather Research and Forecasting model) have a finer resolution (~10-25 km). Versions of WRF adapted for the polar regions (POLAR-WRF, Bromwich et al. (2009)) and coupled atmospheric chemistry (WRF-CHEM, Grell et al. (2005)) are therefore very suitable to study the exchange of climate-active trace gases in the Arctic.

However, complex sea ice processes that are important for gas exchange in the Arctic seem to be relatively poor represented in models such as PWRFC (POLAR-WRF-CHEM). The absence of a proper representation of relevant sea ice processes in models like PWRFC may result in some shortcomings in the

[1] Coupled model set up of the ocean modelling system NEMO together with the sea ice component Louvain-la-Neuve Ice Model (LIM2), and a marine biogeochemical component of the Pelagic Interaction Scheme for Carbon and Ecosystem Studies (PISCES)

[2] Max Planck Institute global ocean-sea-ice general circulation model MPIOM coupled to the Hamburg ocean carbon cycle model HAMOCC

representation of the polar regions in global climate, not only relevant to assess its role in the exchange of climate-active trace gases but also given the relevance of sea-ice for the exchange of energy, momentum and water vapor (Yao et al., 2016).

Other versions of WRF have been coupled to complex sea ice models. Yao et al. (2016) for example improved the POLAR-WRF model by coupling it to the HIGHTSI sea ice model, which greatly improved the simulation of sea ice temperature. However, HIGHTSI did not add any sea ice dynamics to the model, which are crucial to simulate for example the formation of leads and it's impact on gas exchange. Liang et al. (2004) coupled the CICE model to the Climate extension of WRF, to improve simulations of the surface heat budget and climate change over the Arctic. Couplings of complex sea ice models with the WRF-CHEM model are although not done yet. Coupling of WRF-CHEM with CICE might be an essential step to apply this system for studies focussing on the simulation of active trace gas exchange in the Arctic.

For this reason, this research will focus on the modelling of relevant sea ice processes for gas exchange in sea ice, mainly relying on application of the CICE modelling system. The relevant sea ice processes as explained in the background section can be subdivided in three type of processes: thermodynamic- (e.g. ice growth, pond formation, brine release), dynamic- (e.g. formation of leads) and biochemical processes (e.g. algal bloom, transport of nutrients). Given time constraint of this thesis study, we will focus on thermodynamic and dynamic processes.

This study is part of the international Multidisciplinary drifting Observatory for the Study of Arctic Climate project (MOSAiC). The MOSAiC project provides year-long measurements of climate-active trace gas exchange in the Arctic. Modelling studies within the MOSAiC project (i.a. using PWRFC) will support analysis of the measurements and will be used to assess the impact of the measured gas exchanges on larger scales. The results of this research will be a step in improving simulations with PWRFC, possibly coupling it in the future to a complex sea ice model such as CICE, to assess the role of Arctic climate-active trace gas exchange in Arctic- and global climate.

The aim of this study is to evaluate the CICE simulated thermodynamic and dynamic sea ice processes that ultimately drive climate-active trace gas exchange in the Arctic. Therefore I state the following research questions:

- To what extent does CICE represent the relevant sea ice processes for active trace gas exchange?
  - How well does CICE represent the growth and melt of sea ice for a full seasonal cycle?
  - How well does CICE simulate the lead formation in the sea ice cover?
  - How well does CICE simulate the evolution of melt ponds? And what is the impact of the different melt pond schemes on the melt pond characteristics and surface albedo?
- What is the influence of atmospheric and oceanic forcing on the sea ice simulation?
- Which steps should be taken to incorporate the role of sea ice in the simulation of climate-active trace gas exchange in the Arctic?

2 Methodology

2.1 Model description

The Los Alamos Sea Ice Model (CICE) was developed to create an efficient sea-ice component for a fully coupled atmosphere-ice-ocean-land global climate model (Hunke et al., 2019a). The CICE model has different interactive components: an ice dynamics model, a transport model and a sub module 'Icepack' that simulates all vertical processes in CICE. This Icepack module (Hunke et al., 2019b) is used as a stand-alone model during the first part of this study, which is focused on understanding and evaluating the sea ice processes in a 1D model set-up. Then in the second part of this study, the CICE model including the Icepack model for the vertical processes is used for the three-dimensional simulations.

The underlying equation that is solved by the CICE model is (Thorndike et al., 1975):

$$\frac{\partial g}{\partial t} = -\nabla \cdot (g\mathbf{u}) - \frac{\partial}{\partial h}(fg) + \psi - L, \qquad (2.1)$$

where $\mathbf{u}$ represents the horizontal ice velocity vector (m/s), f the thermodynamic ice growth (m/s), ψ redistribution by ridging (s^{-1}), L lateral melt (s^{-1}) and g the ice thickness distribution function (-). Here g is the fractional area covered by ice in a thickness range $(h, h+dh)$. All terms are represented in Icepack, with the exception of the divergence term $-\nabla \cdot (g\mathbf{u})$ that is calculated in the CICE model components. For this reason there are no horizontal transport processes represented in simulations with Icepack alone.

We will first describe the vertical model component Icepack (section 2.1.1), followed by a description of the additional model components in the three-dimensional CICE model (section 2.1.2).

2.1.1 Icepack

Icepack is configured with 4 tiles that have different sea ice conditions (open water, slab ice with a homogeneous ice thickness without snow, a full ice thickness distribution (ITD) and land, Figure 2.1a). For all tiles the same forcing data is applied and there is no exchange between the 4 tiles. Only the diagnostics of the full-ITD tile are considered in this study. A description of the most important model components of Icepack follows here.

Ice thickness distribution
Sea ice packs in the Arctic contain a mixture of thin first year ice, thicker multi-year ice and thick pressure ridges. In order to simulate the dynamical and thermodynamic response of such a diverse ice pack, an ice thickness distribution is used in Icepack (Figure 2.1b). Snow and ice are represented in multiple layers and ice thickness is distributed in categories using the remapping scheme of Lipscomb (2001). We use 5 ice thickness categories, 7 layers to represent the ice and 1 layer to represent snow.

Thermodynamics
The energy-conserving thermodynamical model calculates ice growth and melt rates by snow-ice formation and vertical conductive, radiative and turbulent heat fluxes (Bitz and Lipscomb, 1999). Snow depth increases by snowfall and decreases due to snow melt or sublimation. Redistribution of snow by wind is not represented in Icepack. Melt and growth is computed in Icepack after updating the ice and snow temperatures. The temperatures are calculated such that the surface temperature cannot exceed 0°C and the temperature at the bottom of the ice is always at freezing temperature of the water. Ice temperatures are calculated per layer as a result of heat conduction from the temperature gradient between the surface

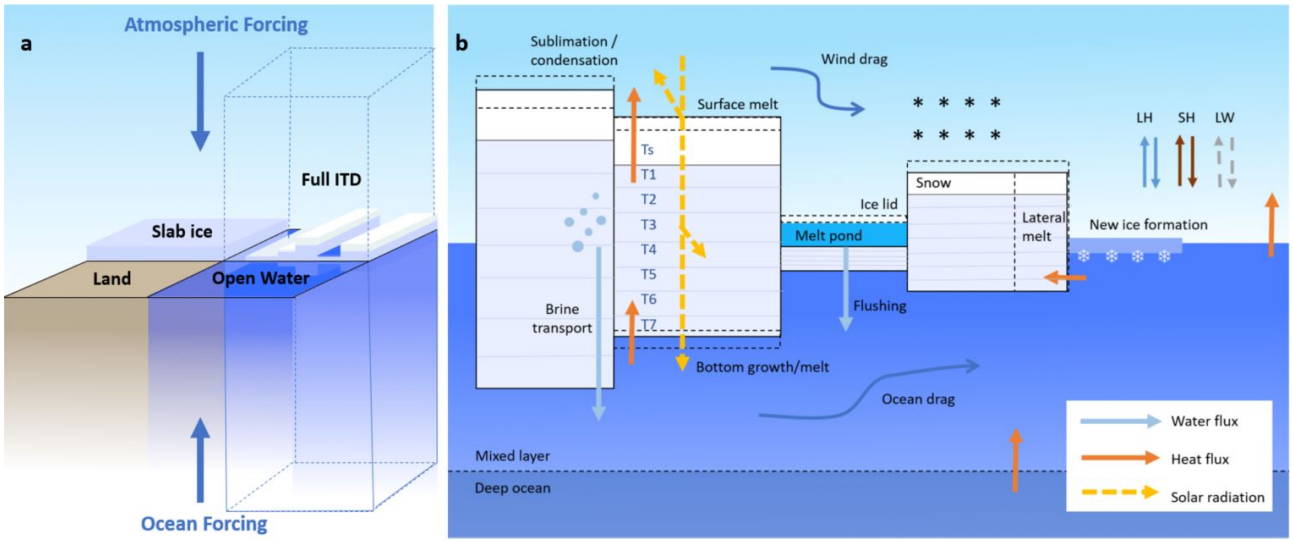

Figure 2.1 | Schematic overview of the Icepack model. In **a)** the columnar model set-up, with 4 tiles representing land, open water, slab ice (without snow) and a full ITD and **b)** the most important vertical processes represented in Icepack when using the ITD.

and bottom, vertical advection of heat by drainage and the absorption of shortwave radiation in the ice.

For every ice and snow layer the enthalpy (defined as the negative of energy required to melt ice and raise its temperature to 0°C) is calculated from the temperature and salinity of the ice. The calculated enthalpy in snow and ice is used to calculate the growth/melt rates. We use the "mushy" thermodynamic scheme that treats the ice as a mushy layer (Feltham et al., 2006), a matrix of pure ice that contains pockets of salty melt water (brine).

Growth and melt at the bottom of the ice is calculated by:

$$q\,\delta h = (F_{cb} - F_{bot})\,\Delta t, \tag{2.2}$$

where q is the enthalpy (J/m^3), δh the change in ice thickness (m), F_{cb} the conductive heat flux arising from the temperature gradient in the ice and F_{bot} the heat flux between the ice/ocean interface (W/m^2). This results in ice growth when the heat conduction to the surface is greater than the heat input from F_{bot}, and similarly ice melt when the heat input F_{bot} from the ocean is larger than the heat that can be conducted away to the surface. For surface melt counts:

$$q\,\delta h = \begin{cases} (F_0 - F_{ct})\,\Delta t & \text{if } F_0 > F_{ct} \\ 0 & \text{otherwise} \end{cases} \tag{2.3}$$

where F_{ct} is the surface conductive flux and F_0 is the net surface flux calculated from the sensible and latent heat flux, longwave radiation and part of the shortwave radiation which is not reflected or penetrated through the ice ($F_0 = F_{SH} + F_{LH} + F_{LW\downarrow} + F_{LW\uparrow} + (1-\alpha)\cdot(1-i_0)F_{SW}$).

Solar radiation
Solar radiation is able to penetrate through both snow and ice layers, with attenuation of the radiation by Beer's law (CICE Consortium, 2019). Two options are available for albedo description. The default option has an albedo described as in the Community Climate System Model, Version3 (CCSM3), depending on surface temperature, air temperature, thickness of snow and ice and the spectral distribution of incoming solar radiation. The second option is based on application of a multiple scattering radiative transfer scheme that uses the Delta-Eddington approach (Briegleb and Light, 2007). This approach calculates the absorption, scattering and transmittance of radiation in the snow and ice. Absorptive effects of carbon soot, salts, algae and snow aging can be included using this approach. The Delta-Eddington approach is also required to simulate the effect of melt-ponds and therefore used in our simulations.

Melt ponds
Formation of melt ponds on ice is simulated considering pond area and depth through the entire simulation. When the top of the pond refreezes and snowfall on top of the refrozen lid blocks solar radiation, the 'effective pond area' that is used for the radiation calculations can decrease while the pond volume remains. The effective pond area is therefore what influences the sea-ice albedo. Three different schemes are available in Icepack to explicitly model melt ponds.

The first basic pond scheme is made for the Communitiy Earth System Model (CESM, known also as the Community Climate System Model). In the CESM scheme, ponds can grow when rain or (snow and ice) melt water is added and shrink through refreezing. The melt pond processes are described empirically in this scheme and pond depth and area are linearly related. The second pond scheme is the topographic scheme (topo, Flocco and Feltham (2007)), which simulates the concept that melt water collects on the lowest parts of the ice. Since Icepack does not explicitly model ice topography, the ice thickness distribution is split into a surface height and basal depth distribution relative to sea level. Melt water is thereafter collected on the ice of the lowest surface height. In this scheme pond water can refreeze (affecting the effective pond area) and drain vertically when the sea ice becomes permeable. The last pond scheme, the level-ice formulation (Hunke et al., 2013) accounts for gravity effects too, but in an innovative way where ponds can only form on the level (undeformed) ice areas per ice category. In the level-ice scheme, melt pond water can also refreeze and drain to the ocean, depending on the permeability of the ice.

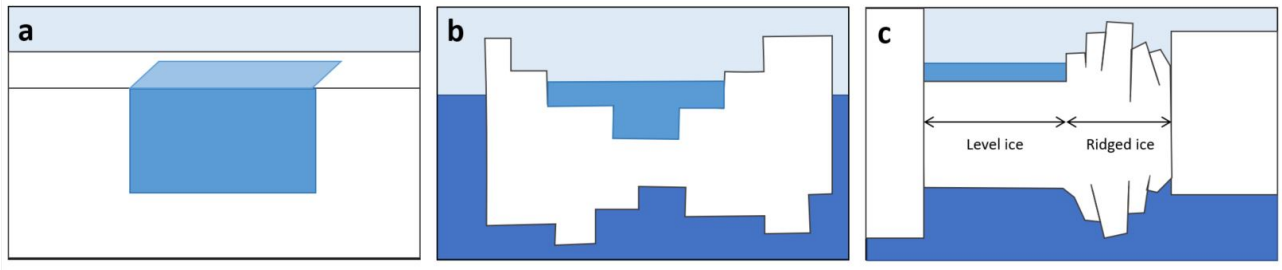

Figure 2.2 | Schematic representation of the melt pond parameterizations a) CESM pond scheme, which is and emperical scheme that assumes a fixed pond depth - area ratio **b)** Topo pond scheme that simulates the topographic effects of sea ice **c)** Level pond scheme where melt water collects on the level ice fractions.

Ocean
Icepack contains an optional thermodynamic slab ocean mixed-layer parameterization, to use when running the model without coupling to an ocean model. In this parameterization sea surface temperature (SST) is calculated using the surface energy balance above the ocean water and the heat flux from below the surface layer (Figure 2.1b). The net surface flux F_0 is calculated as shown above from the turbulent, longwave and shortwave fluxes. When the simulated SST reaches the freezing temperature, frazil ice crystal growth is simulated. When there is open water present, this new ice is added as a uniform layer of 5 cm thick ice. When no open water is present this is added equally to all ice categories. This ice formation is referred to as 'new ice formation'.

Heating/cooling of the SST through exchange with the deeper ocean depends on the given forcing data of mixed layer depth and deep ocean heat flux. The freezing temperature of the water depends on the sea surface salinity (SSS) from forcing data. The simulated SST can be restored to given SST data. This means that the simulated SST is forced towards the input SST data. The strength of the restoring and therefore how quickly the SST heads toward the data depends on the restoring timescale. In all our runs the slab ocean parameterization is switched on.

Mechanical redistribution
The second last term ψ on the right of equation 2.1 is represented in a scheme for mechanical redistribution. The scheme fills open water with sea ice and converts thin ice to thicker ice due to ridging under convergence. The scheme computes opening of the ice as a result of divergence. Ice volume and internal energy is conserved, while the ice area can decrease through ridging. Formation of ridges and keels in turn has effect on the atmosphere and ocean drag. Mechanical redistribution is described in the Icepack code, however the redistribution is linked to the dynamics scheme in CICE (see section 2.1.2) via the computed internal stress and therefore no ridging can occur in one dimensional simulations with Icepack.

Biochemistry
In addition to the column physics, Icepack contains also a representation of vertical biochemical cycling in the ice/snowpack including the role of algae, nutrients and aerosols (Jeffery et al., 2016). Aerosols such as black carbon and dust that are deposited on snow and ice can be transported through the ice via brine drainage processes. The sea ice ecosystems can be simulated with a multi-layer biogeochemical model, which uses among others diatom, phytoplankton, iron, DMSP, nitrate, ammonium and silicate as tracers. The biochemistry is though not considered in this study because of time limits. However, given that this thesis study has been motivated as a contribution to the MOSAiCs project on measurements and modelling of climate-active trace gases also as a function of sea ice biochemical processes, this package provides a promising basis to be further explored in follow-up studies that focus on this modelling of climate-active trace gas exchange through sea ice.

2.1.2 CICE

For three-dimensional simulations we use the CICE model. Within CICE, the vertical processes are still simulated with the Icepack code. We describe here the horizontal processes that are represented in the CICE code.

Horizontal transport
In CICE ice and snow layers can be transported in the horizontal domain as a result of the ice velocity field. A remapping routine is designed to transport the ice over grid cells. This remapping scheme uses conserved ice tracers that are transported with the ice, such as ice volume, salinity, enthalpy, pond area, ice age and fraction of level (undeformed) ice.

Ice dynamics
The balance of forces on the sea ice is solved with a momentum equation

$$m\frac{\partial \mathbf{u}}{\partial t} = \nabla\cdot\sigma + \vec{\tau}_a + \vec{\tau}_w + \vec{\tau}_b - \hat{k}\times mf\mathbf{u} - mg\nabla H_\circ \quad (2.4)$$

where m is the total mass of ice and snow per area (kg), and $\frac{\partial \mathbf{u}}{\partial t}$ the tendency of the horizontal velocity vector (m/s^2). The equation represents ocean and wind stresses $\vec{\tau}_a$ and $\vec{\tau}_w$ (N), seabed stress in shallow water $\vec{\tau}_b$ (not represented in our simulation since no bathymetry is used) and internal stress in the ice σ_{ij} (i and j indicating different components of the stress tensor). The last two terms represent stresses due to Coriolis effects and the tilting of the sea surface. The internal stress is calculated by a chosen rheology; descriptions how internal ice stress and deformation are related. In this study we use the elastic-visouc-plastic (EVP) model (Hunke and Dukowicz, 1997). The EVP model is an adjustment of the viscoplastic rheology (VP) by Hibler (1979). Using VP rheology, ice has viscous behaviour under small deformation rates and has plastic behavior for large deformation rates. In the EVP rheology an elastic term is introduced in the internal stress tensor σ_{ij}, which has as advantage that it is a simple formulation that can be solved with an explicit integration scheme.

2.2 1D Icepack simulations

All simulations in this study are focused on the period October 10th 1997 - October 10th 1998, for which extensive measurements in the Beaufort Sea are available from the Surface heat budget of the Arctic Ocean (SHEBA, Uttal et al. (2002), Figure 2.3a). For this expedition the ice breaker *Des Groseilliers* was

positioned in an ice floe and measurements were made from the SHEBA ice camp that drifted for a full year in the ice. This expedition offers a unique data-set of meteorologic, oceanic and ice measurements that will be used in this study as forcing and evaluation data.

The first part of the study focuses on 1D simulations with Icepack version 1.1.1 (Hunke et al., 2019b). In our 1D analysis we are mainly interested in assessing the role of thermodynamical processes, since dynamical processes related to horizontal transport are not represented in these 1D simulations. First we will discuss how the simulations have been initialized (Section 2.2.1), then the data sets that are used to force the Icepack runs (Section 2.2.2) and finally the different simulation experiments with Icepack (Section 2.2.3). Figure 2.3 shows the location of the SHEBA expedition and also a summary of the simulation set-up that will be discussed here.

2.2.1 Initialization

To start a simulation for the SHEBA expedition having most realistic initial conditions, we planned to do restart simulations from spin-up of different lengths (1990-1997 and 1980-1997). These spin-up runs used as meteorological forcing data 6h-hourly forecast from the European Centre for Medium range Weather Forecast (ECMWF). The oceanic forcing data was obtained from reanalysis from the Simple Ocean Data Assimilation (SODA, Carton and Giese (2008)) based on the Parallel Ocean Program POP model (TAMU/UMD, 2020). Details on the required forcing fields will be discussed in the following section. These spin-up simulations were initialized from an ice pack of which ice of 3 m thick covers the largest area, which gives an average initial ice thickness of 2.6 m.

For both spin-up periods, the ice opened up almost completely in summer within 5 years. These spin-up results were unrealistic, since it is known from the SHEBA expedition that the area has multi-year sea ice. For this reason the SHEBA run is not initialized from a restart but run from 1st of January 1997, from an initial ice thickness with the same average ice thickness of 2.6 m. Running a short simulation like this has as limitation that there is no representation of multi-year ice. The importance of simulating multi-year ice lies in the fact that multi-year ice has gone through deformation mechanisms for a long time, altering the thermodynamic behavior of the sea ice. However, since there is in these 1D simulations no vertical transport and resulting deformation, the simulation of multi-year ice is less important in this 1D set-up. For this reason, a set initial sea ice condition rather than a restart from spin-up is sufficient for our 1D model runs.

Hence, in stead of restarting the 1D simulations from a spin-up simulation, the Icepack simulations are run only for 1997 and 1998. From the start of 1997 until August 1997 the forcing data is provided by the above mentioned 6h ECMWF forecast and monthly POP data. In this study we only focus on the SHEBA expedition period (Oct 1997 - Oct 1998) for the evaluation. The simulation results in an ice thickness of 1.7 m at the start of the SHEBA-expedition (October 1997). This agrees well with the mean ice thickness of 1.5 m measured by sub-marine surveys by Perovich et al. (2003) at the start of the expedition. The following section describes the forcing data used for the SHEBA expedition period.

2.2.2 Forcing

In contrast to the period prior to the SHEBA expedition where forcing data is based on ECMWF and POP data, for the SHEBA period the forcing data is based on local observations of the SHEBA expedition. The atmospheric forcing field consists of 2-m temperature, 10-m wind speed and direction, 2-m specific humidity, incoming shortwave and long wave radiation and precipitation (Table 2.1). The atmospheric observations we use were measured on the meteorological tower 'Met City' of the SHEBA Atmospheric Surface Flux Group (ASFG). The ASFG atmospheric data was provided with hourly intervals and had a data coverage larger than 98% for all needed measurements. The missing data points were linearly interpolated. Zonal and meridional wind components were calculated from wind speed and direction.

The oceanic forcing field consist of SST, SSS and zonal and meridional ocean velocities. The SST and SSS data for the SHEBA expedition is based on daily averaged CTD (Conductivity, Temperature, Depth) observations from the SHEBA observatory (Stanton and Shaw, 2007). A depth of 4.5 meter was chosen for the measurements, in order to still represent surface water conditions, while minimizing the missing values in the measurements. The data coverage was 88% and missing data are filled by linear interpolation. The data was resampled to hourly values with linear interpolation.

The ocean velocities in the zonal and meridional for the forcing field were obtained from the Ocean Turbulent Mast measurements (McPhee, 2007). The relatively low coverage (73.94%) is mainly caused by sizable gaps in February and March due to breakup of the ice camp and redeployment of the measurement equipment. The irregular ocean turbulent mast data was averaged to daily intervals and missing values were filled by linear interpolation. The ocean measurements of the CTD and Ocean Turbulent Mast site agree well (correlation of SST and SSS was 0.98 and 0.99, respectively). This demonstrates that the ocean data from these two different field sites are consistent and can be combined in a forcing data set for Icepack.

Table 2.1 | Icepack forcing data. Overview of forcing data fields used for the Icepack simulation for the SHEBA expedition period (Oct 1997 - Oct 1998). Variables and units are given as required to force Icepack. Frequency represents the measurement frequency, before all data is converted to hourly time-steps.

Variable	Unit	Data source	Frequency	Start	End	Coverage
2-m temperature	[K]	ASFG Fluxtower	hourly	Oct 09 '97	Oct 08 '98	98.3 %
10-m zonal wind	[m/s]	ASFG Fluxtower	hourly	Oct 09 '97	Oct 08 '98	98.5 %
10-m meridional wind	[m/s]	ASFG Fluxtower	hourly	Oct 09 '97	Oct 08 '98	98.5 %
Incoming shortwave radiation	[W/m^2]	ASFG Fluxtower	hourly	Oct 09 '97	Oct 08 '98	99.2 %
Incoming longwave radiation	[W/m^2]	ASFG Fluxtower	hourly	Oct 09 '97	Oct 08 '98	98.1 %
Specific humidity	[kg/kg]	ASFG Fluxtower	hourly	Oct 09 '97	Oct 08 '98	98.3 %
Precipitation	[mm/s]	Snow gauge, SPO corrected [3]	hourly	Oct 29 '97	Oct 02 '98	92.1 %
Sea surface temperature	[K]	CTD	daily	Oct 12 '97	Sep 21 '98	88.7 %
Sea surface salinity	[ppt]	CTD	daily	Oct 12 '97	Sep 21 '98	87.6 %
Zonal ocean velocity	[m/s]	Ocean Turbulence Mast	hourly	Oct 09 '97	Sep 28 '98	73.9 %
Meridional ocean velocity	[m/s]	Ocean Turbulence Mast	hourly	Oct 09 '97	Sep 28 '98	73.9 %

The SHEBA expedition offers a unique data-set, as it is the only available data set up til now that gives atmospheric, oceanic and ice data for a full seasonal cycle. Drobot et al. (2003) studied the representativeness of the data set and concluded that the local atmospheric measurements are well representing the larger domain. On the other hand, with exception of the surface pressure, the measurements did not represent the climatological values but rather an extreme year. Most unusual of the SHEBA year was the low amount of very cold days (Drobot et al., 2003). An overview of the forcing fields for the SHEBA expedition period is shown in Table 2.1.

2.2.3 Experimental design

Next to a control run, we run different simulations to test the sensitivity of the model to different model settings and forcing data sets. A first experiment consists of runs with different schemes for melt-pond calculations (Table 2.2) to study the impact of these schemes on simulated pond fractions and albedo. To investigate the impact of the scale difference between local measurements from the SHEBA observatory and model derived meteorology, we did simulations with different forcing data sets. One run uses the ECMWF column model output for SHEBA that was provided by Bretherton (2007), into which rawinsonde and surface synoptic observations from SHEBA were assimilated. The second run uses the atmospheric forcing data set provided by the Coordinated Ocean-ice Reference Experiment (CORE), which was developed by Large and Yeager (2008) at the National Center for Atmospheric Research (NCAR) and is used to force CICE in the 3D simulations (CICE-Consortium, 2020a). Figure 2.3a shows the SHEBA drift track together with location of the ECMWF and NCAR grid points.

Since this stand-alone run with Icepack does not involve any horizontal transport and resulting divergence, one experiment is focused on the impact of opening and closing of the ice cover. For this run

[3]SHEBA Project Office made corrections on the snow gauge data for wind, blowing conditions and losses due to evaporation and gauge wetting

Table 2.2 | Icepack experiments. Settings for the control run and experimental simulations.

Label	Pond scheme	Atm Forcing	Open rates	SST-restoring	Description
CNTL	level	SHEBA	no	no	Control run
TOPO	topo	SHEBA	no	no	Topo pond scheme
CESM	CESM	SHEBA	no	no	CESM pond scheme
ECMWF	level	ECMWF	no	no	Forced with ECMWF meteorology
NCAR	level	NCAR	no	no	Forced with CORE NCAR meteorology
OPEN	level	SHEBA	yes	no	With opening and closing rates
RSST	level	SHEBA	no	yes	Sea surface temperature is restored on a daily timescale.

an additional forcing data set is used with opening and closing rates for the SHEBA site computed by Stern and Lindsay (2000) (CICE-Consortium, 2020b). Lastly, we did a simulation in which the SST is restored on a daily timescale. In the control run the SST is purely based on the slab-ocean mixed layer parameterization. In contrast, the simulated SST is now nudged towards the observed under-ice water temperatures from CTD measurements, to study the bias of the slab-ocean model in Icepack.

2.3 3D CICE simulations

The second part of this study focuses on the 3D simulations with CICE version 6.0.1 (Hunke et al., 2019a), configured identical for parameters that overlap with the Icepack model. For the 3D simulations we focus again on the same period of the SHEBA expedition. A global 1 degree gx1v3[4] grid is used with displaced pole over Greenland. We focus in this study only on the results for the Arctic.

[4]third version of the 1° global grid of the POP ocean model

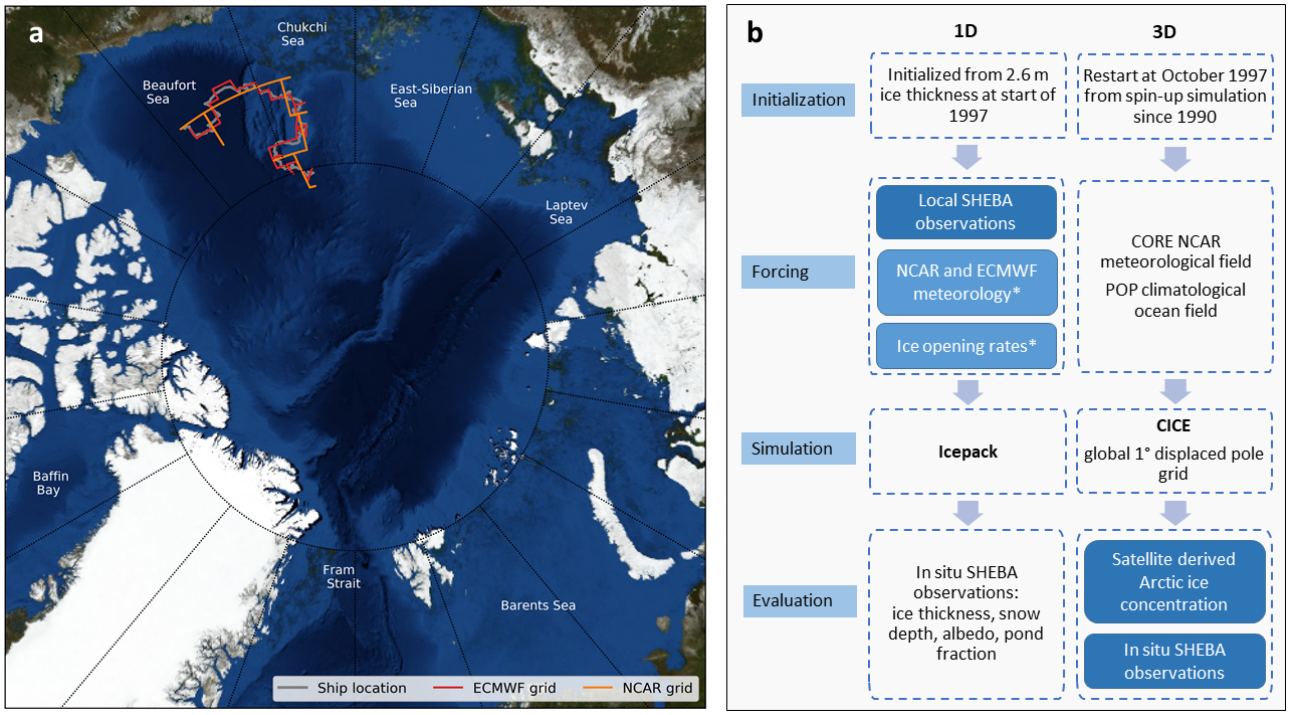

Figure 2.3 | SHEBA expedition and simulation set-up. a) Drift trajectory of the SHEBA expedition. The ship started in the southern tip in October 1997 and finished October 1998. The red and orange line indicate the closest ECMWF and NCAR grid cells to the expedition track used for the ECMWF and NCAR experiments. b) Overview of the 1D and 3D simulation set-up for the SHEBA expedition period. *This forcing data is only used for experimental runs.

2.3.1 Initialization

In contrast to the 1D Icepack run, initialization from a spin-up run is important for a 3D simulation. Since we introduce horizontal processes and resulting deformation in this simulation, representation of multi-year ice becomes essential. A spin-up is therefore necessary to represent a perennial sea ice cover that has undergone several deformation processes and transformations of ice structure. These deformation processes have in turn effect on the ice-ocean and atmosphere interactions.

The simulations with CICE are initialized from a 7 year model simulation (1990-1997). A spin-up of 7 years was used to limit the computational costs and time, while representing multi-year ice. The spin-up simulation is forced with atmospheric forcing fields provided by the Coordinated Ocean-ice Reference Experiments (CORE). The CORE interannual varying forcing data is used, which was developed by Large and Yeager (2008) at the National Center for Atmospheric Research (NCAR). The CORE NCAR forcing dataset includes 6-hourly 10-meter air temperature, specific humidity, meridional and zonal wind velocities. The CORE NCAR forcing data was remapped from the T62 grid onto the gx1v3 CICE grid. Downwelling shortwave and longwave radiation in the spin-up are based on latitude and a monthly climatologic cloud coverage. Precipitation is based on a monthly climatology.

Monthly averaged ocean model output from POP is used as a climatologic ocean forcing data set. SST, SSS, mixed layer depth and ocean heat flux over the mixed layer depth together with sea surface tilt in the zonal and meridional direction are used as ocean forcing fields. The POP ocean currents were not used since these cause a outflow of ice at the Fram strait which is too large (specified in code).

2.3.2 Forcing and additional simulations

The simulation during the SHEBA expedition period is initialized from the above mentioned spin-up simulation. The forcing data sets are similar to the spin-up simulation, with the only difference that daily NCAR downwelling shortwave and longwave radiation and monthly rain and snowfall fields for 1997 and 1998 are used and remapped onto the gx1v3 grid instead of using the climatologies. Similar as in the spin-up, ocean currents are set to zero.

In total 4 different 3D simulations were created for the SHEBA expedition period. One simulation uses a slower restoring timescale of 90 days, in stead of the 15 days restoring timescale in the other simulations. Another simulation uses the topo-pond parameterization, in stead of the level-pond parameterization. Lastly, one simulation uses the oceanic currents from the POP forcing data set. This last simulation is only used in the discussion.

2.4 Model evaluation

The 1D and 3D model simulation results are evaluated against local measurements and satellite observations, both for temporal and spatial comparison. We describe here the evaluation data and statistical methods we used.

The one-dimensional results are evaluated against the local mass balance and energy balance measurements from the SHEBA expedition, which took place from October 1997 until October 1998. Perovich et al. (2007a) measured ice and snow thickness by installing 135 thickness gauges and ablation stakes. These 135 stakes were clustered in 10 measurement sites with different ice characteristics, varying from thin first-year ice to thicker multi-year ice and thick ice ridges. At 7 out of the 10 sites, thermistor strings were installed to measure vertical temperature gradients within the ice and snowpack (Perovich et al., 2007c). The temperature and mass balance measurements are used to evaluate the growth and melt of the ice in the model simulation. More information on the mass balance sites can be found in Appendix A.1. For evaluation of albedo, wavelength-integrated albedos along a transect are used (Perovich et al., 2007b). Finally, observed pond fractions from aerial pictures over the SHEBA field set-up are used to evaluate the simulation of melt ponds (Perovich et al., 2002a).

The three-dimensional simulation results are evaluated on both the pan-Arctic and the local scale. The simulated Arctic ice cover is evaluated against satellite products of ice age (Tschudi et al., 2019) and ice concentration (OSI SAF, 2016). Satellite products of ice thickness and albedo are not available for the time-period of the SHEBA expedition. Therefore only the simulated ice age and ice concentrations are compared with observations for the pan-Arctic field. Subsequently, the 3D simulation is evaluated against local observations from the SHEBA campaign. This is done in two different ways. Firstly, by co-sampling of the grid cells closest to the SHEBA ship trajectory. Secondly, by averaging the output over a larger domain enclosing the entire SHEBA trajectory. Variables that will be evaluated with the SHEBA observations are ice concentration, ice thickness, snow depth, melt pond fraction and albedo.

Different statistical metrics are used to evaluate the model simulation against observations. The main metric that is used is the Root Mean-Square Error (RMSE), to show how well evaluation data and the simulations agree. The RMSE is calculated as

$$RMSE = \sqrt{\frac{\sum_{i=1}^{N}(z_{ri} - z_{0i})^2}{N}} \tag{2.5}$$

where N represents again the number of data points, z_{ri} the CICE simulated value and z_{0i} the observation. In order to calculate RMSE between satellite and CICE simulation fields, both data were remapped on a regular global 320x384 grid (same amount of cells in lat/lon as the gx1v3 grid used in the simulations).

For a analysis of the different meteorological forcing data sets in Appendix A.4 a bias was used to express the difference between the meteorological forcing data from model output and observations. The bias is calculated with

$$Bias = \frac{\sum_{i=1}^{N}(z_{ri} - z_{0i})}{N} \tag{2.6}$$

where N represent the number of data points, z_{ri} represents the modelled value and z_{0i} the observation. For this comparison of different meteorological forcing data sets was also the R^2 used to calculate the correlation. Here R^2 is the correlation coefficient from linear regression.

3 Icepack 1D results

In this section we discuss the results of the 1D simulations with Icepack. Firstly, we discuss the results of the control run and evaluate it against observations (Section 3.1). Next, we compare the results of runs using different pond schemes and using different forcing data sets (Section 3.3 and 3.2). An overview of the different experimental runs is given in Table 2.2

3.1 Control simulation

The simulation results of two important state variables of Icepack, snow and ice thickness, are plotted in Figure 3.1 for the SHEBA expedition period (October 1997 - October 1998). All simulated ice thicknesses that are plotted in this thesis represent the 'actual' ice thickness, which is the average thickness over the ice-covered part of the grid cell. The coloured scatter in the figure shows measured ice thickness at different mass balance sites during the SHEBA expedition from Perovich et al. (2003). The simulated ice thickness from the control run *CNTL* (Figure 3.1a) shows an increase in ice thickness until beginning of June, followed by a strong decrease until half of August. This pattern of growth and melt agrees well with the observed temporal variability at the different mass balance sites. The simulated ice thickness represents the average ice thickness of the measurements well. The ice thickness measurements show though a large variation between the measurement location. This variation is caused by the different sea ice types at the measurement locations, varying from thin single year sea ice, to thicker multiyear ice or very thick ice ridges. More details on the sea ice characteristics of each of the mass balance sites can be found in Appendix A.1. Besides the variation between the sites, within some of the locations large variation up to 5m for The Ridge site is visible. This shows the small scale variation caused by local differences in thickness due to formation of ridges.

The simulation of the next important state variable, snow depth, is is plotted with snow stake measurements in Figure 3.1b. The simulated snow depth increases until the second half of May to 30.5 cm. This simulated snow depth is lower than most of the stake measurements, however it agrees well with the 32 cm that was calculated from temperature profiles in snow and ice (not shown) by Huwald et al. (2005), which is considered more reliable than the high spatial variable stake measurements. The high spatial variation in the stake measurements is very large in winter and spring, which is likely due to redistribution by wind. Wind blowing effects are not represented in Icepack.

The onset of the simulated snow melt is on 26th of May, a little earlier than the start of the surface melt season found by Perovich et al. (2003) on 29th of May. The simulated snow cover is fully melted by June 7th. This is faster than most of the measurements (Figure 3.1b) and due to the thinner simulated snow pack compared to observations. Perovich et al. (2003) found only for some locations with a thin snow cover that the snow was gone in a similar short time, such as for the Quebec site where the snow was gone by the 5th of June. The simulated snow melt rate is on average 2.8 cm/d during this period, while the average melt rate of the snow from measurements is around 1 cm/d. This rather fast snow melt obviously impacted the simulated ice thickness.

The simulated melt of the ice starts slightly earlier and is stronger compared to most of the stake measurements (Figure 3.1a). A possible reason for this is that in the simulations the ice became snow-free relatively fast and therefore surface melt of ice could

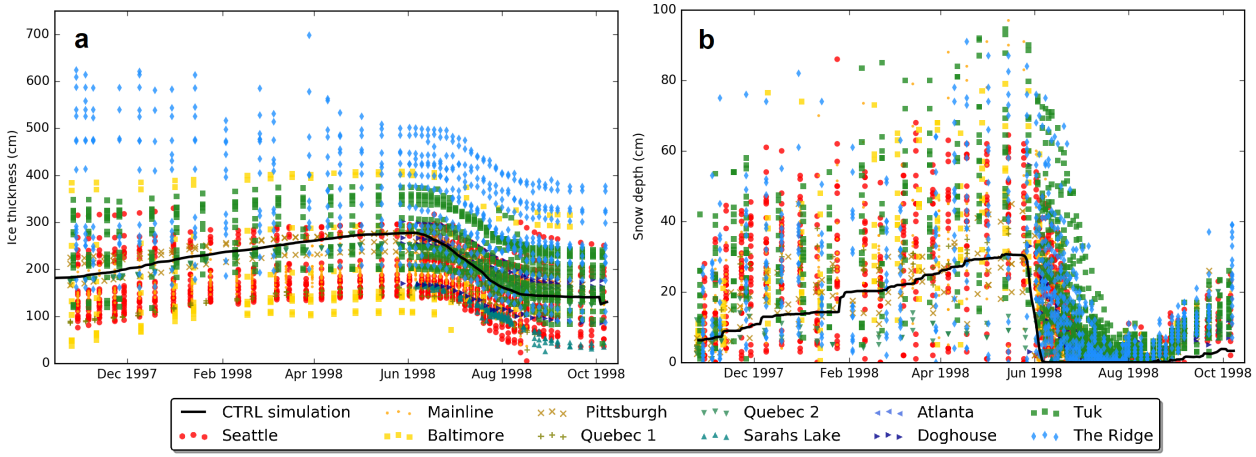

Figure 3.1 | Icepack simulated sea ice thickness (a) and snow depth (b). Ice thickness and snow depth stake measurements are plotted with different colors for different ice mass balance sites at the SHEBA field location from Perovich et al. (2003). See Appendix A.1 for an overview of these mass balance sites.

.

start earlier and continue over a longer period. This shows the important role of the simulated snow-depth on the ice thickness evolution, which will be covered in Section 3.2.2 in more detail. To understand the evolution of the snow and ice thickness, we analyse the different melt and growth components.

The relative importance of different simulated growth and melt terms (Figure 2.1) for snow and ice is visualized in Figure 3.2. The ice grew in the simulation period mainly through bottom growth on existing ice (88cm), also referred to as congelation. The rest of the increase in ice volume is caused by frazil ice formation, the formation of new ice crystals in the water column when this cools to the freezing temperature (36 cm). Ice grows at the bottom of the ice when the ocean water under the ice cools to the freezing temperature, as a result of an upward conductive heat flux arising from a negative temperature gradient in the ice. This link between the vertical temperature gradients and bottom melt and growth is visualized in Figure 3.3. Figure 3.3a shows the ice category-weighted average temperature profiles during the SHEBA period (Oct 10th 1997 - Oct 10th 1998), based on the simulated ice temperature in 7 layers for each of the 5 ice categories. On top of the ice temperature profile, the average snow depth is shown in gray. The lowering of the ice surface in June in Figure 3.3a represents the loss in ice thickness due to surface melt. The temperature gradients from roughly Oct 1997 until June 1998 result in an upward transport of heat and growth of ice to the bottom of the ice. The bottom ice growth is shown in blue in Figure 3.3b. The peaks in simulated bottom growth (Figure 3.3b) mostly resemble the strongest temperature gradients in the ice.

The simulated ice temperatures profile is very comparable with the temperatures measured at the Pittsburgh mass balance site (see Appendix A.2, Figure A.2c). This mass balance site shows comparable initial ice thickness and snow depth, and can therefore be used for comparison. During the winter period the simulated ice temperatures show colder temperatures compared to the measurements. Apart from that, the evolution of the ice temperatures is very similar. The ice growth though was larger in the simulation, together with a larger surface melt in summer.

The accumulated melt and growth terms of the simulation for the SHEBA expedition (Oct 10th 1997 - Oct 10th 1998) are shown in Figure 3.2. The dominant ice melt component is surface melt, which was 120 cm in total. Total bottom melt was 41 cm and lateral melt only 5 cm. Snow-ice formation, sublimation and condensation are negligibly small compared to the other growth and melt terms. The relative contribution of surface melt was greater than bottom melt in our simulation, while bottom and surface melt were comparable in the mass balance study by Perovich et al. (2003). We can explain this difference by the fact that our 1D-simulation does not include any dynamics and opening of the ice. This opening would result in warming of the water and therefore an increase in the bottom melt.

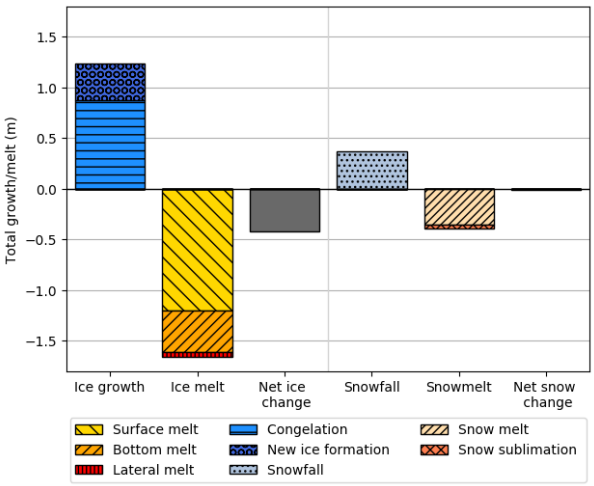

Figure 3.2 | Budget of simulated growth and melt. The melt and growth terms are given for the SHEBA expedition period (Oct 10th 1997 - Oct 10th 1998), in total volume per area (m) change of ice and snow.

In Section 3.2.1 we conduct an experiment with additional opening forcing data for the 1D-simulation to test how this influences the relative contribution of bottom and lateral melt.

Bottom melt started half of June, a little later than the measured bottom-melt onset by Perovich et al. (2003) in early June. The timing of the start of bottom melt is likely again influenced by the fact that there is no dynamical opening of the ice in our control run. We expect with an opening of the ice an earlier warming of the water and therefore an earlier start of the bottom melt. The surface melt period starts and ends earlier than the bottom melt period, which is to be expected due to the delay in the warming and in the cooling of the water.

The separate terms together gave a total ice growth of 125 cm and a total ice melt of 167 cm, resulting in a net ice loss of 42 cm. The mass balance study done by Perovich et al. (2003) showed on average a net loss of approximately 75 cm, reflecting strong variations in net loss from 20 cm up to 180 cm between sites.

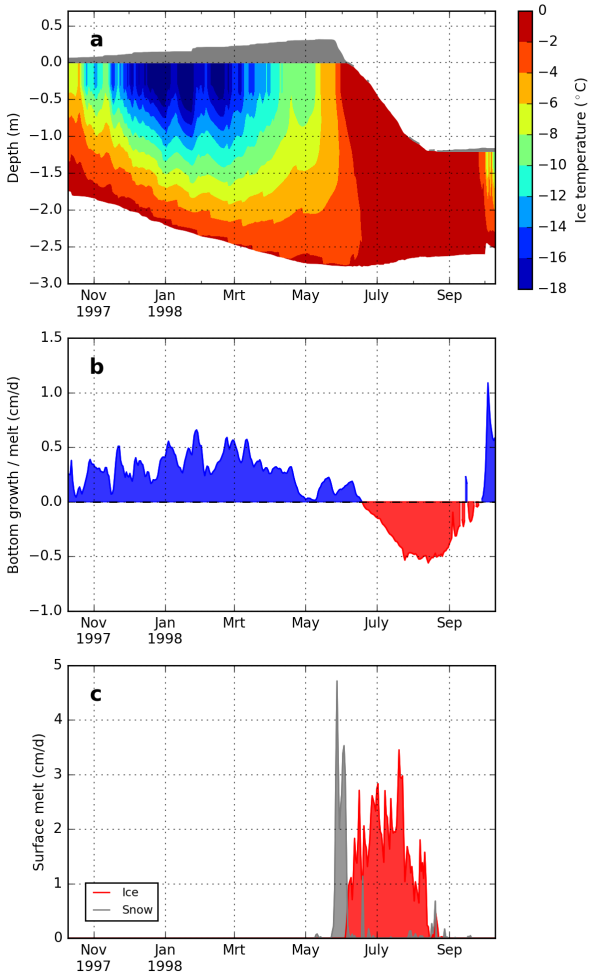

Figure 3.3 | Simulated evolution of ice temperatures (a), bottom growth and melt (b) and surface melt (c) for the SHEBA period. The temperature profile is an ice-category weighted average and shows the average snow depth on top.

3.2 Impact forcing data sets

3.2.1 Ice opening rates

The results of the 1D simulation are useful to understand the relative importance of different processes that influence the growth and melt of ice. A limitation however is that this simulation does not include any horizontal transport, with resulting opening and ridging of ice. To study the impact of opening of the ice on the sea ice response, we run the Icepack model with additional forcing data that contain opening and closing rates. These rates were computed by Stern and Lindsay (2000) based on SAR image observations on 4 sizes of square regions centered on the SHEBA site, by tracking changes in the individual cells within each region. In this way these opening and closing rates imitate the effect of dynamical opening and closing of the ice pack in the 1D simulation. This simulation reduces the ice area, but does not simulate actual dynamical effects such as ridging. The simulated state variables that are impacted are shown in Figure 3.4, where blue shows the control run (*CNTL*) and the green dashed line the results when additional opening rates were used (*OPEN*). The *NCAR* and *ECMWF* runs in orange and red will be discussed in Section 3.2.2.

The run with additional opening rates results in a thicker ice thickness, up to 0.6 m thicker (Figure 3.4a). This seems counter-intuitive, since with more opening of the ice more growth of new (thin) ice is expected and therefore on average a thinner ice pack. To explain this unexpected result we look into the melt and growth terms. Table 3.1 shows the total absolute and relative contribution of the different ice growth and melt components. Here we see indeed in total more new ice formation: where in the control run there was only 36 cm of new ice formation, in the *OPEN* experiment this is 53.1 cm (Table 3.1). Figure 3.5 shows the timing of the different melt and growth components. We see that especially in January/February there is additional new ice formation in the *OPEN* compared to the *CNTL* experiment (Figure 3.5e). This period of increased new ice formation is a result of the opening of the ice, induced by the forcing data. The opening results here in a cooling of the surface water to the freezing temperature, which leads to enhanced ice formation (Figure 3.4f). This new ice formation is not only in open water, but is distributed over the ice categories when no open water fraction is present. This causes an increase in the overall ice thickness. In reality indeed the frazil ice can collect under sea ice when the seawater gets super-cooled. However, the resulting larger ice thickness in the OPEN simulation agrees less with the observed ice thickness (Figure 3.1).

Besides the increase in new ice formation, there is a total increase in bottom growth onto existing ice from 88.0 cm in *CNTL* to 94.2 cm in the *OPEN* experiment (Table 3.1). However, there is not a strong increase in bottom growth in May to explain the sudden increase in ice thickness that is visible during this period (Figure 3.5d). Note here that Figure 3.4a shows the average ice thickness and does not represent the total ice volume, which is plotted in 3.4d. Actually here an increase in lateral melt (Figure 3.5c) of thin ice reduces the ice area and leads to the increase in the average ice thickness, while the ice volume decreases. A plot of the contribution of the different ice categories to the average ice thickness in Appendix A.3 (Figure A.3) supports this explanation.

Subsequently, the melt season is affected by the additional opening rates. During the melt season, the simulated ice volume in the *OPEN* experiment decreases faster than in the control run (3.4d). When analysing the individual melt terms, we see that the bottom melt and lateral melt are strongest impacted by the opening of the ice (Figure 3.5b,c). During the summer period we see an enhanced bottom melt and an earlier start of the bottom melt period (Figure

Table 3.1 | Simulated absolute and relative contribution of ice growth and ice melt components for the *CNTL*, *OPEN*, ECMWF and *NCAR* simulations. Contributions are given for the period of October 10th 1997 - October 10th 1998..

Runs	Ice growth components								
	Congelation		New-ice		Snow-ice		Condensation		Total
	cm	*%*	*cm*	*%*	*cm*	*%*	*cm*	*%*	*cm*
CNTL	88.0	70.3	36.1	28.9	0.0	0.0	0.9	0.7	125.0
OPEN	94.2	63.0	53.1	35.5	0.0	0.0	2.1	1.4	149.5
ECMWF	85.8	70.6	34.6	28.5	0.0	0.0	1.2	1.0	121.6
NCAR	73.7	70.4	30.4	28.9	0.0	0.0	1.0	0.9	105.0

Runs	Ice melt components								
	Bottom melt		Top melt		Lateral melt		Sublimation		Total
	cm	*%*	*cm*	*%*	*cm*	*%*	*cm*	*%*	*cm*
CNTL	41.1	24.6	120.3	71.9	5.0	3.0	0.7	0.5	167.3
OPEN	52.4	28.1	98.3	52.7	35.4	19.0	0.36	0.2	186.5
ECMWF	40.8	26.0	111.0	70.7	4.8	3.0	0.3	0.2	156.9
NCAR	27.9	33.9	51.8	62.9	2.2	2.7	0.4	0.5	82.5

3.5c). The extra bottom melt is caused by the increase in the sea surface temperature (Figure 3.4f). The imposed opening of the ice in summer enables heating of the water, which is calculated by the slab ocean model in Icepack. The addition of opening rates to the simulation triggered a positive feedback system: the opening results in warming of the water, which increases lateral melt and the open area, which in turn results in more warming of the water.

In Section 3.1 we hypothesized that the relative importance of the melt components would change with opening of the ice. It did indeed change significantly the melting processes: while surface melt contributed 72% of the total melt in *CNTL*, it contributes now only by 53% (Table 3.1). This shift is partly caused by the increase in bottom and lateral melt, but as well by a decrease in surface melt. Surface melt started later (Figure 3.5a) and was in total more than 20 cm less in the *OPEN* experiment compared to the control simulation. This reduction in total surface melt is due to the fact that the ice area is lower because of enhanced lateral melt. The lower contribution of surface melt agrees better with the contributions found by Perovich et al. (2003).

Finally, we analyze some of the surface characteristics of the simulated ice. The average snow depth in the *OPEN* simulation is lower (Figure 3.4b), through an increase of snow sublimation of in total 2 cm (not shown). Small differences in albedo are visible at the start of the melt season, which has to do with a de-

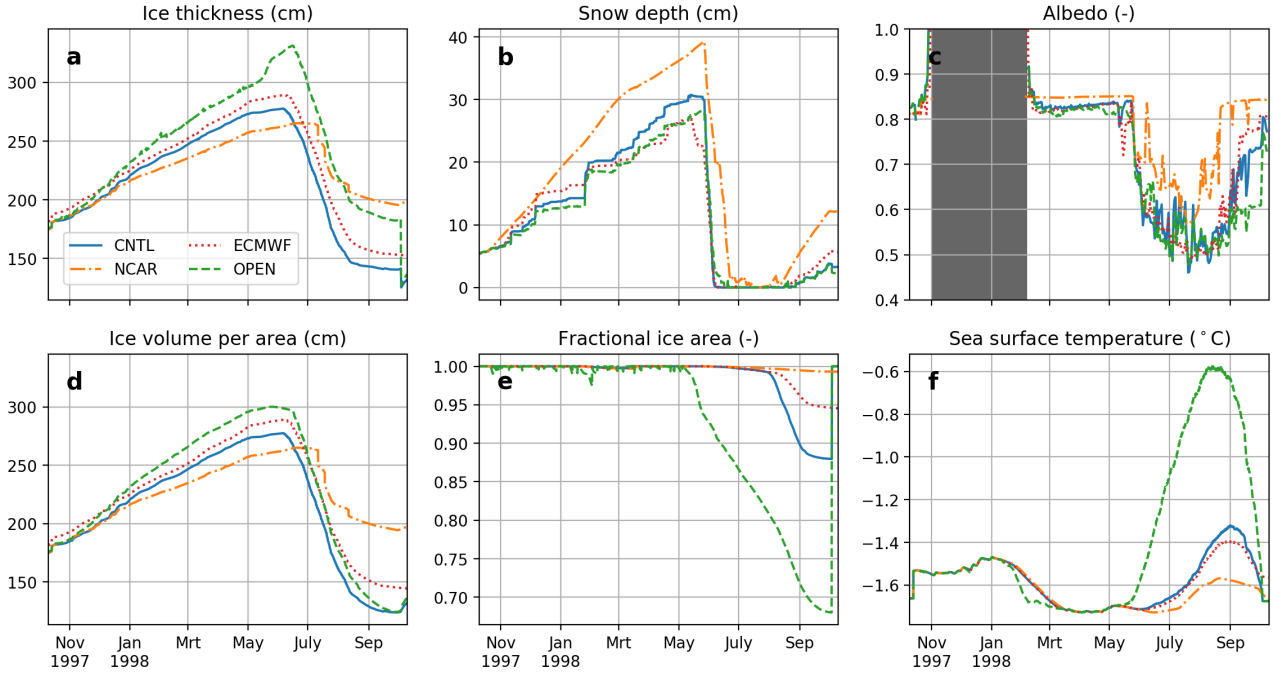

Figure 3.4 | Simulated state variables for the control run (*CNTL*) and *OPEN*, *ECMWF* and *NCAR* runs. The model simulations are shown for the SHEBA expedition period (Oct 1997 - Oct 1998). The albedo given in **c)** represents the grid-averaged albedo.

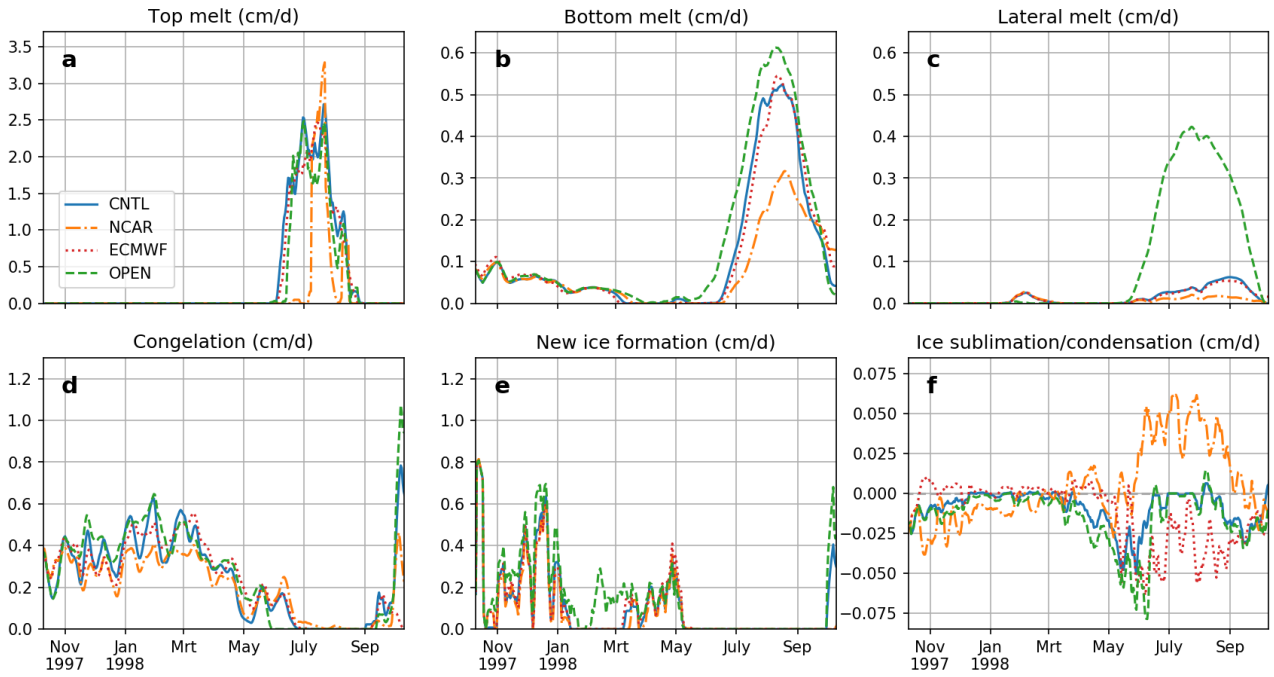

Figure 3.5 | Simulated melt (a, b, c, f) and growth (d, e, f) components for the control run (*CNTL*) and *OPEN*, *ECMWF* and *NCAR* runs. The model simulations are shown for the SHEBA expedition period (Oct 1997 - Oct 1998). The data is smoothed using a Savitzky-Golay filter over 7 days to make the difference between runs better visible.

crease in effective pond area. The grid-averaged albedo however (Figure 3.4c) is lower especially in the end of the simulation due to a larger fraction of open water.

3.2.2 Meteorological forcing data sets

The control simulation forced with local measurements gives a good opportunity to evaluate the stand-alone sea ice model with local measured ice thickness measurements. However, when using CICE in a ice-atmosphere coupled mode to study the exchange of climate-active trace gasses in the Arctic, atmospheric forcing is provided in grid-cells by the meteorological model. In this experiment we do a simulation with column model output from ECMWF to see what the impact is of using grid-averaged meteorology input instead of local measurements. Additionally, the NCAR CORE forcing that will be used for the 3D simulations in Section 4 is selected for the SHEBA ship trajectory and used as forcing data for Icepack. These simulations are used to analyze the uncertainty induced by the meteorological forcing data. The locations of the closest ECMWF and NCAR grid cells to the ship trajectory is given in Figure 2.3.

Some of the differences in atmospheric forcing between the observations and ECMWF and NCAR datasets are presented in Figure 3.6. The ECMWF air temperature is fluctuating less than observed at the SHEBA site, with slightly lower temperatures in summer (Figure 3.6). The NCAR temperatures follow on the other hand the observed fluctuations very well. Fluctuations in specific humidity are smaller as well in winter for ECMWF compared with observed values. While the specific humidity's in winter agree well, larger differences are visible in summer. The ECMWF specific humidity is considerably smaller in summer compared to the observed specific humidity. In contrast, the NCAR specific humidity is higher than observed. The wind and radiation terms are given in Appendix A.4, Figure A.4. Notable is the NCAR incoming longwave radiation, which is overestimated in winter while underestimated in summer. Figure A.5 in Appendix A.4 shows correlation between the observations and the NCAR and ECMWF data sets, together with the bias. Lastly, we compare the precipitation of the different data sets (Figure 3.6c): ECMWF has in spring less snowfall than observed and more rainfall in summer than observed. Largest differences are for the NCAR dataset, with almost 10 cm more snowfall in summer than measured.

Looking at the impact of these atmospheric forcing data sets on the state variables, we see the largest impact using the NCAR data (Figure 3.4). At the end of summer, the NCAR simulated ice thickness reaches a smaller thickness and remains thicker over the melt season compared to the other simulations (Figure 3.4a). The NCAR snow depth increases stronger during winter and spring and is melted away slower in summer (Figure 3.4b). Besides having a thicker ice pack in summer, the area remains almost completely ice covered while in ECMWF and *CNTL* there is an open water fraction of at least 5% and 10% respectively. The colder sea surface temperature

in summer of NCAR (Figure 3.4f) is a result of the smaller open water fraction.

The NCAR simulation shows us the impact of snow on the melt and growth components. The insulating effect of the extra snow results in a decrease in congelation of 15 cm, which explains the smaller ice thickness before the melt onset. The thicker snow cover at the start of the melt season subsequently delays the onset of the surface melt (Figure 3.5a). The decreased surface melt results in less pond formation, a higher summer ice albedo and resulting in a total surface melt which is less than half of the surface melt in *CNTL* (Table 3.1). Not only surface melt, but also bottom and lateral melt are strongly reduced, owing to the reduced warming of the sea surface water in summer. Ultimately, the total melt in NCAR is 82 cm over the whole season, compared to 167.3 cm in *CNTL* (Table 3.1)

The impact of using the ECMWF forcing compared to the observed meteorology (*CNTL*) on the state variables is rather small (Figure 3.4). The small changes in ice thickness and volume are the result of small variations in congelation, new ice formation and surface melt (Figure 3.5a and d, e). This shows that the strong variations in air temperature from the observations in winter and spring do not have a large impact on the ice simulation, as long as their average temperatures agree. The differences in snowfall described before had a much larger impact on the ice simulation.

Finally, the sublimation/condensation term is strongly dependent on the meteorological forcing. Figure 3.5f shows the sublimation (values < 0) and condensation (values > 0) of ice for the different simulations. The control run shows mostly only sublimation. Focusing on the summer period, we see enhanced sublimation when using the ECMWF data and remarkable is the shift of sign when using the NCAR data. This pattern in summer of condensation (sublimation) using the NCAR (ECMWF) data holds as well for the sublimation/condensation of snow (not shown). The calculated latent heat flux determines whether the ice/snow is evaporated or condensed, which has a positive sign in summer for NCAR while being negative using the ECMWF dataset. This sign shift is caused by the air specific humidity that is given as atmospheric forcing (Figure 3.6b) that is used together with the surface humidity to calculate the latent heat flux in Icepack. This result shows that the condensation/sublimation term depends strongly on the specific humidity from the atmospheric forcing data-set. On the other hand, ice sublimation/condensation makes only a small contribution to the total melt and growth of ice, when we look at the balance of melt and growth components in Table 3.1.

3.3 Melt pond schemes

Here we present an evaluation of the simulated albedo and formation of melt ponds for simulations using different melt pond schemes. The *CNTL* run uses the level-melt pond scheme by Hunke et al. (2013), which simulates the effect that melt water collects on the undeformed (level) ice. *TOPO* uses the topo-pond scheme, which simulates gravity effects as well but using the ice thickness categories. *CESM* simulates melt ponds with a fixed pond shape, so that pond depth is a linear function of pond fraction.

Figure 3.7 shows the evolution of melt ponds for the melt season (May-October) of the SHEBA expedition and its impact on the simulated albedo. Firstly, in Figure 3.7a, the fractional area of the grid cell covered by ponds is plotted for the three runs. In this figure the 'effective pond area' is plotted with dashed line, which represents the pond area that is used for the albedo calculations. Also is shown the estimated pond fraction over the SHEBA site from aerial pictures (Perovich et al., 2002a). Secondly, in Figure 3.7b, the

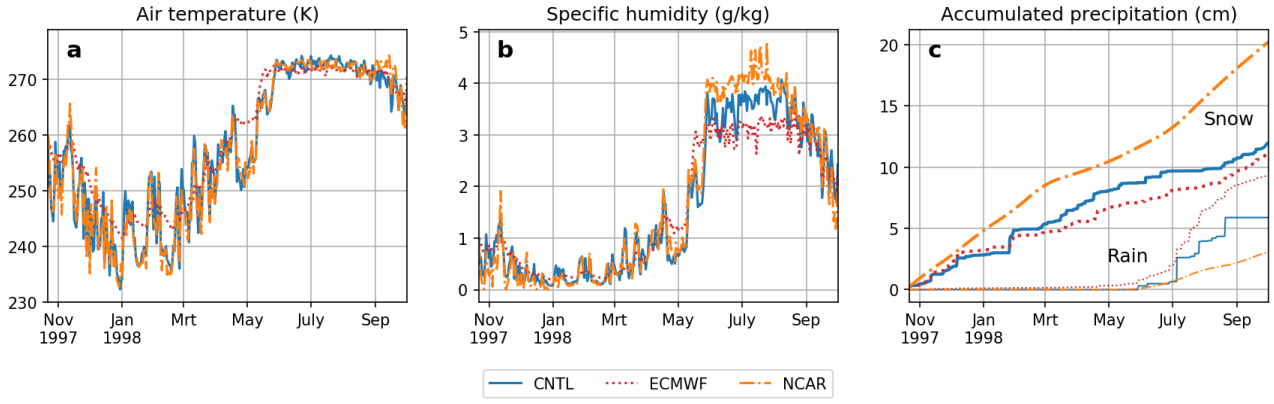

Figure 3.6 | Atmospheric forcing used in the *CNTL*, *ECMWF* and *NCAR* runs. a) 2-m air temperature, **b)** 2-m specific humidity and **c)** accumulated snowfall (solid line) and rainfall (dashed line) from the start of the SHEBA experiment. Snow is given in snow water equivalent (cm). A comparison of the remaining meteorological variables is given in Appendix A.4.

simulated depth of the ponds is plotted and on top of that the refrozen lid thickness (when no difference in the two lines is visible, no ice lid is present). Observed pond depths and standard deviations along the albedo transect are shown in this figure as well. Thirdly in figure 3.7c the simulated albedo is shown. Next to the simulated albedos, the observed albedo values are shown that were measured by Perovich et al. (2003) along a transect and on the meteorological tower. Spatial variation in the measured albedos along this transect are visualized here with a mean and standard deviation.

Formation of ponds starts end of May for all simulations (Figure 3.7a). All simulations show an initial fast increase in pond fraction. After that we see different behavior for the different melt pond schemes. The simulated pond fraction in the control run increases steadily up to 0.8, which is significantly higher than the maximum pond fraction simulated by the *TOPO* and *CESM* scheme up to around 0.3. Another distinct difference between the simulations with the different pond schemes is the fluctuation in pond fraction that is simulated using the topo scheme, while the control run shows a rather steady increase of pond area during the melt season.

The *CNTL* simulated pond area up to 0.8 is too high when we compare this with measurements during the SHEBA experiment. Estimated melt pond fraction along the albedo line (a transect on the ice along which albedo and melt pond measurements have been made by Perovich et al. (2002a)) were up to a maximum of 0.4 (not shown). Melt pond fractions estimated for the SHEBA experiment from aerial photographs stay below 0.25 (Figure 3.7a). The control run uses the level ice melt pond scheme, which uses the principle that melt water flows down from deformed ice and collects on the lower flat areas (level ice). The large simulated pond area might be due to the fact that there is only level ice in the 1D run, since sea ice dynamics forming ridges are not represented in Icepack. This results in that the melt water spreads over a rather large area, with relative shallow ponds (Figure 3.7b).

The *TOPO* simulation seems to give better results for the simulated pond fraction than *CNTL*. The simulated pond depths up to 0.3 in *TOPO* agree better with the observations (RMSE 0.08 compared to RMSE of 0.4 for *CNTL*). The average pond depth in *TOPO* is fluctuating strongly, from only a few centimeters to 50 cm. This fluctuation is not seen in the observations, which show a rather steady increase in pond depth. The *CESM* melt pond scheme shows a similar evolution of pond depth and pond fraction, although a generally simulated smoother temporal variability compared to the *TOPO* simulations, since the pond scheme uses a fixed pond shape. The *CESM* simulated pond fraction and depth give the lowest RMSE with observations. This is though to

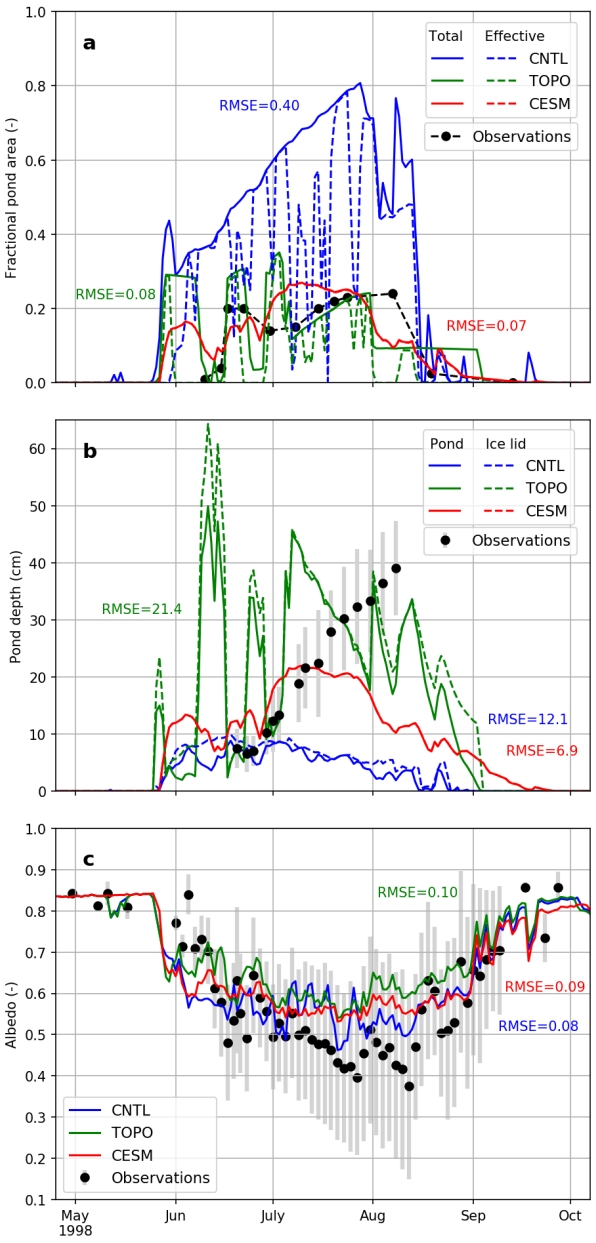

Figure 3.7 | Icepack simulated melt pond evolution during the SHEBA melt season for *CNTL*, *TOPO* and *CESM* run. a) Total pond area and pond area effective for the radiation calculation. The black dots show the estimated pond fraction from aerial pictures. **b)** Pond depth with on top the thickness of the refrozen pond ice lid. Pond depth observations along the albedo line are shown with mean and standard deviation. **c)** Albedo, plotted with the observations along a transect with mean and standard deviation.

be expected since this simple parameterization is strongly based on SHEBA melt pond observations.

Not the total pond area but the 'effective pond area' is what influences the albedo. The effective pond area can decrease when ice forms on top of the melt pond and shelters the radiative effects of the pond, while total pond area remains the same. Simulated albedos in Figure 3.7c represent albedos over the ice-covered parts of the grid-cell. This was plotted here in stead of

the grid-averaged albedo to be able to compare with the measurements over ice. The albedos drop fast at the end of May when snow melts and pond formation starts. The onset of melt is faster than observed, as described in the previous section, and this results in a faster drop in albedo compared to observations as well. The albedo decreases to 0.5 for the *CNTL* run and to 0.55 for *TOPO* and *CESM*. The simulated albedos are well in the range of the albedo-line measurements, although often larger than the observed average albedo along the albedo line. The large spread up to 0.5 in observed albedo is a clear indicator of the high spatial variability when melt-ponds form on ice. The fluctuations in the simulated albedos can be explained by changes in the effective pond area shown in Figure 3.7a, which is in turn affected by refreezing of the pond water. Remarkable is that while the *CNTL* run performs worst concerning the pond fraction and pond depth, the *CNTL* simulated albedo agrees best with observations. This might be due to the different spatial scales that are covered by the evaluation data set, since the spatial scale of the aerial picture based pond fraction is much larger than the albedo measurements along the transect.

3.4 Restoring of SST forcing

In the stand-alone runs with Icepack, a slab ocean parameterization is switched on which calculates the sea surface temperature based on the balance in forcing at the sea surface and under the ice. In one simulation experiment we restore the input sea surface temperature on a daily time-step, which nudges the temperatures to the observed values from CTD measurements (*RSST*). The bias in the simulated sea surface temperature using the default ocean-slab model set-up is slightly positive in winter, negative in spring and early summer and positive in late summer (Figure 3.8). The observed peak in sea surface temperature in summer occurs earlier and has smaller peak values than modelled. The SST bias can be caused by inconsistencies in the input forcing data set or by the limitations of the ocean slab parameterization, which does not account for freshwater and salt fluxes during ice growth and melt and vertical mixing processes in the water column.

The SST bias impacts both the simulated melt and growth components. Figure 3.8a shows the sea surface temperature for the control run and for the *RSST* simulation. In Figure 3.8b the most important melt and growth components are shown for the two different simulations. A large difference appears in the formation of new ice: where in the control run this contributed in total 36.1 cm of new ice formation in a year, this decreased to 7.6 cm in the simulation where the sea surface temperature is restored (*RSST*). The cause lies in the slightly warmer sea surface temperature that does not reach the freezing temperature. The congelation is impacted as well by the restoring; Especially in the winter months there is more congelation, due to an enhanced upward conductive heat flux and therefore loss of heat through the ice to the atmosphere (not shown).

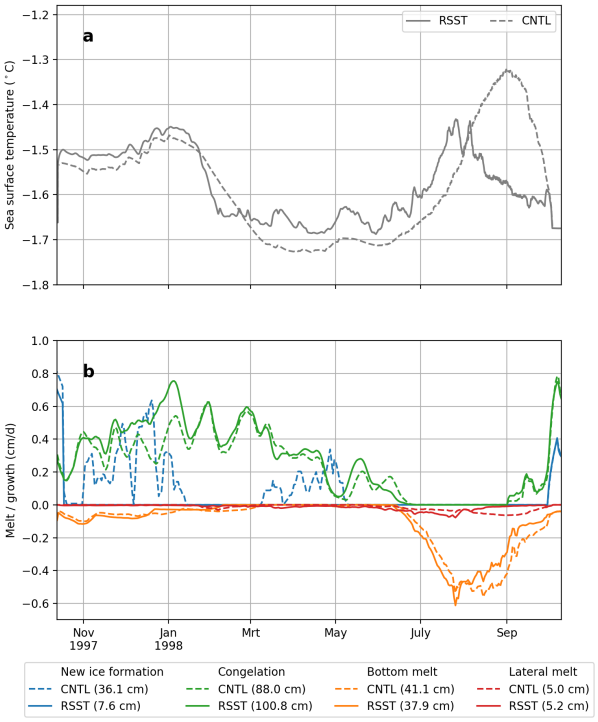

Figure 3.8 | Impact of SST restoring on growth and melt terms. Simulated sea surface temperature **a)** in the control run (*CNTL*) and *RSST* run. In **b)** are shown the simulated new ice formation, congelation, bottom and lateral melt. The total of the growth and melt terms is given in the legend.

When we then analyse the melt terms, we see that mainly the timing of the peaks in lateral and bottom melt changed. The onset of the melt is earlier for the *RSST* run. This shift is a reflection of the earlier simulated peak in SST in summer compared to that one in the *CNTL* simulation. These results show that the bias in the slab ocean calculations mainly affect the formation of new ice. This sensitivity of new ice formation to the calculated energy balance and resulting temperatures by the ocean slab model will be discussed as well in the following results section about the 3-dimensional simulations.

4 CICE 3D results

In this section we continue the discussion of the results, this time focussing on the 3D simulations with CICE. We will start with a short evaluation of the spin-up that is used to initialize the simulations (Section 4.1). We follow with an Arctic wide evaluation of the simulated ice cover (Section 4.2). Then we discuss results that show the role of SST restoring (Section 4.3) and we will link the results again to the smaller scale, by evaluating against the observations from the SHEBA campaign (Section 4.4). Finally, we evaluate the impact of melt pond schemes in the 3D simulations (Section 4.5).

4.1 Initialization

By introducing horizontal transport and deformation in the 3D simulation, the age of ice becomes relevant. The importance of ice age lies in the fact that the relative thin first year ice (FYI) deforms more easily and is more prone to melt. In contrast, multiyear ice (MYI) has undergone different cycles of deformation, is often thicker and more likely to remain through the melt season (Tschudi et al., 2019). Figure 4.1 shows in a) the simulated ice age at the start of the SHEBA expedition, and in b) the ice age obtained from a product by Tschudi et al. (2019). The observed ice age is calculated by tracking ice floes in satellite imagery, therefore new ice growth on the bottom of existing ice does not influence this age. Similarly, the simulated ice age increases with each time step and is not influenced by growth of new ice on the bottom of the ice column. Our simulation is restarted from a spin-up of 7,5 years and therefore the simulated ice age at the start of the simulation cannot reach ages above 7,5 years. It is clearly visible from the observed ice age that there is older ice up to more than 10 years old. The general spatial distribution of ice age corresponds well between the observations and the simulation: older ice is found closer to the coast of Greenland and Canada and younger ice on the Russian side of the Arctic Ocean. Some differences are visible which are a result of different ice motions. The simulation shows for example multiyear ice in the Chukchi Sea that is not present in the observations.

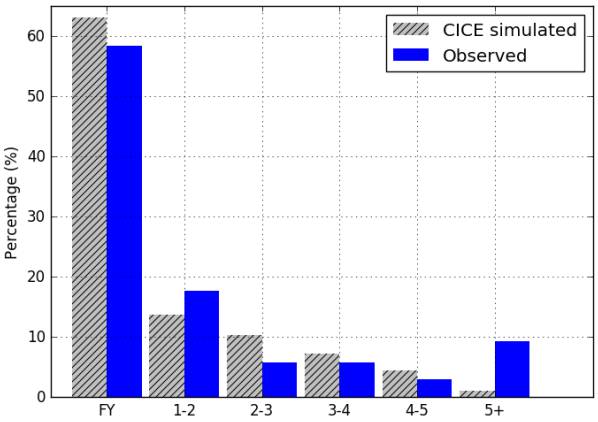

Figure 4.2 | Modelled and observed percentage of the ice covered grid cells per sea ice age. FY represents ice up to 1 year old.

The relative distribution of the ice ages is given in Figure 4.2. The largest difference lies in the percentage of ice older than 5 years. This difference is partly caused by the short spin-up simulation, since Hunke and Bitz (2009) found ice age in September 1997 with an average age of 5.5 years and ice up to 10 years old when using a simulation period of 27 years. Only a 7-years spin-up simulation was used to limit the computational costs and time. While this difference in contribution from old MYI is considerable, the percentage of FYI is for measured and simulated both

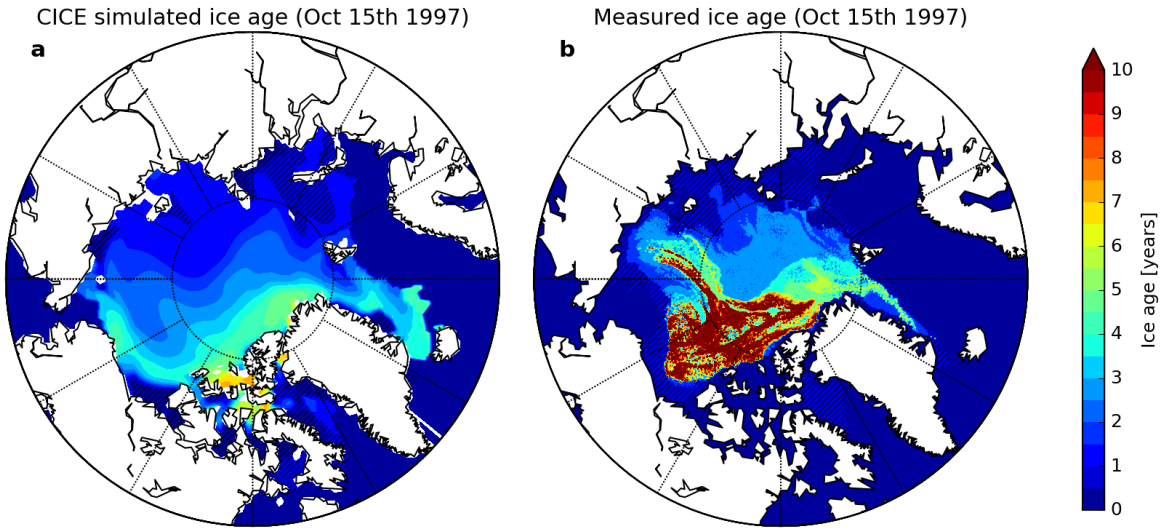

Figure 4.1 | Comparison of modelled vs observed ice age on Oct 15th 1997. Hatched area indicates first year sea ice (up to 1 year old). Observed ice age is based on a recently enhance sea ice age product by Tschudi et al. (2019), which shows the oldest ice per grid cell.

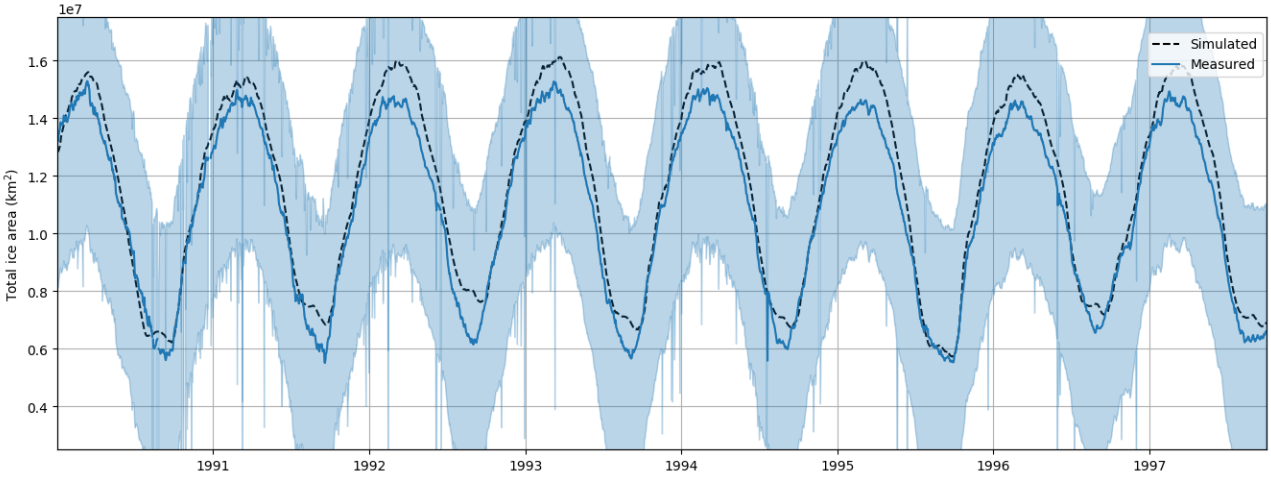

Figure 4.3 | Comparison of CICE simulated and observed Arctic ice area during the spin-up. In blue is shown the ice area from OSI SAF (2016) indicated with the total standard error as shaded area. The dashed black line shows the CICE simulated total ice area.

around 60 % (Figure 4.2). A representation of the FYI-MYI ratio is most important. The difference in susceptibility of ice to melt and deformation is largest between FYI and MYI and smaller between younger and older MYI. This is the case since the difference in ice thickness and ice strength between FYI and MYI is much larger than between younger and older MYI.

To further evaluate the initialization of our simulations, we show in Figure 4.3 the simulated ice area (dashed black line) together with observations (blue) for the spin-up period. The seasonal cycle in total Arctic ice extent matches between observations and the simulation. The mean total ice area is though slightly higher in the simulations, around 1.16e7 km^2, compared to an observed ice area of 1.09e7 km^2. Besides, the amplitude of the fluctuating ice area is smaller in the observations (4.6e6 km^2) compared to the simulation (5.1e6 km^2). While the simulated total ice area is larger than observations for 90 % of the spin-up, the variation in summer ice area between the years is comparable with the observations. The year of lowest ice area in summer is for both observations and simulations 1995, followed by 1990. The year of maximum summer ice area is 1992 for the simulation, whereas for the observations this is 1996. Some of the variation between the years in the observations is represented by the simulation, as a consequence of the yearly varying atmospheric forcing (temperature, humidity, horizontal and meridional wind velocities). In contrast, some variation might be missing since climatological data is used for the radiation and precipitation forcing.

A notable difference in the seasonal cycle between the simulation and observations is visible at the end of each melting season; The observations show a clear decrease in ice area in each summer, followed by a strong increase. The simulation however shows each year at the minimum ice areas a short period where there is a halt in the ice melt of even some slight ice growth. This period of freezing in summer is caused by the SST calculated by the slab ocean-model. The role of SST restoring in solving this issue will be discussed in Section 4.3 in more detail.

4.2 Pan-Arctic evaluation

We start the evaluation of the ice and growth in the 3D set-up by comparing the simulated fractional ice area with observed ice concentrations. Figure 4.4 shows the average fractional ice cover over the period of Oct 1997 - Sept 1998 based on the CICE simulation (a) and on observations (b). In Figure 4.4c the RMSE between the measurements and simulation is given, based on the same period. The simulation used in the comparison in this section uses a 15-days restoring timescale. The following Section 4.3 explains why this is most realistic.

The spatial distribution of the simulated ice area matches reasonable well the observations, showing high concentrations in the central Arctic ocean and lower fractions around Svalbard, in the Beaufort Sea and the Chuckchi Sea. The largest differences and therefore highest RMSE values between the observations and the simulation are found in the marginal ice zone. This is expected because the variations in ice fraction throughout the year are largest in this zone. The largest RMSE's are found in the Fram Strait, Barents Sea and south of the Baffin Bay. For these locations the simulations give higher fractional ice areas than observed.

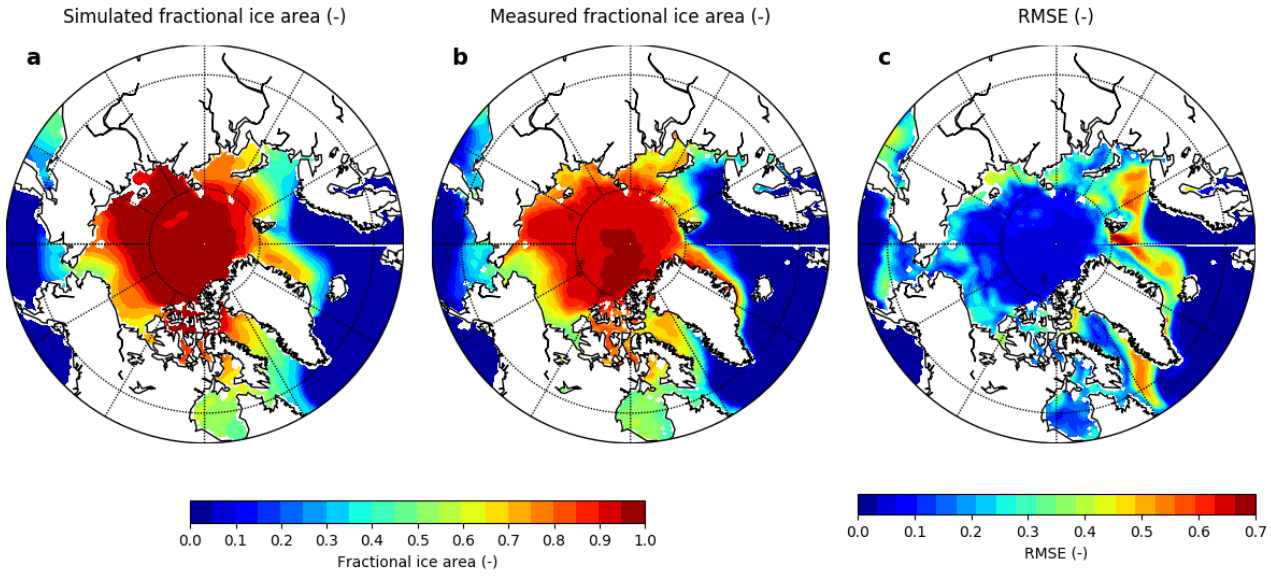

Figure 4.4 | Comparison of modelled vs observed average ice concentrations. In **a)** is shown the fractional ice area from CICE the simulation and in **b)** observed ice concentrations based on OSI SAF (2016). In **c)** is shown the RMSE per grid cell over the SHEBA period (Oct 1th 1997 - Sept 30th 1998) based on daily measurements and simulations.

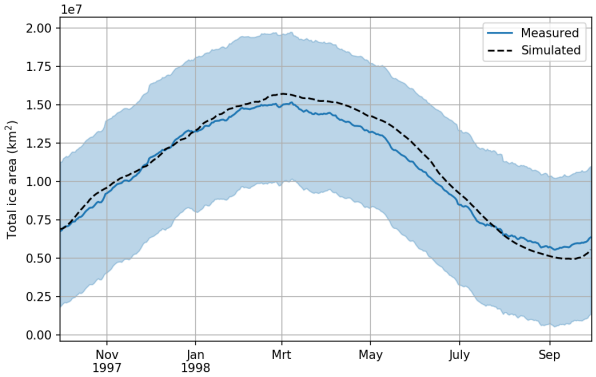

Figure 4.5 | Comparison of simulated and observed Arctic ice area during the SHEBA period. In blue is shown the ice area from OSI SAF (2016) indicated with the total standard error, the dashed black line shows the CICE simulated total Arctic ice area (km^2).

Even though the RMSE values are very low in the central Arctic, the simulation shows an almost completely closed ice cover (Figure 4.4a) while the measurements still show an open water fraction (Figure 4.4b). The simulated yearly average open water fraction is about 3% in the central Arctic ice and mostly zero in winter. This shows the lead fractions are very small in winter in the central Arctic, and higher in the marginal ice zone. Evaluating these small openings in the ice pack with the observed ice concentration in the central Arctic is however difficult, since the error of the ice concentration in the central Arctic is up to 0.12, while the expected lead fractions are much smaller.

Besides the spatial variation in ice concentration, we also analyse the total Arctic ice area in Figure 4.5. The figure shows the evolution of the total Arctic ice area, both based on observations with the total standard error (blue) and the CICE simulation (dashed black) for the period Oct 1th 1997 - Sept 30th 1998. The simulated ice area stays within the error range from observations for the entire simulation. The simulated total ice area is slightly larger in spring compared to the observations, and slightly smaller in September. Figure A.6 in Appendix A.5 shows spatial maps of the simulated vs observed ice area and the RMSE per season. During winter and spring the largest errors are found in the Barents Sea, Baffin Bay and the Fram Strait. These errors arise from transport of ice into these regions, which is not the case in the observations. During summer the errors are largest in the East Siberian Sea and Laptev Sea, where the ice remains while it shows open water in the observations.

4.3 Role of SST restoring

To link and compare the one-dimensional and 3-dimensional simulations, we analyze the CICE results along the SHEBA trajectory. This enables us as well to evaluate the 3D simulated field against local observations. The output for the grid-cell closest to the ship trajectory is selected for each day in the SHEBA campaign period. The 8 surrounding grid-cells of the closest cell are used to calculate a standard deviation. This standard deviation is given with the shaded area in Figure 4.6 and shows how representative the selected cells are for the larger domain. The ship trajectory is shown in the sub-figure in Figure 4.6b in black, where the red and lighter red dots show the closest grid-cells and surrounding cells.

An unexpected result in the 3D-simulation is a period of ice growth in August. Figure 4.6a shows the fractional area of ice and SST for the SHEBA trajectory, for the run using the initial chosen

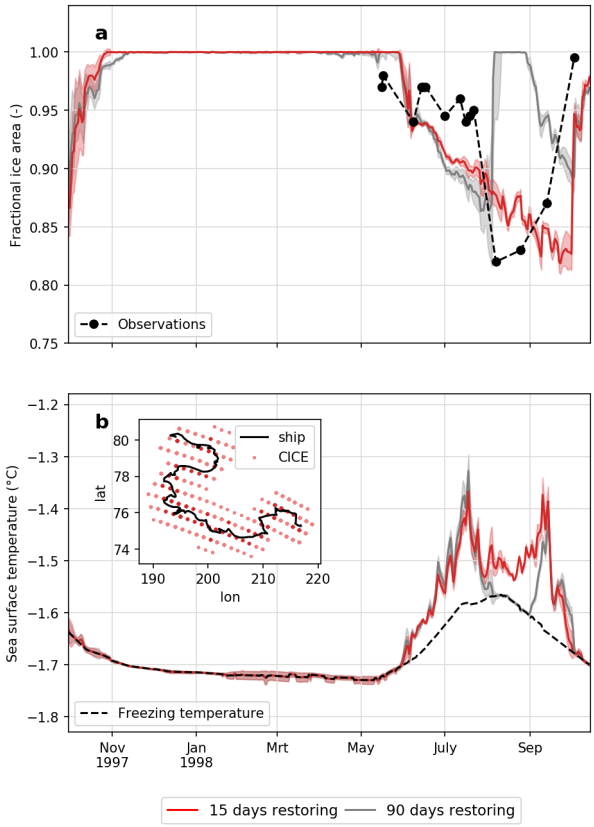

Figure 4.6 | Simulated and observed ice fraction (a) and sea surface temperature (b) along the SHEBA track. Two different CICE runs are plotted, using a slow SST restoring timescale of 90 (solid red) and faster SST restoring timescale of 15 days (dashed red).

restoring timescale of 90 days (red) and for a second run using a restoring time scale of 15 days (gray). The restoring time scale represents how fast the simulated SST is nudged towards the forced SST data. In the simulation with slow restoring (90 days), a rapid refreezing of the open water fraction is visible at the start of August, after which a period of melt follows at the start of September (Figure 4.6a). Estimated open water fraction from aerial pictures by Perovich et al. (2002b) indicate that this refreezing is not realistic (Figure 4.6a). When we evaluate the net surface energy flux along the SHEBA trajectory (see Appendix A.6), we find a positive net surface flux during August. This indicates that the short period of ice growth is not caused by a negative surface energy balance. In fact, the explanation should be found in the simulated SST by the slab ocean model. Figure 4.6b shows the calculated SST temperatures which increases in summer, drops from half July and reaches the freezing temperature in August causing the formation of new ice. Not a cooling by the atmosphere, but a cooling by the deep ocean heat flux results in this SST drop (not shown). We see in the same figure that an additional run with a shorter restoring timescale yields more realistic results: the SST is nudged to the warmer temperatures in summer, and the ice growth in summer is prevented.

Increasing the SST restoring is an indirect way to reduce the impact of the input deep ocean heat flux. Altering this ocean heat flux in the forcing data set would be another way to prevent this unrealistic result.

The restoring timescale impacts not only the simulation along the SHEBA trajectory, but also the entire Arctic ice pack. In Appendix A.7 we show the simulated ice area and thickness in the Arctic, for the run using 15 and 90 days SST restoring. The increased nudging towards the SST forcing results in less and thinner ice in the Greenland and Barents Sea as well in the central Arctic. Conversely, the increased SST restoring gives more and thicker ice especially in the East Siberian and Laptev Sea and to a lesser extent in the Beaufort Sea. Looking at the RMSE field between this simulation using the 90 days SST restoring and observations (Figure 4.7), we see again the largest errors in the Fram Strait, Barents Sea and south of the Baffin Bay. However, in this simulation (90 days restoring) the RMSE errors in these areas are up to 0.3 higher compared to the RMSE errors in the simulation with a 15 days restoring (Figure 4.4c). An exception of the increased errors is in the East-Siberian Sea and Laptev Sea; In these areas coastal polynyas are expected to be found (Dmitrenko et al., 2001), that are areas where the persistent winds push the newly formed ice away and keep the area ice-free. Here the smaller simulated ice area using the 90 days in stead of 15 days restoring timescale agrees better with observations, showing RMSE's that are up to 0.2 smaller.

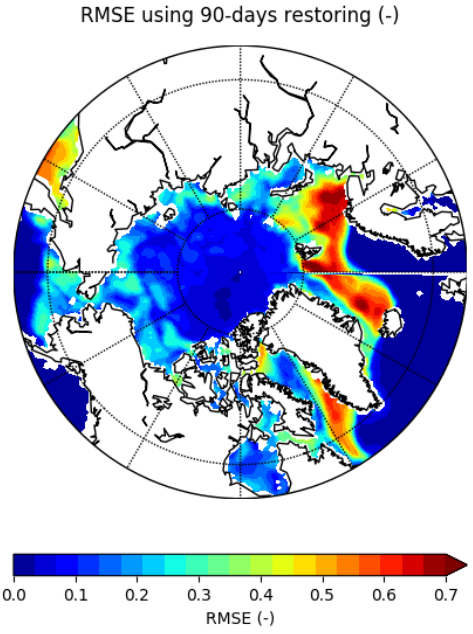

Figure 4.7 | RMSE between daily observations and simulation using a 90 days restoring timescale. RMSE is given per grid cell over the period Oct 1th 1997 - Sept 30th 1998.

After this spatial evaluation, we do a temporal

Figure 4.8 | RMSE between the CICE simulated and OSI SAF (2016) observed Arctic ice concentrations The RMSE error is calculated per daily time step, both for the simulation using a 15 and 90 days SST restoring timescale. The error represents the average RMSE of all ice covered grid cells.

evaluation of the errors of both simulations. For each day in the simulated period (Oct 1th 1997 - Sept 30th 1998), the RMSE is calculated for all grid cells that show ice in the Arctic in the simulations. Only in the erroneous case that the measurements show ice, when this is not simulated, this is not represented in the error. The RMSE is calculated from the ice covered grid cells, not weighted with the grid cell area. This can result in a total RMSE that is too low, since the grid cells in the central Arctic are impacting the total RMSE too much in this error. From previous analysis it was visible though that for most locations and time periods, the simulations show a larger ice area than the observations. The calculated RMSE's are given for the two simulations with fast and slower SST restoring in Figure 4.8. For the entire period, with exception of September, the error is smaller when using the restoring timescale of 15 days. From October until April, the errors are comparable for both simulations. After April the differences between simulations become larger, up to a difference in RMSE of 0.05. The restoring timescale shows the largest impact on the ice area in the melting season, for the reason that in this period small changes in SST can be critical to (not) reach the freezing temperature, and therefore strongly impact the fractional ice area. These results show the sensitivity of the ice area to the ocean boundary conditions, and therefore also the importance of coupling of sea ice dynamics to ocean models.

4.4 1D vs 3D evaluation

Since the simulation using a 15-day restoring timescale appears to be closest to the observations, we will use this run in the following evaluations. We will evaluate the main state variables, ice thickness and snow depth, along the trajectory. Figure 4.9a,b shows the simulated ice thickness and snow depth along the trajectory in red, where the shaded area indicates one standard deviation based on the ice/snow thicknesses of the 8 surrounding grid cells. In orange and blue are shown the 1D simulations forced with observed meteorology and NCAR meteorology, respectively. In Figure 4.9c,d the ice thickness and snow depth is given for the 3D simulation, but this time taking the average and standard deviation of a entire domain around the SHEBA trajectory. Observations are indicated by black dots that represent a moving average (period of 7 days) and in gray the standard deviation of all measurements within this period. A moving average is applied here since different mass balance sites were measured at different days, which would cause a fluctuation in the daily average that does not represent the changes in time but differences between sites. The moving average shows still large variation in the growing season since less measurements were done compared to the melting season. The original data that is used here was already shown in Figure 3.1 as colored scatter.

During the ice growing season the simulations overlap and fall all within the range of the observed ice thickness (Figure 4.9a). From May on, the simulations deviate more from each other. The 3D simulated ice thickness is largest over the entire melting season and falls outside the range of the observations in summer. In contrast, the 1D simulations stay within the range of the observations. This is reflected also in the RMSE between the mean observed and simulated ice thickness, which is largest for the 3D simulation and smallest for the 1D control simulation. Notable is the difference in onset of the melting season between the simulations: The 1D control simulation season shows the earliest melt in the beginning of June, the 3D and 1D NCAR simulation show a later onset and a more gradual ice melt. The 3D simulation shows an increase in the ice thickness in summer, which is not visible in the 1D simulation. However, we should be careful interpreting the changes in the 3D ice thickness. The 'increase' in ice thickness does not necessarily represent a period of ice growth in summer, but rather a larger ice thickness of the selected grid cells that resemble the summer SHEBA track position compared to the previous selected grid cells for the position at an earlier stage.

To avoid this problem of sudden changes in the thickness due to our co-sampling strategy, we evaluate the mean ice thickness also over a larger domain that includes the entire SHEBA trajectory (Figure 4.9c,d). This shows a larger ice thickness during the growing season and on average a lower ice thickness in summer. The spread in the ice thickness increases strongly towards the end of the summer period, representing the difference between ice in the perennial and the marginal ice zone. On one hand the RMSE of the domain averaged ice thickness is lower, on the other hand the evolution of the ice in the domain shows a stronger ice growth and melt compared to the observations.

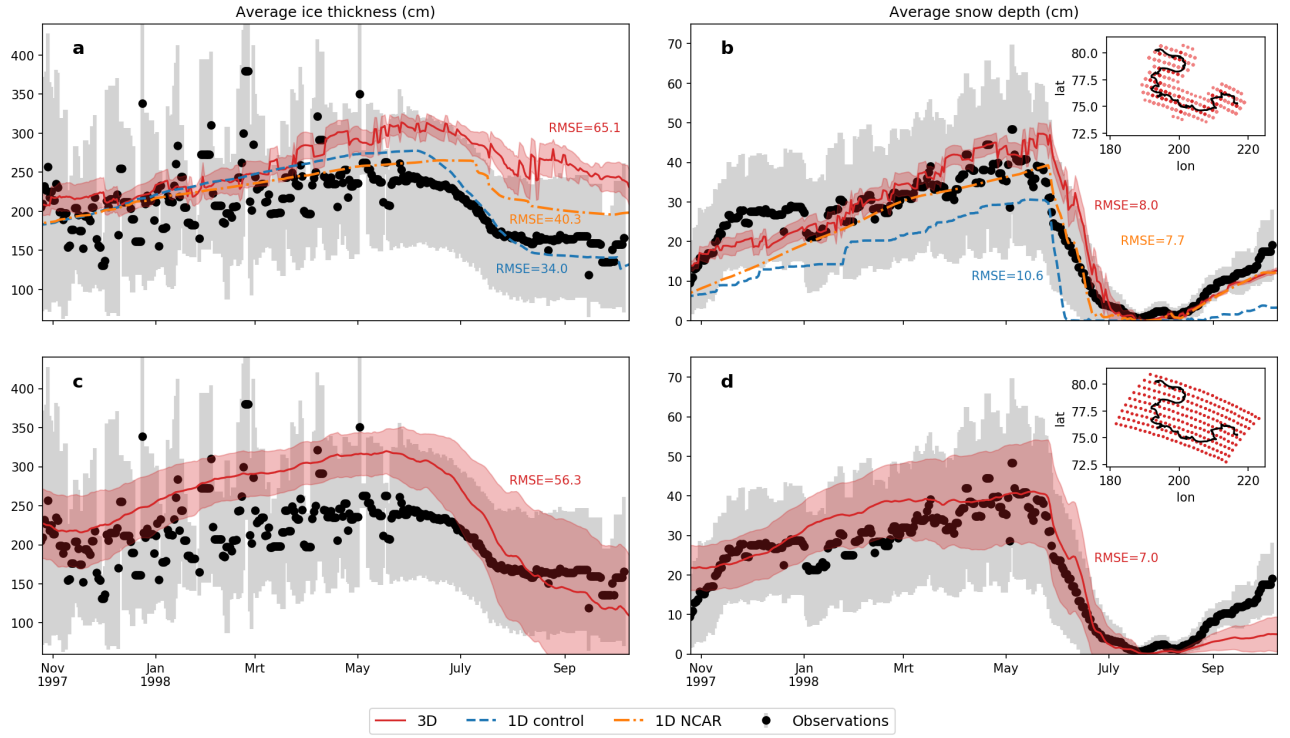

Figure 4.9 | Simulated and observed sea ice thickness (left) and snow depth (right) along the SHEBA trajectory. 1D simulations with Icepack are plotted in blue (using observations as forcing) and orange (using NCAR data as forcing). In red is shown the 3D simulated ice thickness/snow depth, with a mean and standard deviation of the 9 closest cells to the SHEBA trajectory (**a,b**) and of a domain over the entire trajectory (**c,d**). A moving average (7 day period) of the observed ice thickness and snow depth are plotted with standard deviation, based on Perovich et al. (2003). The RMSE between observations and the averaged observations is given per simulation.

The simulated ice melt is likely influenced by the simulated snow depth, therefore we also evaluate the snow depth shown in Figure 4.9b and d. During winter and spring, the snow depth of the 3D and 1D NCAR simulation correspond well with the observations (RMSE between 7.0 and 8.0 cm). The 1D control simulation is, in contrast, consistently smaller than the observations and the other simulations, which is due to the lower snowfall in the 1D control simulation compared to the NCAR data (used in 1D NCAR and 3D simulation, see Figure 3.6). Besides, the simulated snow melt in the 1D NCAR and 3D simulation agrees better with the observations compared to the 1D control run. The snow is melted away too fast compared to observations in the 1D control run.

Similarly we need to be careful interpreting the 3D simulated snow depth in Figure 4.9b. Fluctuations in the snow depth do not necessarily represent snowfall or melt events, but can be caused by the co-sampling strategy. The average snow-depth for the entire SHEBA domain (Figure 4.9d) shows smoother results. The average simulated snow depth represents very well with the observations for the period of April-September, resulting in the lowest RMSE of 7.7. The earlier onset of ice melt in Figure 4.9a for the 1D control simulation might be caused by the fact that all snow disappeared almost a month earlier in this simulation. Nevertheless, the results seem inconsistent since the 1D control simulations shows the largest error with snow observations, while it shows the smallest error for the simulated ice thickness. This inconsistency can be due to the inconsistencies in the SHEBA evaluation data set. Huwald et al. (2005) calculated snow depths from the precipitation measurements and found that these were much smaller than the observed snow depths. Our results show similarly that the 1D simulated snow depths are considerably lower than the observations when the observed snowfall rates are used as forcing data.

Table 4.1 | Melt and growth terms. Total absolute and relative contribution of the melt and growth terms over the entire domain that includes the SHEBA trajectory.

	3D (domain average)		**1D (forcing as 3D)**	
	Absolute	Relative	Absolute	Relative
Congelation	56.9 cm	48.9 %	69.8 cm	53.6 %
New-ice	55.6 cm	47.8 %	91.4 cm	53.5 %
Snow-ice	0.9 cm	0.8 %	0.0 cm	0.0 %
Condensation	3.0 cm	2.6 %	1.0 cm	0.6 %
Total growth	116.0 cm		170 cm	
Top melt	58.8 cm	30.5 %	47.0 cm	57.5 %
Bottom melt	128.9 cm	67.0 %	28.8 cm	35.3 %
Lateral melt	4.5 cm	2.3 %	5.4 cm	6.6 %
Sublimation	0.3 cm	0.1 %	0.5 cm	0.6 %
Total melt	192.6 cm		81.7 cm	

We want to investigate the role of horizontal processes by comparing the 1D and 3D simulations. We can

compare the 3D simulations with the previously discussed 1D simulation, which include the 1D NCAR simulation that uses the same meteorological forcing data. The oceanic forcing data is different though between the simulations, since SST and SSS in the 1D simulation was based on local observations. As we expect from our previous results that the simulated ice growth and melt is very sensitive to oceanic forcing data, we compare in Table 4.1 the 3D melt/growth terms with a 1D simulation which uses the meteorological and oceanic forcing data selected from the 3D forcing fields. Including this simulation in the comparison between 1D and 3D can help us distinguish influences from horizontal processes and the oceanic forcing data set.

Table 4.1 gives the absolute and relative contribution of the different melt/growth terms for the 3D simulated domain (the domain is visualized in the sub-figure in Figure 4.9d). In addition to these growth and melt terms, horizontal transport of ice results in a net transport of 39 cm out of the domain. Congelation and new-ice formation contribute equally to the growth of the ice in the 3D domain (Table 4.1). This is different to our 1D results, which showed that congelation was always the main contributor (60-70%, Table 3.1). From our 1D results section we expect that the new-ice formation would be larger in the 3D simulation, due to the opening of the ice. Not only the opening of the ice but also the oceanic forcing data influenced here the simulated SST and therefore the new-ice formation. This is confirmed by the increased new ice formation in the 1D simulation shown in Table 4.1 compared to the 1D NCAR simulation.

The ice melt in the 3D domain is dominated by bottom melt (67.0 %). Surface melt plays a smaller role (30.5 %). The small role of surface melt is likely due to the larger snowfall in the NCAR data-set, as described in Section 3.2.2. The strong contribution of bottom melt in the 3D simulation is a large difference from all 1D simulations, which show contributions of bottom melt of only around 30% (Table 3.1 and 4.1). This indicates that not the oceanic forcing data caused this strong bottom melt, but the dynamical opening of the ice that enables heating of the ocean mixed layer. Perovich et al. (2003) found that for SHEBA the bottom and surface melt rates were comparable. Our domain averaged bottom rates might be larger since the southern part closer to the marginal ice zone is included, while the SHEBA measurements in summer were collected more northward.

In conclusion, the 1D control simulated ice thickness agreed better with the SHEBA observations than the 3D simulated ice thickness. On the other hand, the 3D simulation performs better in representing the observed snow depth. This contradicting results gives indication to an inconsistency in the snowfall and snow depth measurements. From the comparison of the 1D and 3D simulations we cannot conclude on the influence of dynamical processes on the growth terms,

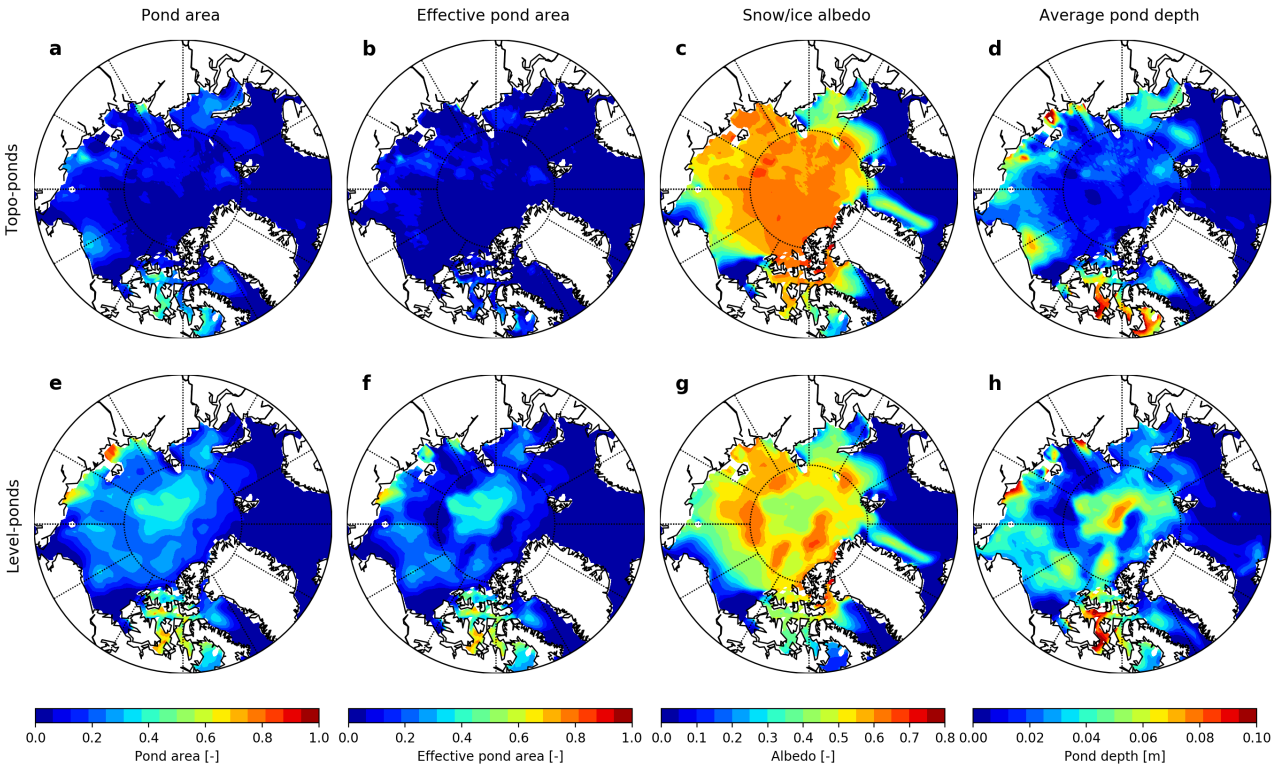

Figure 4.10 | July 1998 simulated melt ponds using the topo or level-melt pond scheme.. For both simulations the simulated fractional pond area (a,e), effective pond area (b,f), average albedo of the ice pack (c,g) and the average pond depth (d,h) are plotted.

since the oceanic forcing had a dominant influence on the new ice formation. Nevertheless, the comparison shows us that bottom melt did increase in the 3D simulation, as a result of increased heating of the surface ocean through the open water fraction.

4.5 Melt pond schemes

In Section 3.3 we discussed the impact of different melt pond schemes in the 1D simulation. Since we hypothesized that the results would be different in a 3D set up, we compare here two simulations with different melt pond parameterizations. The simulated average melt pond area, effective pond area, sea ice albedo and the average pond depth for July 1998 are presented in Figure 4.10. The top row in the figure shows the results for a simulation using the topo melt-pond scheme by Flocco and Feltham (2007), the bottom row using the level melt-pond scheme by Hunke et al. (2013). The pond area is considerably larger using the level melt-pond scheme, especially in the central Arctic (0.1 for topo, 0.5 for level-ponds). The effective pond fraction is in the same way much larger, in some areas reaching 0.6 using level-ponds while almost 0 for topo-ponds. The differences in effective pond area are also reflected in differences in simulated ice albedo. In the central Arctic the albedo differs between the two different simulations up to 0.3, being substantially higher in the topo melt-pond scheme, which can have substantial impact on the ice melt.

The lower fractions of pond area using the topo melt-pond scheme are likely caused by the critical ice lid thickness, which is a parameter for the melt pond scheme. When the ice lid thickness is larger than this parameter, penetration of radiation into the underlying pond is blocked. This in turn limits the growth of the melt pond by radiation, limiting the strength of the positive feedback (Hunke, 2013). Adjusting this critical ice lid thickness would likely result in higher pond areas. A more in depth study on the performance and tuning of this scheme is needed to fully evaluate and improve the melt pond simulations, but this is beyond the scope of this study.

The simulated pond depths at the edges of the sea ice pack are agree better between the two simulations (Figure 4.10d, h). This does not hold for the central Arctic, where the ponds are much deeper using the level-ice melt pond scheme. The level-ponds are deepest in the center of the Arctic Ocean. This result did not agree with our expectations that the deepest ponds would be located at the roughest ice (in our simulation at the coast of north Greenland and Canada, not shown). It is expected that at rougher, ridged ice, smaller areas are covered with deeper ponds (Polashenski et al., 2012; Hunke et al., 2013).

How did the simulated melt ponds affect the ice melt?

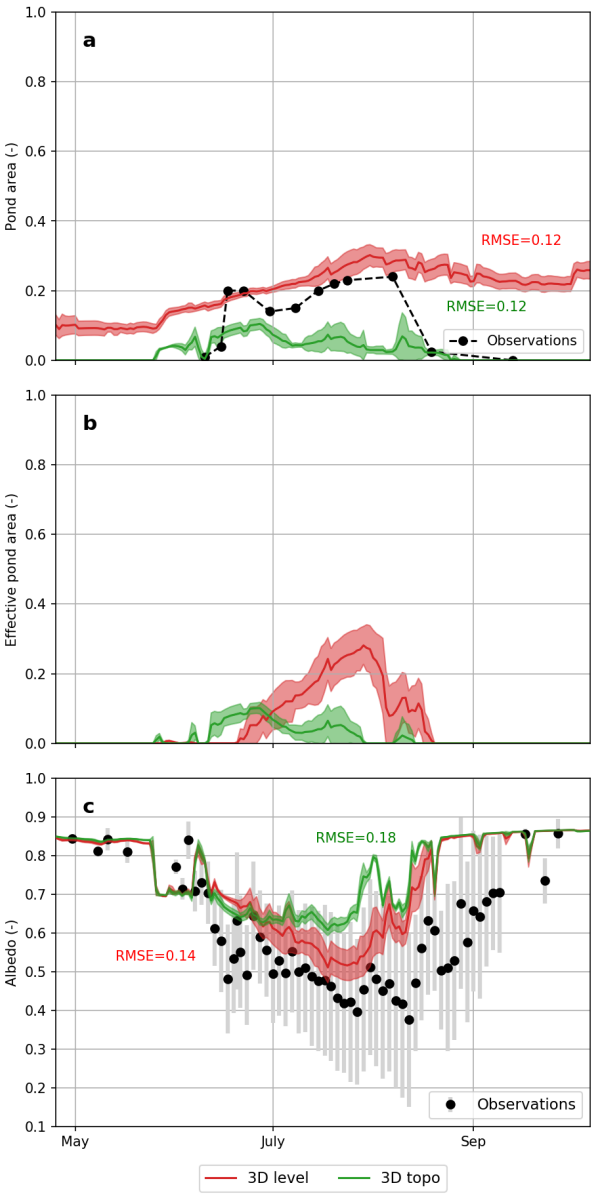

Figure 4.11 | Simulated melt pond evolution during the SHEBA melt season for the 3D and 1D simulations a) Fractional pond area, together with estimated pond fractions from aerial pictures **b)** pond area effective for the radiation calculation **c)** Snow/ice albedo, plotted against the observed albedo along a transect shown with a mean and standard deviation.

The fractional ice area and average ice thickness in September for the two simulations are given in Appendix A.8. We see that over the entire Arctic, the simulation using the level-ice pond scheme has a smaller ice area with thinner ice. The simulation with the level melt-pond scheme shows more opening of the ice in the central Arctic and more melt of the ice edge in the Beaufort Sea, reaching differences of open water fractions of 0.4. The differences in ice thickness are visible over the entire ice pack. The strongest reduced thicknesses are found in the center of the Arctic ocean, where reductions in ice thickness are up to 1m ($\pm$ 50 %). In these regions the effective pond areas and pond depths are largest, strongly

reducing the surface albedo and therefore increasing the surface melt.

To evaluate the 3D simulated pond fractions and albedos we compare the co-sampled output against the SHEBA observations in Figure 4.11. Similarly as in Section 3.3 we find the largest pond fractions using the level-pond scheme, and smaller pond fractions using the topo-pond scheme (Figure 4.11a). The topo-ponds are effective for the radiation calculation slightly earlier (Figure 4.11b). Afterwards, the level-pond simulated effective pond area increases significantly more and has therefore resulting albedos in the melting season that reach values of 0.1 lower (Figure 4.11c).

The level-pond and topo-pond scheme seems to perform comparable in representing the observed pond areas with similar RMSE values (Figure 4.11a). This is different from what we found in Section 3.3, where the topo-pond scheme performed better in simulating the pond area. It should be noted that while the pond area remains high at the end of the melting season for the level-pond scheme, the effective pond fraction decreases very similarly as the observed pond fractions. Looking at the simulated albedos, we see that the level-pond scheme performs better. A difference with the 1D simulations in Section 4.11 is that the effect of the melt ponds on the albedo at the end of the melting season is missing in the 3D simulations: where the observations show low albedo values in end of August and September, the simulated albedo increases to albedos of sea ice covered by snow (Figure 4.11c). This rather high albedo is due to the snowfall in the NCAR data set (see also Figure 3.4c).

The 3D results show here again the sensitivity of the simulated pond and albedos to the chosen pond scheme. In contrast to the 1D simulation however, the differences of the pond schemes are smaller and the level-pond simulations are closer to the observations. This can be explained by the fact that the level-ice tracer is used in the level-pond scheme, which is variable in the 3D simulation and was always 1 in 1D. Our results show the important role that melt ponds play on the summer melt season through their feedback on the radiation balance.

5 Discussion

5.1 Connection to MOSAiC

This study is a contribution to the MOSAiCs project on measurement and modelling of climate-active trace gas exchange in the Arctic. The exchange of these gases (CO_2, CH_4, DMS and O_3) in the Arctic is potentially significantly influenced by (biogeochemical) sea ice processes. The goal of this study was therefore to evaluate the thermodynamic en dynamic sea ice processes that also ultimately drive climate-active trace gas exchange, the later to be focus of follow-studies with CICE. Consequently, we discuss here the findings of this thesis in the context of studying and simulating the climate-active trace gas exchange in the Arctic.

One of the key features of the sea ice pack for gas exchange are the leads and polynyas in the ice, which provide a passage for gases between the ocean and atmosphere (Vancoppenolle et al., 2013; Steiner et al., 2013). We compared the simulated areal fraction of ice, and therefore the open water fraction, against observations. The largest discrepancies were found in the marginal ice zone around Svalbard. Detailed analysis on the lead fraction in the central Arctic was not possible with the available satellite products for the SHEBA period, since errors in observed ice concentrations are larger than the expected lead fractions. New lead detection methods provide better data-sets for the evaluation of lead fractions in the Arctic (Ivanova et al., 2016). While the EVP rheology used in CICE is able to capture some of the lead formation, the representation of the lead characteristics with often long but narrow leads is expected to increase by increasing the spatial resolution of the model (Wang et al., 2016).

Remarkable was the impact of the ocean SST restoring on the open water fraction. The results showed that chosen SST restoring timescale and the heat flux between the deep ocean and the mixed layer from the forcing fields were crucial for the simulated open water fraction in summer. A negative (downward) ocean heat flux in summer could lead to a period of SST cooling and ice growth in the open water fraction, which might strongly influence the total gas exchange in the summer period. CICE shows here a limitation regarding the simulation of leads being very sensitive to the open water fraction that can close up instantly by new ice growth. The frazil ice calculation in CICE, which calculates the new ice formation based on the energy balance, implements the new ice as a constant ice cover of 5cm. However, in reality frazil ice crystals form in the open water, can clump together and be transported to the side of the leads by the wind, remaining a fraction of open water. The frazil ice calculation is more sophisticated in the NEMO-LIM model, which uses a variable collection thickness depending, among others on windspeed. Since leads can play an important role in the exchange of gases, implementing such a 'grease' ice calculation is recommended. Wilchinsky et al. (2015) describes a improved parameterization that calculates frazil ice and grease ice in leads also being incorporated in CICE. This parameterization however was not available in the default public versions of CICE.

While our results showed that on one hand the shorter SST restoring timescale decreased the overall RMSE between observed and simulated ice concentration, on the other hand it resulted in a worse simulation of the the Laptev Sea and East Siberian Sea polynyas. Polynyas are areas of persistent open water and act as a sink for CO_2, even in winter time (Else et al., 2011). A more in depth analysis should be done to evaluate the simulation of polynyas in CICE, which is likely limited in the current CICE configuration. Since coastal polynyas occur in areas where persistent winds blow newly formed frazil ice to the leeward site, similarly as described above regarding the refreezing of leads, the representation of polynyas in CICE might not be optimal. We expect, besides these subtle, small-scale features of sea ice dynamics, that addition of an interactive ocean component will improve the simulation of Arctic polynyas, since then the interaction of brine formation and vertical mixing of the water column in coastal polynyas can be simulated.

A second important sea ice property is the presence of melt ponds. Firstly, melt ponds typically have much lower albedos than sea ice and therefore impact the surface melt of the ice strongly. The results clearly reflected this: different melt-pond parameterizations led to differences in albedo up to 0.3 and resulting ice thickness differences up to 1 m. Secondly, previous studies also showed that melt ponds play a role in the exchange of the climate-active trace gas DMS (Park et al., 2019; Vancoppenolle et al., 2013; Arrigo et al., 2012). Our evaluation on the melt pond simulation can therefore give valuable information for follow-up studies that link sea ice processes and DMS exchange. Our results show that simulated pond areas and pond depths strongly differ using the different parameterizations. Evaluating the performance of the pond area and the albedo simulation of the different schemes gave inconclusive results. Further evaluation of the albedo and melt pond simulations against observations for more recent years is needed to fully compare the performance of both parameterizations. Tuning the melt pond parameters, such as the critical ice lid thickness, can also improve the melt ponds simulation (Hunke et al., 2013). Because of the different thermodynamic and biochemical roles of melt ponds, together with their strong sensitivity to the chosen pond scheme, the simulation of melt ponds are important to consider and improve for the simulation of climate-active trace gases.

This study focuses on (thermo)dynamic sea ice processes that are likely relevant for the simulation of climate-active gas exchange in the Arctic. However,

there remains a lot of work before we can simulate the exchange of these gases through sea ice. To simulate the CO_2 exchange, a separate flux calculation over sea ice and open water should be added in the model (as suggested by Vancoppenolle et al. (2013)), since fluxes of CO_2 through sea ice can be significant (Geilfus et al., 2012). This flux can be calculated from the difference in pCO_2 between the open water/brine and atmosphere, using different transfer velocities for open water and ice. Furthermore, the earlier described sea-ice carbon pump can have regional large effects on the CO_2 budget (Moreau et al., 2016; Grimm et al., 2016). To include the effect of this pump, incorporation of the sea ice carbon chemistry in the biochemical model of CICE is required. This study lacks an evaluation of the brine processes in CICE. Duarte et al. (2017) evaluated the sea ice biochemistry in CICE for the N-ICE expedition and found simulated bulk salinities that were in good agreement with observations. Future studies that are related to the transport of biochemical tracers in the brine matrix in CICE are recommended. To explicitly simulate this carbon sink, CICE should be configured coupled to a real ocean model.

To simulate the sulfur cycling and DMS exchange through sea ice, the sulfur cycling in the biochemical model in CICE needs to be tested. The flux of DMS to the atmosphere needs to be added, with again different gas transfer velocities for DMS over open water and over sea ice. For both DMS, CO_2 as well as CH_4 it is still unknown how large the exchange of gases is through the sea ice brine - air interface. A problem that can arises for the simulation of gasses with a low solubility, is that the mushy layer theory (used in CICE) does not include the gas phase (Loose et al., 2011). In this theory sea ice is seen as microscopic brine inclusions surrounded by a matrix of pure water ice, though these brine pockets cannot become gas filled. Altogether, many different biochemical, thermodynamic and dynamic ice and ocean processes play a role in the exchange of CO_2, CH_4, DMS and O_3. It is recommended to further study what the most important drivers of this exchange are and how these processes can implemented in coupled sea-ice atmospheric chemistry models, while limiting their computational expenses.

5.2 SHEBA and MOSAiC expeditions

Given that the historic SHEBA expedition took place about 23 years ago relative to the ongoing MOSAiC expedition, it seems relevant to compare the expeditions and focus on the differences in sea ice condition. Over this 23 year period, the sea ice extent has declined and the thick multiyear ice is replaced by relatively thinner first-year ice (Onarheim et al., 2018). The amount of ice that survives the melting season is less, and the seasonal ice zone is of growing importance. The SHEBA year was though characterized by above-normal warm winter temperatures and ice concentrations in August and September 1998 were record low (Drobot et al., 2003). The ice conditions around the SHEBA ice camp were also characterized by abnormally low MYI concentrations (Drobot et al., 2003). Despite the fact that his rather extreme year was not representative for the climatology, it can be better related to the ice conditions under the current changing climate and to the MOSAiC project.

Still, differences in the sea ice processes can be expected between the SHEBA and MOSAiC expedition. Perovich et al. (2003) found comparable amounts of surface and bottom melt for the SHEBA melt period. Our modelling results showed that the dynamical opening of the ice, together with the oceanic forcing played an important role in the bottom and lateral melt contribution. We can expect different contributions of the melt components for the MOSAiC expedition. Where surface melt was the dominant melt term in the 20th century, bottom melt shows a growing contribution to the total melt (Richter-Menge et al., 2006; Tsamados et al., 2015). Measurements on the relative contribution of the melt terms in the Arctic are sparse, still the observed decrease in ice area, climate warming and possible increase in storm events are expected to increase the bottom melt contribution (Perovich et al., 2014). The MOSAiC expedition will likely make a transpolar drift in areas with predominately thin ice (DuVivier et al., 2019). Also changes in the Arctic ice pack showed an increasing contribution of thin FYI (Maslanik et al., 2007). These differences in location and time with the SHEBA expedition give likely a different ice response, with ice that might move faster, break up easier and that has a longer melt season.

5.3 The challenge of evaluating 3D simulations with local observations

The Arctic Ocean is a region of sparse in-situ observations. Arctic-wide observations are available from satellite derived products, such as ice concentration (since 1979, Breivik et al. (2009)) and estimates of ice thickness (since 2003, Laxon et al. (2003)). While these satellite products are valuable to assess the Arctic-wide ice pack, they have as disadvantage a rather coarse true resolution ($\sim$ 50km) that does not resolve the local scale variation in ice concentration. Besides, the timing of the seasonal cycles in these pan-Arctic fields do not accurately represent the seasonal cycle for a specific ice floe (DuVivier et al., 2019). The SHEBA expedition provided a unique data set of various in situ sea ice measurements over a full seasonal cycle. The combination of measurements in the ocean, ice and atmosphere during this drifting experiment make the data-set very

suitable to evaluate 1D simulations forced by local measurements. Our 1D simulation was in this way set up as a Lagrangian experiment, where both ocean and meteorological forcing as well as the ice evaluation data was measured when following an the ice floe.

Drifting expeditions, such as SHEBA and MOSAiC, are very suitable to evaluate a 1D simulation. Using such local observations though for evaluation of 3D simulations can be more tricky. In this study we use two methods. Firstly the co-sampling strategy, where the output was selected for the grid cells closest to the SHEBA drift location. Secondly, the output was averaged over a larger domain enclosing the entire SHEBA trajectory. Evaluating the co-sampled grid cells with the SHEBA observations tells us how well the simulation represents the observed ice conditions for this specific location at that specific time. Whether the evaluation results can tell us something about how well the evolution of the ice pack is represented in the simulation, is questionable. We take as example the evaluation of ice thickness: while the SHEBA observations show us the evolution of ice thickness of one single ice floe over the entire period, the selected grid cells might represent the ice thickness of different ice floes at different time steps. To be able to evaluate the changes of purely a single ice floe, the simulated ice velocity field should match the observed drift of the SHEBA ice camp.

A way to test the validity of our method is by Lagrangian tracking of the sea ice in the simulated ice velocity field, from the start location of the SHEBA expedition (75.6 N, -144.0 E). Figure 5.1 shows in blue these computed trajectories using the Python package OceanParcels created by Sebille et al. (2019). This Lagrangian tracking approach indicates that the sea ice drifts in direction of the Chukchi Sea, instead of north westward as the SHEBA expedition. The results from backward tracking are shown in orange and show where the ice at the end location of SHEBA came from. Both trajectories show that the CICE simulated ice velocity field does not reproduce the drift of the SHEBA ice camp. The observed track of the SHEBA expedition is mainly driven by the Beaufort Gyre, but shows a northward movement that is a-typical for the Beaufort Sea (Drobot et al., 2003). Since the ship trajectory is largely driven by oceanic circulation, a feature not represented in our simulations used in this thesis study, an additional run was done which uses the ocean currents from the POP climatological data set (red an cyan in Figure 5.1). However, the addition of ocean currents does not make a large difference for the trajectories. Drobot et al. (2003) compared the SHEBA drift to hypothetical drifts from the SHEBA start location for different years, and found that most years the drift was westward, in direction of the Chukchi Sea. This agrees with our foreward derived trajectory and indicates that the SHEBA drift is not represented by the climatological ocean currents.

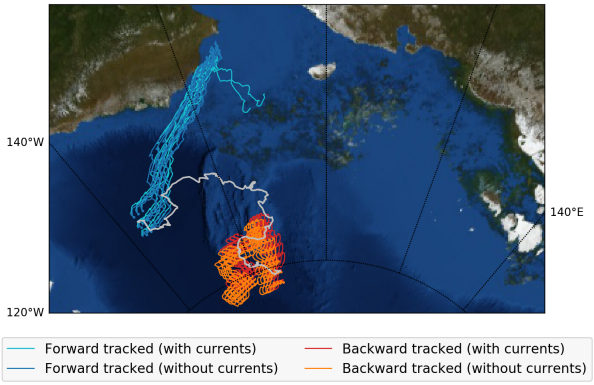

Figure 5.1 | Lagrangian forward and backward tracked sea ice trajectories. Tracking is based on the CICE simulated ice velocity field. Forward tracking was done from 9 grid cells around the SHEBA start location, backward tracking from 9 grid cells around the SHEBA end location. In white is shown the SHEBA ship trajectory.

A second method we used to compare the 3D simulated field against local SHEBA observations, is by evaluating the averaged model output over a larger domain that encloses the entire SHEBA trajectory. This method has as advantage that sudden changes in the diagnostic variables due to the co-sampling are averaged out, which enables to evaluate the mass balance of growth and melt terms for the domain. Evaluating the mass balance for the co-sampled grid cells is in contrast not possible, because the co-sampled melt and growth terms cannot explain the co-sampled ice volume changes. However, with the domain method we loose a lot of information on the sub-domain heterogeneity. Our results showed that especially in the summer this heterogeneity is considerable. The standard deviation of ice thickness within the domain in September was 70% of the mean ice thickness.

An alternative way to evaluate the 3D simulation against local ship observations, is by evaluating an ensemble of Lagrangian tracked sea ice floes. DuVivier et al. (2019) state to rather use these ice floes ensembles than regional averages to compare drift observations with simulations. In light of the MOSAiC project that will soon provide us with a large data set on ocean, ice and atmospheric measurements, it is important to consider the most optimal approach to make use of the data for model evaluation and model improvement. We show here that it is likely better to use Lagrangian tracked sea ice floes to evaluate models than selecting the observations locations from the simulation fields. However, for both methods to compare the 'same' ice in observations and simulations, it is important to have an accurate simulation of the ice velocity field. This points out once more the challenge in comparing local sea ice observations with model derived fields in the Arctic.

5.4 Evaluation in a stand-alone set up

In this study the CICE model is evaluated as a stand-alone sea ice model, where atmospheric an oceanic data is given as forcing data. The motivation of this study was to evaluate the CICE model for a potential coupling with WRF-CHEM. Since establishing this coupling between the CICE model and WRF-CHEM was definitely not possible within the time frame of this thesis study, we evaluated CICE as stand-alone sea ice model. This study gave us helpful insight in the representation of the sea ice processes and in the response of the simulated ice properties to forcing data and several model parameterizations in CICE. Furthermore, in the stand-alone set-up we were able to analyze a full seasonal cycle for the entire Arctic ocean. Assessing a simulation on this timescale and spatial scale would, also due to computational costs, not been possible using a coupled set-up with WRF-CHEM.

Our results show the sensitive response of the ice pack to the atmospheric and oceanic forcing data-sets. To illustrate this, the snowfall from the forcing data determined the onset and therefore total melt of the melting season. Even more sensitive was the formation of ice to the restoring of the SST from the forcing data. The importance of the SST restoring scheme in stand-alone set-up of the modelling system was also found by Tsamados et al. (2015) in a study running CICE for 24 years. The fact that our simulation shows this strong sensitivity to the forcing data, draws the importance of coupling the simulation of sea ice dynamics to the atmosphere and ocean models. Hunke (2010) found similarly that the accuracy of the external forcing data was most crucial to arrive at realistic simulations with sea ice models.

A limitation of our uncoupled approach is that is that it does not have a complete representation of the feedbacks between the ice, atmosphere and ocean. In an 'online' coupling between the atmosphere and the CICE model, variables such as the wind velocity, air humidity and density, temperature, radiation and precipitation will be provided by the atmospheric model. The other way around, using the standard CICE coupling method, the sea ice model provides the surface temperature, and outgoing radiative, turbulent and conductive fluxes to the atmospheric model (West et al., 2016). Besides interaction in the surface exchange of heat and moisture, interactions with the air-chemistry in WRF-CHEM are possible as well, such as the effects of dust and aerosols on the ice melt (Hunke et al., 2010). A coupled model set-up allows these coupled feedbacks to act, which can significantly change the ice response (e.g. melt pond formation). Therefore, full evaluation of a sea ice model should be done in a coupled context (Hunke, 2010). To use CICE in a coupled setting with WRF-CHEM to study the exchange of climate-active trace gases in the Arctic, validation of the relevant sea ice processes should be done in the coupled CICE-WRF configuration.

6 Conclusion

The aim of this study was to evaluate the CICE simulated thermodynamic and dynamic sea ice processes that ultimately drive climate-active trace gas exchange in the Arctic. Previous studies have shown that ice growth and melt, formation of leads, polynyas and melt ponds are important processes for this exchange. Both 1D and 3D simulations were set up for the period of the SHEBA expedition (Oct 1997 - Oct 1998), to evaluate the CICE simulations for a full seasonal cycle.

To evaluate the representation of the growth and melt of sea ice in CICE, the 1D and 3D simulated ice thickness was evaluated against SHEBA observations by Perovich et al. (2003). We found that the 1D simulated ice thickness based on local forcing data agreed well with observed ice thickness (RMSE 14 cm). Co-sampled 3D output along the SHEBA trajectory showed a much larger error with the observed ice thickness (RMSE 65 cm). In contrast to the ice thickness, 1D simulated snow depth was considerably lower than most observations. The 3D simulated snow depth on the other hand agreed better with the observations (RMSE 8 cm). This difference in performance of the snow and ice simulation indicated a inconsistency in the evaluation data set.

While lead formation is not represented in the 1D set-up with solely vertical processes, the influence of lead formation on the ice simulation was tested in a 1D set-up by an additional input of opening and closing rates. The opening of the ice pack caused a stronger contribution of bottom and lateral melt to the total ice melt, through the surface water heating in the open water fraction. This relative lower contribution of surface melt agreed better with the contributions found by Perovich et al. (2003). Detailed evaluation of lead formation in CICE was limited, since the available Arctic ice concentration product had larger errors than the expected lead fractions in the central Arctic. The simulation of polynyas in CICE is limited because of the absence of wind effects on frazil ice in CICE. Still, good agreement was found between the simulated and observed Arctic ice concentration (RMSE 0.1). The largest errors were found in the marginal ice zone, especially in the Fram Strait, Barents Sea and west of Greenland, where the simulated outflow of ice was too large.

The simulated melt-pond characteristics in both the 1D and 3D simulations were very sensitive to the chosen melt pond parameterization. The level-melt ponds gave the largest pond fraction, up to 0.8, which is considerably larger then the maximum observed pond fraction of 0.4. Despite some of these discrepancies regarding the representation of melt ponds, the albedos fall mostly within the range of the observations. The 3D simulation showed though that the simulated July albedo had differences as large as 0.3 in the central Arctic between the melt pond parameterizations. These large albedo differences had a strong impact on the summer ice melt.

Besides this evaluation of different sea ice processes, we tested in this study the influence of atmospheric and oceanic forcing data on the sea ice simulation. 1D simulations forced with local observed meteorology were compared to simulations forced by model output from ECMWF and NCAR. The largest differences were visible when the NCAR data was used: the higher snowfall amounts resulted in a delayed and shorter surface melt period, decreased melt pond formation and as result of that a thicker ice pack at the end of the melt season. This showed the strong impact of snowfall amounts on the sea ice simulation.

The 3D simulation showed us also a strong influence of the oceanic forcing data on the ice concentration. The timescale of SST restoring influenced the importance of the input ocean heat flux, that strongly influenced the ice area in the melting season. In this period, small differences in the simulated SST can be critical to (not) reach the freezing temperature, and therefore strongly impact the open water fraction.

Overall, our analysis gives a detailed evaluation of the key sea ice processes in CICE against local observations. Our evaluation also demonstrated the challenge of comparing 3D simulations with local observations. Using tracking algorithms to evaluate individual ice floes against drift observations is an alternative method that we advice for future studies. We conclude that the CICE simulated ice concentrations, albedo and thicknesses agree reasonably well with observations. Though we find a strong sensitivity of these features to the forcing data sets as well as to melt pond parameterizations. Next steps to improve the simulation of exchange of climate-active trace gases with CICE is to evaluate and improve the biochemistry in CICE. Then, CICE can be coupled, with addition of flux calculations through ice, to an atmospheric chemistry component to simulate Arctic climate-active trace gas exchange.

7 Acknowledgments

I like to thank first of all Laurens for his supervision and enthusiasm during my thesis project. I am very thankful for the freedom you gave me to work on a topic I am passionate about. I would like to thank Elizabeth Hunke for her feedback on my thesis work. I would also like to thank Sinclair and Sjoerd for their help with the HPC and debugging the code to get CICE running. I am thankful for the friends at the thesis penthouse, with whom I could always laugh in the coffee breaks and afternoon drinks. Lastly, without my housemates the last phase of home working on my thesis would have been not nearly as nice as it was now.

References

Arrigo, K. R., Perovich, D. K., Pickart, R. S., Brown, Z. W., Van Dijken, G. L., Lowry, K. E., Mills, M. M., Palmer, M. A., Balch, W. M., Bahr, F., Bates, N. R., Benitez-Nelson, C., Bowler, B., Brownlee, E., Ehn, J. K., Frey, K. E., Garley, R., Laney, S. R., Lubelczyk, L., Mathis, J., Matsuoka, A., Mitchell, B. G., Moore, G. W. K., Ortega-Retuerta, E., Pal, S., Polashenski, C. M., Reynolds, R. A., Schieber, B., Sosik, H. M., Stephens, M., and Swift, J. H. (2012). Massive Phytoplankton Blooms Under Arctic Sea Ice. DOI: 10.5061/dryad.4dn793t6.

Bitz, C. M. and Lipscomb, W. H. (1999). An energy-conserving thermodynamic model of sea ice. *Journal of Geophysical Research: Oceans*, 104(C7):15669–15677, DOI: 10.1029/1999jc900100.

Boucher, O., Moulin, C., Belviso, S., Aumont, O., Bopp, L., Cosme, E., Von Kuhlmann, R., Lawrence, M. G., Pham, M., Reddy, M. S., Sciare, J., and Venkataraman, C. (2003). DMS atmospheric concentrations and sulphate aerosol indirect radiative forcing: a sensitivity study to the DMS source representation and oxidation. *Atmospheric Chemistry and Physics*, 3:49–65, www.atmos-chem-phys.org/acp/3/49/.

Breivik, L.-A., Carrieres, T., Eastwood, S., Fleming, A., Girard-Ardhuin, F., Karvonen, J., Kwok, R., Meier, W. N., Mäkynen, M., Pedersen, L. T., Sandven, S., Similä, M., and Tonboe, R. (2009). Remote sensing of sea ice. http://www.jaxa.jp/projects/sat/gcom/.

Bretherton, C. (2007). Model ECMWF Column Output (netCDF). Version 1.0. UCAR/NCAR - Earth Observing Laboratory. DOI: https://doi.org/10.5065/D61G0JPN.

Briegleb, B. P. and Light, B. (2007). A Delta-Eddington Multiple Scattering Parameterization for Solar Radiation in the Sea Ice Component of the Community Climate System Model. Technical report, National Center for Atmospheric Research, Boulder, Colorado.

Bromwich, D. H., Hines, K. M., and Bai, L. S. (2009). Development and testing of Polar Weather Research and Forecasting model: 2. Arctic Ocean. *Journal of Geophysical Research Atmospheres*, 114(8), ISSN: 01480227, DOI: 10.1029/2008JD010300.

Carton, J. A. and Giese, B. S. (2008). A Reanalysis of Ocean Climate Using Simple Ocean Data Assimilation (SODA). *Monthly Weather Review*, 136(8):2999–3017, ISSN: 0027-0644, DOI: 10.1175/2007MWR1978.1.

CICE Consortium (2019). CICE Documentation . Technical report, Los Alamos National Laboratory.

CICE-Consortium (2020a). CICE gx1 COREII Forcing Data - 2020.03.20. DOI: 10.5281/ZENODO.3731012.

CICE-Consortium (2020b). Icepack Forcing Data - 2020.03.26. DOI: 10.5281/ZENODO.3728287.

Damm, E., Bauch, D., Krumpen, T., Rabe, B., Korhonen, M., Vinogradova, E., and Uhlig, C. (2018). The Transpolar Drift conveys methane from the Siberian Shelf to the central Arctic Ocean. *Scientific Reports*, 8(1):1–10, ISSN: 20452322, DOI: 10.1038/s41598-018-22801-z.

Dmitrenko, I., Hölemann, J. A., Tyshko, K., Churun, V., Kirillov, S., and Kassens, H. (2001). The Laptev Sea flaw polynya, Russian Arctic: effects on the mesoscale hydrography. *Annals of Glaciology*, 33.

Drobot, S. D., Maslanik, J. A., and Fowler, C. (2003). Atmospheric and Sea Ice Conditions During the Sheba Year: Historical and Spatial Assessment. *Polar Geography*, 27(1):15–37, ISSN: 19390513, DOI: 10.1080/789610220.

Duarte, P., Meyer, A., Olsen, L. M., Kauko, H. M., Assmy, P., Rösel, A., Itkin, P., Hudson, S. R., Granskog, M. A., Gerland, S., Sundfjord, A., Steen, H., Hop, H., Cohen, L., Peterson, A. K., Jeffery, N., Elliott, S. M., Hunke, E. C., and Turner, A. K. (2017). Sea ice thermohaline dynamics and biogeochemistry in the Arctic Ocean: Empirical and model results. *Journal of Geophysical Research: Biogeosciences*, 122(7):1632–1654, ISSN: 2169-8961, DOI: 10.1002/2016JG003660@10.1002/(ISSN)2169-9291.NICE1.

DuVivier, A. K., DeRepentigny, P., Holland, M. M., Webster, M., Kay, J. E., and Perovich, D. (2019). Going with the floe: tracking CESM Large Ensemble sea ice in the Arctic provides context for ship-based observations. *The Cryosphere Discussions*, pages 1–20, ISSN: 1994-0416, DOI: 10.5194/tc-2019-145.

Elliott, S., Deal, C., Humphries, G., Hunke, E., Jeffery, N., Jin, M., Levasseur, M., and Stefels, J. (2012). Pan-Arctic simulation of coupled nutrient-sulfur cycling due to sea ice biology: Preliminary results. *Journal of Geophysical Research: Biogeosciences*, 117(1), ISSN: 01480227, DOI: 10.1029/2011JG001649.

Else, B. G., Papakyriakou, T. N., Galley, R. J., Drennan, W. M., Miller, L. A., and Thomas, H. (2011). Wintertime CO2 fluxes in an Arctic polynya using eddy covariance: Evidence for enhanced air-sea gas transfer during ice formation. *Journal of Geophysical Research: Oceans*, 116(9), DOI: 10.1029/2010JC006760.

Else, B. G. T., Papakyriakou, T. N., Granskog, M. A., and Yackel, J. J. (2008). Observations of sea surface fCO2 distributions and estimated air-sea CO2 fluxes in the Hudson Bay region (Canada) during the open water season. *Journal of Geophysical Research*, 113(C8):C08026, DOI: 10.1029/2007JC004389.

Feltham, D. L., Untersteiner, N., Wettlaufer, J. S., and Worster, M. G. (2006). Sea ice is a mushy layer. *Geophysical Research Letters*, 33(14), ISSN: 00948276, DOI: 10.1029/2006GL026290.

Flocco, D. and Feltham, D. L. (2007). A continuum model of melt pond evolution on Arctic sea ice. *Journal of Geophysical Research*, 112(C8):C08016, ISSN: 0148-0227, DOI: 10.1029/2006JC003836.

Forster, P., Ramaswamy, V., Artaxo, P., Berntsen, T., Betts, R., Fahey, D., Haywood, J., Lean, J., Lowe, D., Myhre, G., Nganga, J., Prinn, R., Raga, G., Schulz, M., and Van Dorland, R. (2007). Changes in Atmospheric Constituents and in Radiative Forcing. In Solomon, S., Qin, D., Manning, M., Chen, Z., Marquis, M., Averyt, K., Tignor, M., and Miller, H., editors, *Climate Change 2007: The Physical Science Basis. Contribution of Working Group I to the Fourth Assessment Report of the Intergovernmental Panel on Climate Change*. Cambridge University Press, Cambridge, United Kingdom and New York, NY, USA.

Ganzeveld, L., Helmig, D., Fairall, C. W., Hare, J., and Pozzer, A. (2009). Atmosphere-ocean ozone exchange: A global modeling study of biogeochemical, atmospheric, and waterside turbulence dependencies. *Global Biogeochemical Cycles*, 23(4), ISSN: 08866236, DOI: 10.1029/2008GB003301.

Geilfus, N. X., Carnat, G., Papakyriakou, T., Tison, J. L., Else, B., Thomas, H., Shadwick, E., and Delille, B. (2012). Dynamics of pCO2 and related air-ice CO2 fluxes in the Arctic coastal zone (Amundsen Gulf, Beaufort Sea). *Journal of Geophysical Research: Oceans*, 117(2), ISSN: 21699291, DOI: 10.1029/2011JC007118.

Gourdal, M., Lizotte, M., Massé, G., Gosselin, M., Poulin, M., Scarratt, M., Charette, J., and Levasseur, M. (2018). Dimethyl sulfide dynamics in first-year sea ice melt ponds in the Canadian Arctic Archipelago. *Biogeosciences*, 15:3169–3188, DOI: 10.5194/bg-15-3169-2018.

Grell, G. A., Peckham, S. E., Schmitz, R., McKeen, S. A., Frost, G., Skamarock, W. C., and Eder, B. (2005). Fully coupled "online" chemistry within the WRF model. *Atmospheric Environment*, ISSN: 13522310, DOI: 10.1016/j.atmosenv.2005.04.027.

Grimm, R., Notz, D., Glud, R. N., Rysgaard, S., and Six, K. D. (2016). Assessment of the sea-ice carbon pump: Insights from a three-dimensional ocean-sea-ice-biogeochemical model (MPIOM/HAMOCC). *Elementa*, 4, DOI: 10.12952/journal.elementa.000136.

Hayashida, H., Steiner, N., Monahan, A., Galindo, V., Lizotte, M., and Levasseur, M. (2017). Implications of sea-ice biogeochemistry for oceanic production and emissions of dimethyl sulfide in the Arctic. *Biogeosciences*, 14(12):3129–3155, ISSN: 17264189, DOI: 10.5194/bg-14-3129-2017.

Hibler, W. D. (1979). A Dynamic Thermodynamic Sea Ice Model. *Journal of Physical Oceanography*, 9(4):815–846, ISSN: 0022-3670, DOI: 10.1175/1520-0485(1979)009<0815:adtsim>2.0.co;2.

Hunke, E. (2013). Weighing the importance of surface forcing on sea ice - A September 2007 CICE modeling study. In *ECMWF-WWRP/THORPEX Workshop on Polar Prediction*.

Hunke, E., Allard, R., Bailey, D. A., Blain, P., Bouchat, A., Craig, T., Dupont, F., DuVivier, A., Grumbine, R., Hebert, D., Holland, M., Jeffery, N., Lemieux, J.-F., Rasmussen, T., Ribergaard, M., Roberts, A., Turner, M., and Winton, M. (2019a). CICE-Consortium/CICE: CICE Version 6.0.1. DOI: 10.5281/ZENODO.3351684.

Hunke, E., Allard, R., Bailey, D. A., Blain, P., Craig, T., Dupont, F., DuVivier, A., Grumbine, R., Hebert, D., Holland, M., Jeffery, N., Lemieux, J.-F., Rasmussen, T., Ribergaard, M., Roberts, A., Turner, M., and Winton, M. (2019b). CICE-Consortium/Icepack: Icepack1.1.1. DOI: 10.5281/ZENODO.3251032.

Hunke, E. C. (2010). Thickness sensitivities in the CICE sea ice model. *Ocean Modelling*, 34:137–149, DOI: 10.1016/j.ocemod.2010.05.004.

Hunke, E. C. and Bitz, C. M. (2009). Age characteristics in a multidecadal Arctic sea ice simulation. *Journal of Geophysical Research*, 114(C8):C08013, ISSN: 0148-0227, DOI: 10.1029/2008JC005186.

Hunke, E. C. and Dukowicz, J. K. (1997). An elastic-viscous-plastic model for sea ice dynamics. *Journal of Physical Oceanography*, 27(9):1849–1867, DOI: https://doi.org/10.1175/1520-0485(1997)027%3C1849:AEV

Hunke, E. C., Hebert, D. A., and Lecomte, O. (2013). Level-ice melt ponds in the Los Alamos sea ice model, CICE. *Ocean Modelling*, 71:26–42, ISSN: 14635003, DOI: 10.1016/j.ocemod.2012.11.008.

Hunke, E. C., Lipscomb, W. H., and Turner, A. K. (2010). Sea-ice models for climate study: Retrospective and new directions. *Journal of Glaciology*, 56(200):1162–1172.

Huwald, H., Tremblay, L.-B., and Blatter, H. (2005). Reconciling different observational data sets from Surface Heat Budget of the Arctic Ocean (SHEBA) for model validation purposes. *Journal of Geophysical Research*, 110(C5), ISSN: 0148-0227, DOI: 10.1029/2003JC002221, http://doi.wiley.com/10.1029/2003JC002221.

Ivanova, N., Rampal, P., and Bouillon, S. (2016). Error assessment of satellite-derived lead fraction in the Arctic. *The Cryosphere*, 10:585–595, DOI: 10.5194/tc-10-585-2016.

Jeffery, N., Elliott, S. M., Hunke, E. C., Lipscomb, W. H., and Turner, A. K. (2016). Title: Biogeochemistry of CICE: the Los Alamos Sea Ice Model Documentation and Software User's Manual zbgc_colpkg modifications to Version 5 . Technical report, Los Alamos National Laboratory.

Jin, M., Deal, C., Lee, S. H., Elliott, S., Hunke, E., Maltrud, M., and Jeffery, N. (2012). Investigation of Arctic sea ice and ocean primary production for the period 1992-2007 using a 3-D global ice-ocean ecosystem model. *Deep-Sea Research Part II: Topical Studies in Oceanography*, ISSN: 09670645, DOI: 10.1016/j.dsr2.2011.06.003.

Kirst, G. O., Thiel, C., Wolff, H., Nothnagel, J., Wanzek, M., and Ulmke, R. (1991). Dimethylsulfoniopropionate (DMSP) in icealgae and its possible biological role. *Marine Chemistry*, 35(1-4):381–388, ISSN: 03044203, DOI: 10.1016/S0304-4203(09)90030-5.

Kort, E. A., Wofsy, S. C., Daube, B. C., Diao, M., Elkins, J. W., Gao, R. S., Hintsa, E. J., Hurst, D. F., Jimenez, R., Moore, F. L., Spackman, J. R., and Zondlo, M. A. (2012). Atmospheric observations of Arctic Ocean methane emissions up to 82 degree north. *Nature Geoscience*, 5, DOI: 10.1038/NGEO1452.

Large, W. G. and Yeager, S. G. (2008). The global climatology of an interannually varying air - sea flux data set. *Climate Dynamics*, 33:341–364, DOI: 10.1007/s00382-008-0441-3.

Laxon, S., Peacock, H., and Smith, D. (2003). High interannual variability of sea ice thickness in the Arctic region. *Nature*, 425(6961):947–950, ISSN: 00280836, DOI: 10.1038/nature02050.

Levasseur, M., Gosselin, M., and Michaud, S. (1994). A new source of dimethylsulfide (DMS) for the arctic atmosphere: ice diatoms. *Marine Biology*, 121(2):381–387, ISSN: 00253162, DOI: 10.1007/BF00346748.

Liang, X.-Z., Pan, J., Kunkel, K., Wang, J. X. L., Hunke, E. C., and Lipscomb, W. H. (2004). Coupling the CWRF with the CICE for Arctic climate applications. *Preprints of the 5th WRF/14th MM5 User's Workshop*, pages 22–25, http://www.wrf-model.org/.

Lipscomb, W. H. (2001). Remapping the thickness distribution in sea ice models. *Journal of Geophysical Research: Oceans*, 106(C7):13989–14000, DOI: 10.1029/2000jc000518.

Loose, B., Miller, L. A., Elliott, S., and Papakyriakou, T. (2011). Sea ice biogeochemistry and material transport across the frozen interface. *Oceanography*, 24(3):202–218, ISSN: 10428275, DOI: 10.5670/oceanog.2011.72.

Maslanik, J. A., Fowler, C., Stroeve, J., Drobot, S., Zwally, J., Yi, D., and Emery, W. (2007). A younger, thinner Arctic ice cover: Increased potential for rapid, extensive sea-ice loss. *Geophysical Research Letters*, 34(24), ISSN: 00948276, DOI: 10.1029/2007GL032043.

McPhee, M. (2007). Ice Camp Ocean Turbulence Mast Data [McPhee, M.]. 1.0. DOI: https://doi.org/doi:10.5065/D6XW4H6P.

Miller, L. A., Papakyriakou, T. N., Collins, R. E., Deming, J. W., Ehn, J. K., Macdonald, R. W., Mucci, A., Owens, O., Raudsepp, M., and Sutherland, N. (2011). Carbon dynamics in sea ice: A winter flux time series. *Journal of Geophysical Research*, 116(C2):C02028, ISSN: 0148-0227, DOI: 10.1029/2009JC006058.

Moreau, S., Vancoppenolle, M., Bopp, L., Aumont, O., Madec, G., Delille, B., Tison, J. L., Barriat, P. Y., and Goosse, H. (2016). Assessment of the sea-ice carbon pump: Insights from a three-dimensional ocean-sea-ice biogeochemical model (NEMO-LIM-PISCES). *Elementa*, 2016, ISSN: 23251026, DOI: 10.12952/journal.elementa.000122.

Onarheim, I. H., Eldevik, T., Smedsrud, L. H., and Stroeve, J. C. (2018). Seasonal and regional manifestation of Arctic sea ice loss. *Journal of Climate*, 31(12):4917–4932, ISSN: 08948755, DOI: 10.1175/JCLI-D-17-0427.1.

OSI SAF (2016). Global Sea Ice Concentration climate data record release 1.1 (period 1978-2009) - DMSP, EUMETSAT SAF on Ocean and Sea Ice. http://dx.doi.org/10.15770/EUM_SAF_OSI_0001.

Park, K., Kim, I., Choi, J. O., Lee, Y., Jung, J., Ha, S. Y., Kim, J. H., and Zhang, M. (2019). Unexpectedly high dimethyl sulfide concentration in high-latitude Arctic sea ice melt ponds. *Environmental Science: Processes and Impacts*, 21(10):1642–1649, ISSN: 20507895, DOI: 10.1039/c9em00195f.

Perovich, D., Grenfell, T. C., Light, B., Richter-Menge, J., and Tucker, W. (2007a). Ice Mass Balance. Arctic Data Center. DOI: doi.org/10.5065/D6H130DF.

Perovich, D., Grenfell, T. C., Light, B., Richter-Menge, J., and Tucker, W. B. (2007b). Wavelength-integrated Albedos. Arctic Data Center. DOI: doi.org/10.5065/D6SB444G.

Perovich, D., Richter-Menge, J., Polashenski, C., Elder, B., Arbetter, T., and Brennick, O. (2014). Sea ice mass balance observations from the North Pole Environmental Observatory. *Geophysical Research Letters*, 41(6):2019–2025, ISSN: 00948276, DOI: 10.1002/2014GL059356.

Perovich, D., Richter-Menge, J., Tucker, W., Elder, B., and Bosworth, B. (2007c). Snow and Ice Temperature Profiles. Arctic Data Center. DOI: 10.5065/D6KS6PZ7.

Perovich, D. K. and Elder, B. C. (2001). Temporal evolution of Arctic sea-ice temperature. *Annals of Glaciology*, 33.

Perovich, D. K., Grenfell, T. C., Light, B., and Hobbs, P. V. (2002a). Seasonal evolution of the albedo of multiyear Actic sea ice. *Journal of Geophysical Research C: Oceans*, 107(10), ISSN: 01480227, DOI: 10.1029/2000jc000438.

Perovich, D. K., Grenfell, T. C., Richter-Menge, J. A., Light, B., Tucker, W. B., and Eicken, H. (2003). Thin and thinner: Sea ice mass balance measurements during SHEBA. *Journal of Geophysical Research C: Oceans*, 108(3):26–1, ISSN: 01480227, DOI: 10.1029/2001jc001079.

Perovich, D. K., Tucker, W. B., and Ligett, K. A. (2002b). Aerial observations of the evolution of ice surface conditions during summer. *Journal of Geophysical Research C: Oceans*, 107(10):24–1, ISSN: 01480227, DOI: 10.1029/2000jc000449.

Polashenski, C., Perovich, D., and Courville, Z. (2012). The mechanisms of sea ice melt pond formation and evolution. *Journal of Geophysical Research: Oceans*, 117(C1), ISSN: 01480227, DOI: 10.1029/2011JC007231.

Richter-Menge, J. A., Perovich, D. K., Elder, B. C., Claffey, K., Rigor, I., and Ortmeyer, M. (2006). Ice mass-balance buoys: a tool for measuring and attributing changes in the thickness of the Arctic sea-ice cover. *Annals of Glaciology*, 44, http://iabp.apl.washington.edu/.

Rysgaard, S., Bendtsen, J., Delille, B., Dieckmann, G. S., Glud, R. N., Kennedy, H., Mortensen, J., Papadimitriou, S., Thomas, D. N., and Tison, J.-L. (2011). Sea ice contribution to the air-sea CO2 exchange in the Arctic and Southern Oceans. *Tellus B: Chemical and Physical Meteorology*, 63(5):823–830, DOI: 10.1111/j.1600-0889.2011.00571.x.

Sebille, E. v., Delandmeter, P., Lange, M., Rath, W., Phillips, J. S., Simnator101, pdnooteboom, Kronborg, J., Thomas-95, Wichmann, D., nathanieltarshish, Busecke, J., Edwards, R., Sterl, M., Walbridge, S., Kaandorp, M., hart-davis, Miron, P., IsoldeGlissenaar, Vettoretti, G., and Ham, D. A. (2019). OceanParcels/parcels: Parcels v2.0.0: a Lagrangian Ocean Analysis tool for the petascale age. DOI: 10.5281/ZENODO.3257432.

Serreze, M. C. and Stroeve, J. (2015). Arctic sea ice trends, variability and implications for seasonal ice forecasting. *Philosophical Transactions of the Royal Society A: Mathematical, Physical and Engineering Sciences*, 373(2045), ISSN: 1364503X, DOI: 10.1098/rsta.2014.0159.

Shakhova, N., Semiletov, I., Sergienko, V., Lobkovsky, L., Yusupov, V., Salyuk, A., Salomatin, A., Chernykh, D., Kosmach, D., Panteleev, G., Nicolsky, D., Samarkin, V., Joye, S., Charkin, A., Dudarev, O., Meluzov, A., and Gustafsson, O. (2015). The East Siberian Arctic Shelf: towards further assessment of permafrost-related methane fluxes and role of sea ice. *Philosophical Transactions of the Royal Society A: Mathematical, Physical and Engineering Sciences*, 373(2052):20140451, ISSN: 1364-503X, DOI: 10.1098/rsta.2014.0451.

Simpson, W. R., Carlson, D., Hönninger, G., Douglas, T. A., Sturm, M., Perovich, D., and Platt, U. (2007). First-year sea-ice contact predicts bromine monoxide (BrO) levels at Barrow, Alaska better than potential frost flower contact. *Atmospheric Chemistry and Physics*, 7:621–627, www.atmos-chem-phys.net/7/621/2007/.

Stanton, T. P. and Shaw, W. J. (2007). Ice Camp Ocean Seacat CTD Data-Deep (Preliminary). Version 1.0. UCAR/NCAR - Earth Observing Laboratory. DOI: doi:10.5065/D6M906SD., https://data.eol.ucar.edu/dataset/13.524.

Steiner, N. S., Lee, W. G., and Christian, J. R. (2013). Enhanced gas fluxes in small sea ice leads and cracks: Effects on CO 2 exchange and ocean acidification. *Journal of Geophysical Research: Oceans*, 118(3):1195–1205, ISSN: 21699291, DOI: 10.1002/jgrc.20100.

Stern, H. and Lindsay, R. (2000). Opening and closing rates.

TAMU/UMD (2020). ERDDAP - SODA - POP 2.2.4 Monthly Means, 1871-2010 (At Depths). https://coastwatch.pfeg.noaa.gov/erddap/griddap/hawaii_d90f_20ee_c4cb.html.

Thorndike, A. S., Rothrock, D. A., Maykut, G. A., and Colony, R. (1975). The thickness distribution of sea ice. *Journal of Geophysical Research*, 80(33):4501–4513, ISSN: 0148-0227, DOI: 10.1029/jc080i033p04501.

Tsamados, M., Feltham, D., Petty, A., Schroeder, D., and Flocco, D. (2015). Processes controlling surface, bottom and lateral melt of Arctic sea ice in a state of the art sea ice model. *Philosophical Transactions of the Royal Society A: Mathematical, Physical and Engineering Sciences*, 373(2052):20140167, ISSN: 1364-503X, DOI: 10.1098/rsta.2014.0167.

Tschudi, M. A., Meier, W. N., and Stewart, J. S. (2019). An enhancement to sea ice motion and age products. *The Cryosphere Discuss*, DOI: 10.5194/tc-2019-40.

Uttal, T., Curry, J. A., McPhee, M. G., Perovich, D. K., Moritz, R. E., Maslanik, J. A., Guest, P. S., Stern, H. L., Moore, J. A., Turenne, R., Heiberg, A., Serreze, M. C., Wylie, D. P., Persson, O. G., Paulson, C. A., Halle, C., Marison, J. H., Wheeler, P. A., Makshtas, A., Welch, H., Shupe, M. D., Intrieri, J. M., Stamnes, K., Lindsey, R. W., Pinkel, R., Pegau, W. S., Stanton, T. P., and Grenfeld, T. C. (2002). Surface heat budget of the arctic ocean. *Bulletin of the American Meteorological Society*, 83(2):255–275, ISSN: 00030007, DOI: 10.1175/1520-0477(2002)083<0255:SHBOTA>2.3.CO;2.

Vancoppenolle, M., Meiners, K. M., Michel, C., Bopp, L., Brabant, F., Carnat, G., Delille, B., Lannuzel, D., Madec, G., Moreau, S., Tison, J. L., and van der Merwe, P. (2013). Role of sea ice in global biogeochemical cycles: Emerging views and challenges. *Quaternary Science Reviews*, 79:207–230, DOI: 10.1016/j.quascirev.2013.04.011.

Wang, Q., Danilov, S., Jung, T., Kaleschke, L., and Wernecke, A. (2016). Sea ice leads in the Arctic Ocean: Model assessment, interannual variability and trends. *Geophysical Research Letters*, 43(13):7019–7027, ISSN: 00948276, DOI: 10.1002/2016GL068696.

West, A. E., McLaren, A. J., Hewitt, H. T., and Best, M. J. (2016). The location of the thermodynamic atmosphere-ice interface in fully coupled models - A case study using JULES and CICE. *Geoscientific Model Development*, 9(3):1125–1141, ISSN: 19919603, DOI: 10.5194/gmd-9-1125-2016.

Wilchinsky, A. V., Heorton, H. D. B. S., Feltham, D. L., and Holland, P. R. (2015). Study of the Impact of Ice Formation in Leads upon the Sea Ice Pack Mass Balance Using a New Frazil and Grease Ice Parameterization. *Journal of Physical Oceanography*, 45(8):2025–2047, ISSN: 0022-3670, DOI: 10.1175/JPO-D-14-0184.1.

Yao, Y., Huang, J., Luo, Y., and Zhao, Z. (2016). Improving the WRF model's (version 3.6.1) simulation over sea ice surface through coupling with a complex thermodynamic sea ice model (HIGHTSI). *Geoscientific Model Development*, 9(6):2239–2254, ISSN: 19919603, DOI: 10.5194/gmd-9-2239-2016.

A Appendices

A.1 Mass balance sites

A detailed description on the mass balance sites where Perovich et al. (2003) installed gauges and ablation stakes to measure snow and ice depth is given below in Table A.1. The locations of the mass balance sites are visualized in Figure A.1

Site	Number of gauges installed	Number of yearlong gauges	Temperature measurements	Description
Pittsburg	5	4	yes	Relative thick multiyear ice
The Ridge	20	14	yes	Young ridge that probably formed in the spring of 1997
Quebec 1	7	1	yes	Undeformed ice with an initial thickness of 0.85 cm
Quebec 2	4	7	yes	1.75 m thick hummock
Seattle	29	10	yes	Ponded area with nearby hummocks
Mainline	16	6	no	50m long line with undeformed and ponded multiyear ice
Tuk	22	17	yes	Old consolidated ridge
Atlanta	10	6	no	45-m long line with ponded and unponded multiyear ice
Doghouse	4	0	no	Thick multiyear ice
Sarah's Lake	6	0	no	First-year ice with adjacent lead
Baltimore	12	7	yes	First-year ice with adjacent multiyear ice and a rubble zone

Table A.1 | Summary of the ice mass balance measurement sites. Based on Table 1 in Perovich et al. (2003)

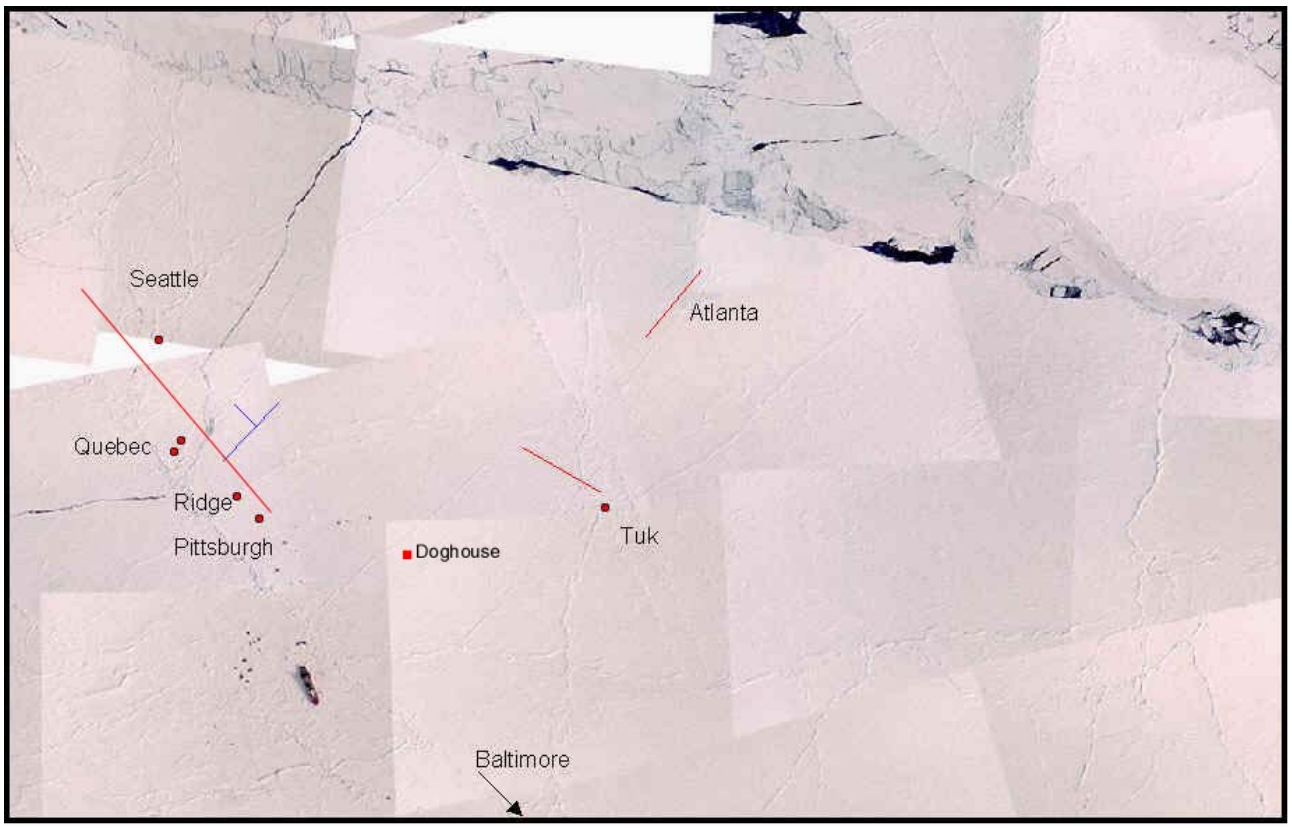

Figure A.1 | Aerial picture from May 17th 1998 with locations of the SHEBA mass balance sites described in Table A.1. (Perovich et al., 2003).

A.2 Observed ice temperature profiles

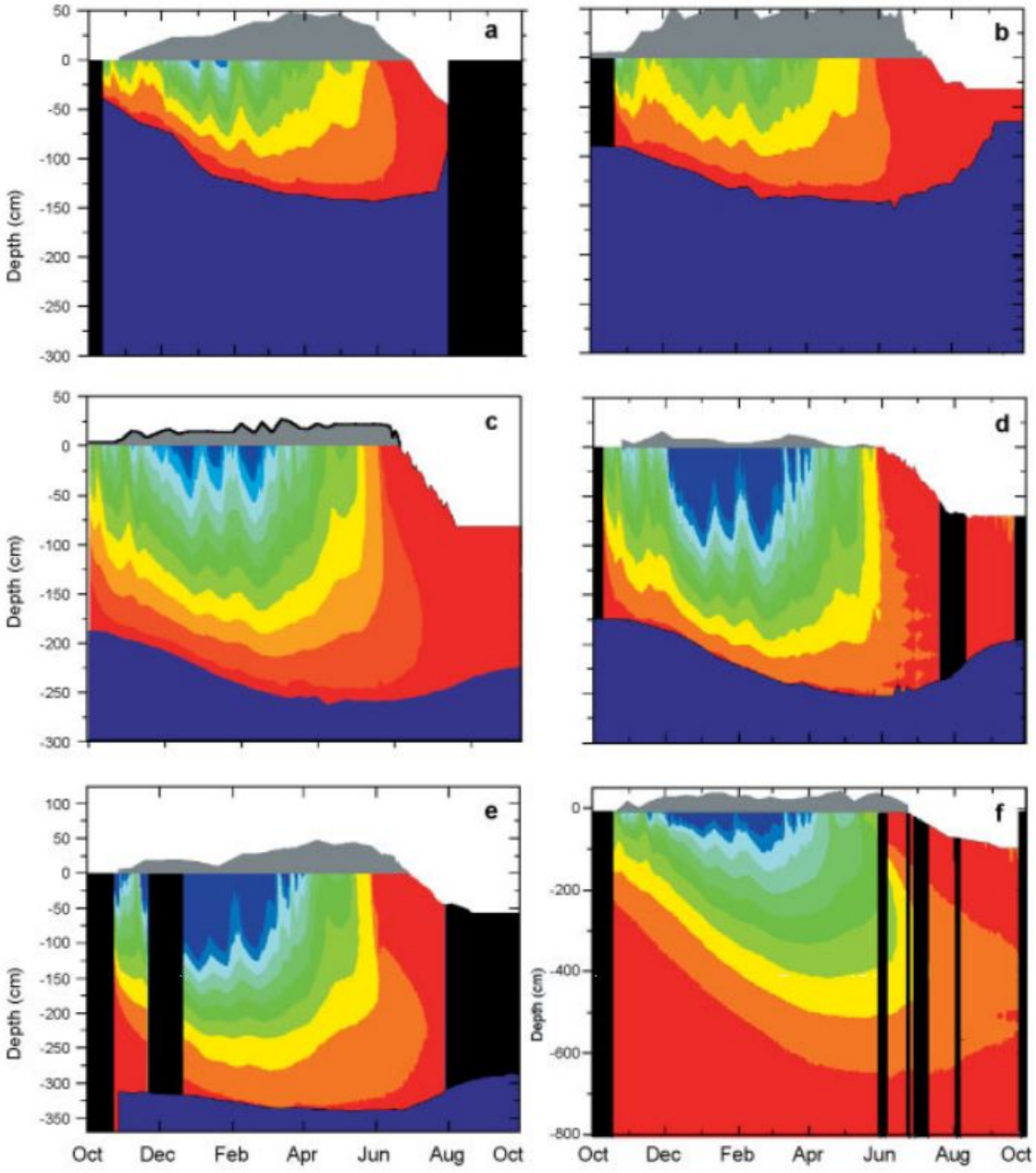

Figure A.2 | Temporal evolution of sea ice temperatures for the different mass balance sites. **a)** Baltimore, **b)** Seattle , **c)** Pittsburg, **d)** Quebec 2, **e)** Tuk, **f)** The Ridge. Color contours show the ice temperatures with blue representing cold (-20 °C) and red warm (0 °C) temperatures. From Perovich and Elder (2001)

A.3 Ice categories in the OPEN experiment

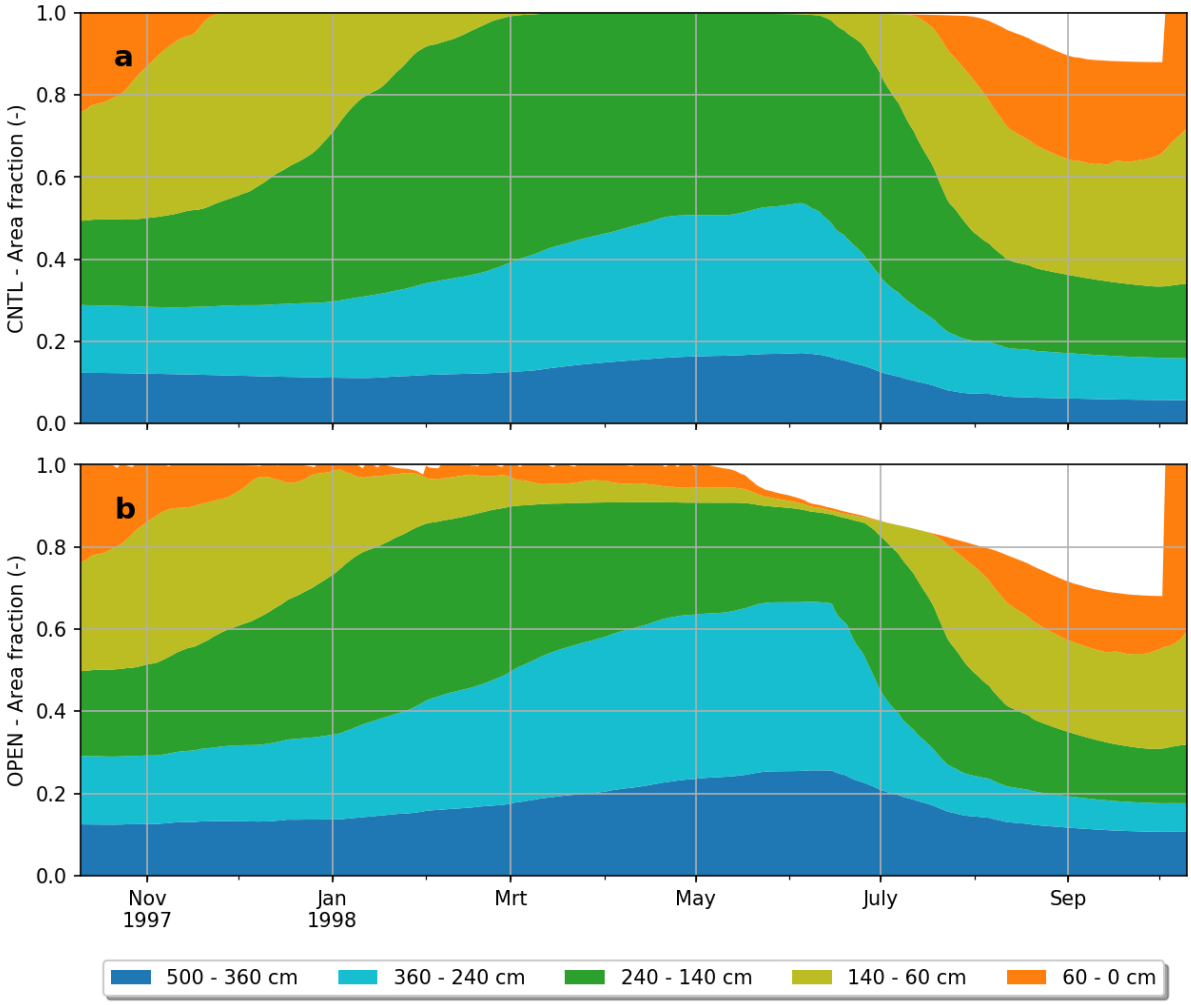

Figure A.3 | Simulated area fraction of each ice categories for a) OPEN and b) CNTL. In the legend the ice thickness boundaries of each category are given, where dark blue represents the thickest ice and orange the thinnest ice category.

A.4 Meteorological forcing data sets

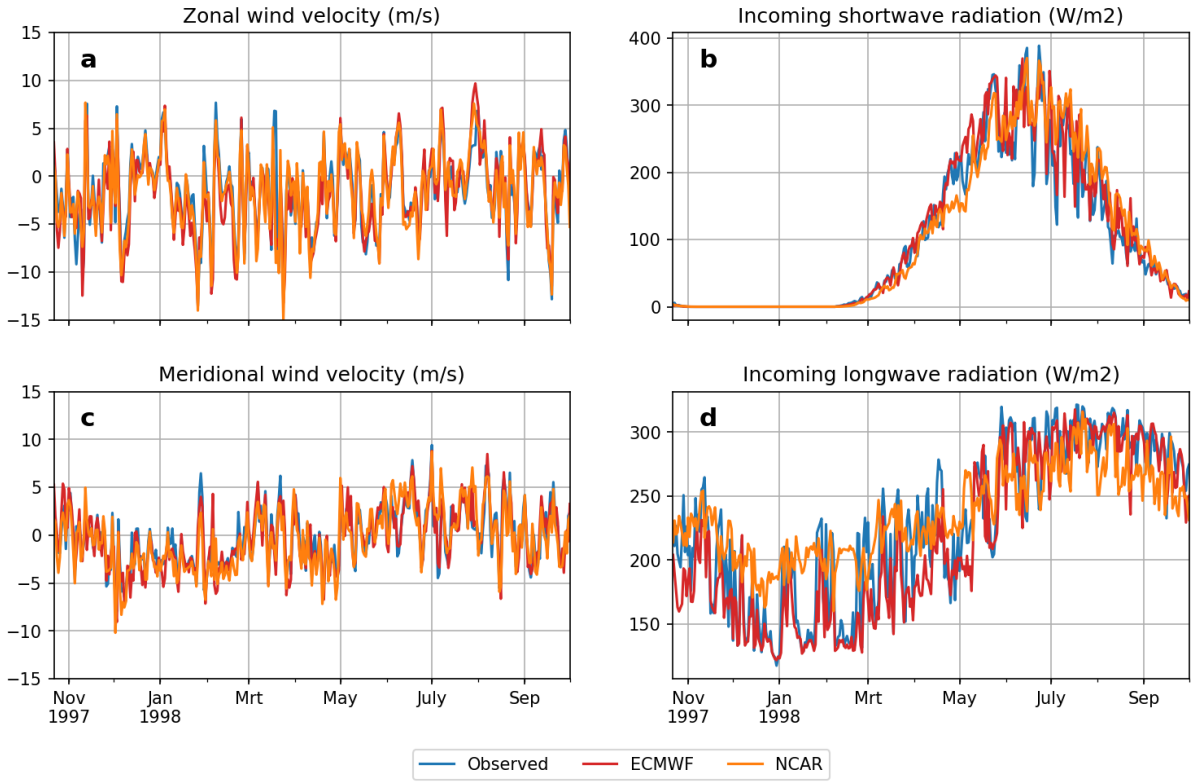

Figure A.4 | Atmospheric forcing fields from different forcing data sets. In blue the atmospheric measurements from the SHEBA campaign, used to force the CNTL Icepack run. Red shows the ECMWF column model output for the SHEBA location. In orange is shown the NCAR data used to force CICE, for the gridcell closest to the SHEBA expedition. On the x-axis is shown the day of the year since January 1st 1997.

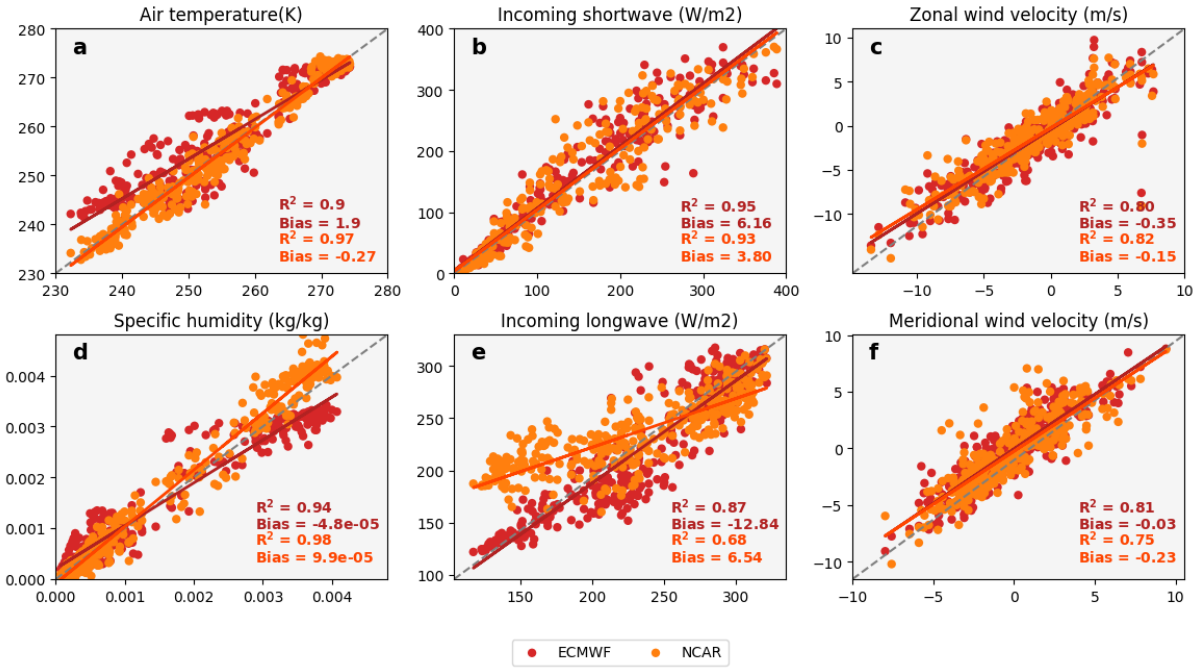

Figure A.5 | Correlation between the model atmospheric fields on the y-axis and measured atmospheric fields from the SHEBA campaign (x-axis). For both model atmospheric fields (ECMWF in red and NCAR in orange) the regression line with it's R-squared is shown. The bias represents the average difference between the observations and models.

A.5 Seasonal ice concentrations

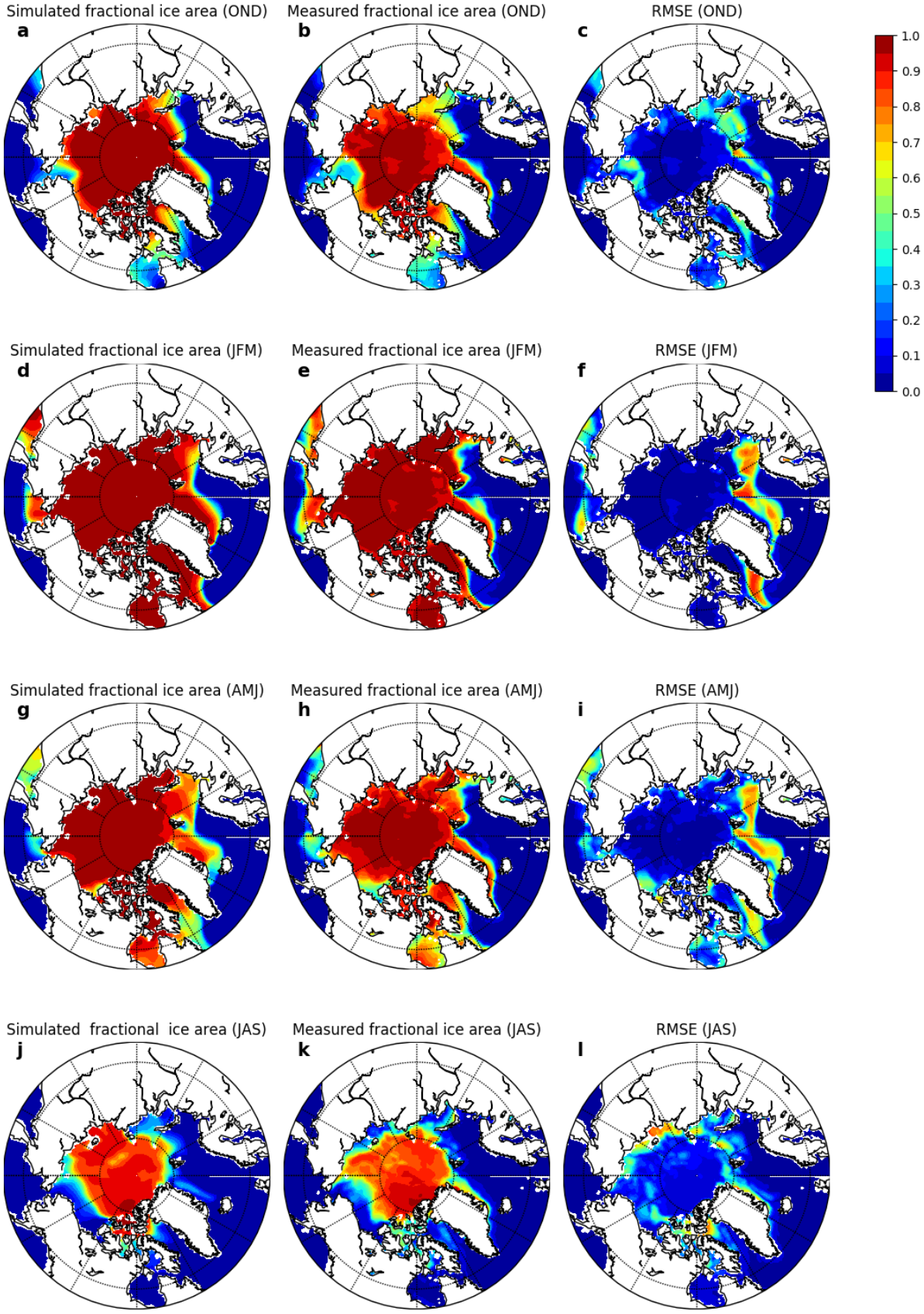

Figure A.6 | Comparison of modelled vs observed seasonal averaged ice concentrations. Seasonal averages are calculated for the period Oct 1th 1997 - Sept 30th 1998. All left figures show CICE simulations, with in the middle the observed ice concentration from OSI SAF (2016) and on the right the RMSE between observations and simulation.

A.6 Surface energy balance

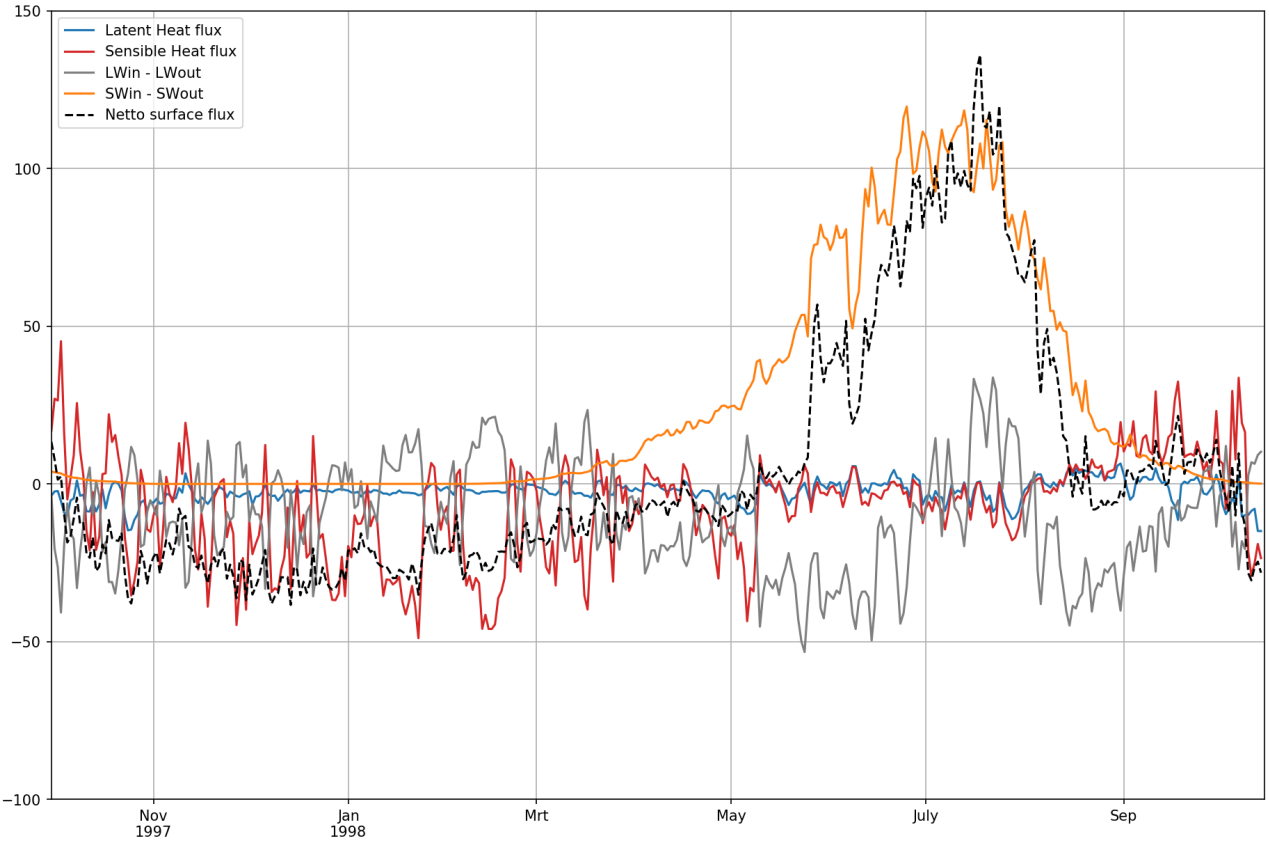

Figure A.7 | Surface energy balance components along the SHEBA-trajectory. The fluxes are given for the CICE simulation using a 90-days restoring timescale in W/m^2.

A.7 Impact SST restoring on Arctic ice pack

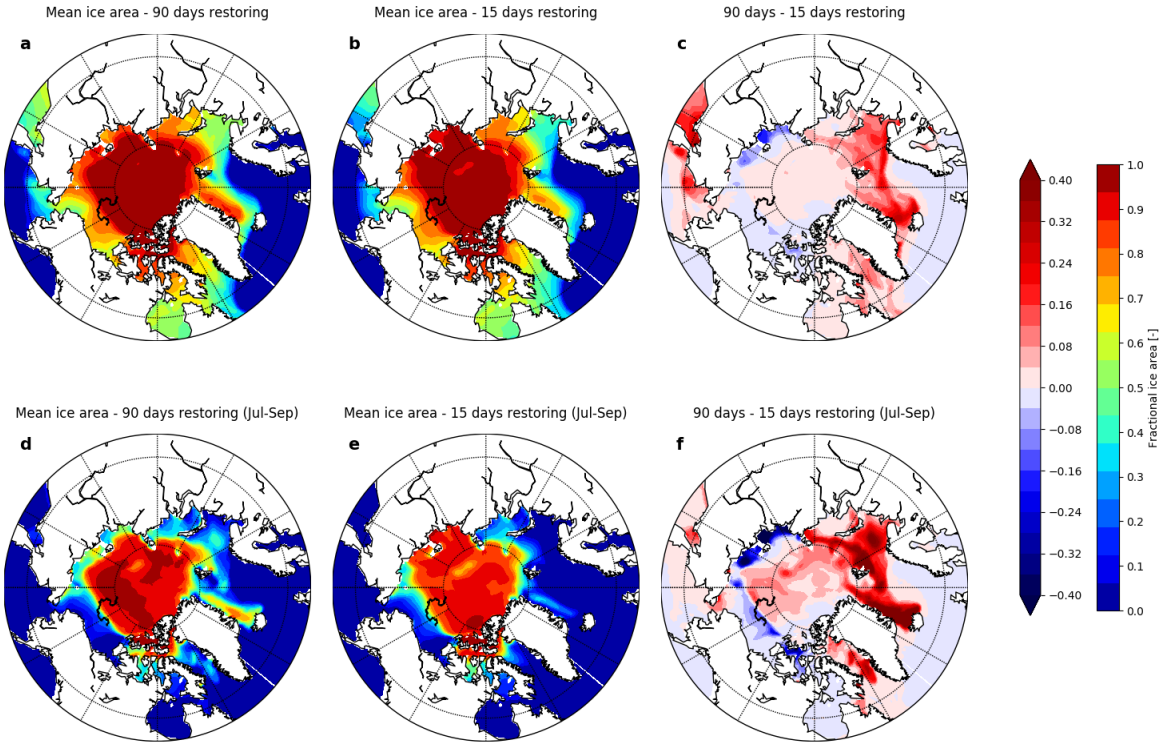

Figure A.8 | Simulated mean fractional ice area for a run using a long (90 days) and short (15 days) restoring timescale. (a,b) show the ice concentration over the SHEBA period and (**d,e**) for July until September.**c)** and **f)** show the difference in ice area between the two simulations. With a black line the SHEBA trajectory is plotted in each map.

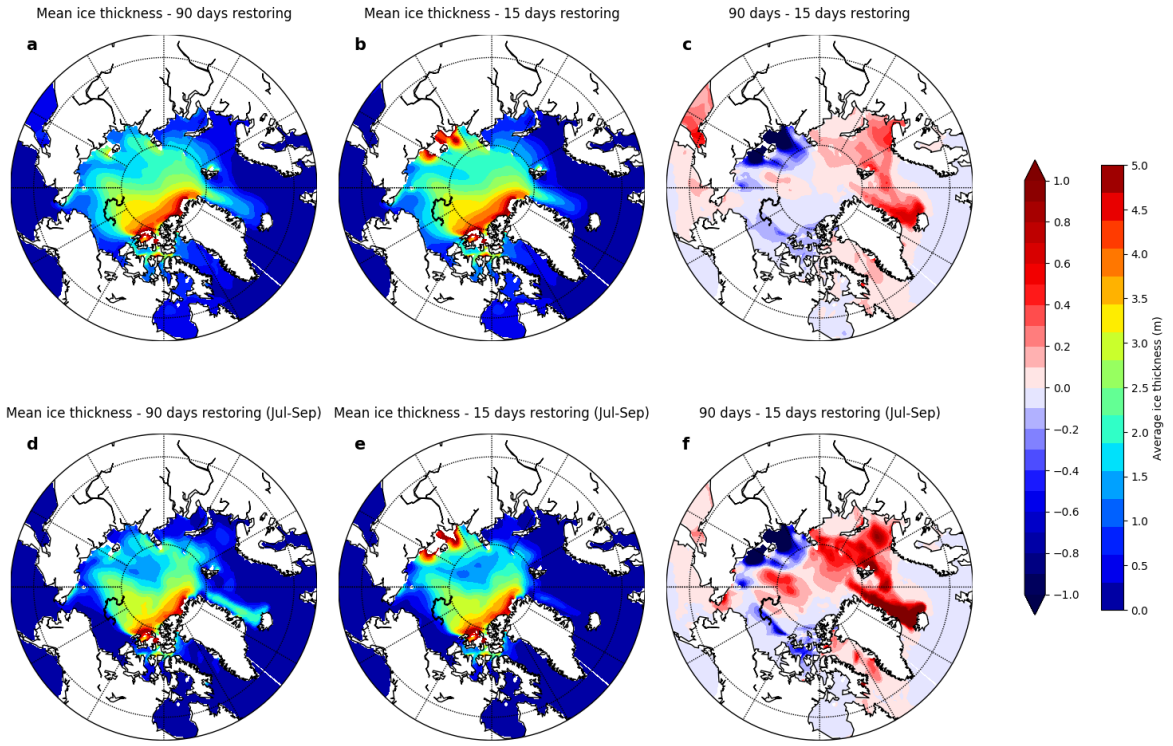

Figure A.9 | Simulated mean ice thickness for a run using a long (90 days) and short (15 days) restoring timescale. (a,b) show the mean ice thickness over the SHEBA period and (**d,e**) for July until September.**c)** and **f)** show the difference in ice thickness between the two simulations. With a black line the SHEBA trajectory is plotted in each map.

A.8 Impact melt pond schemes on Arctic ice pack

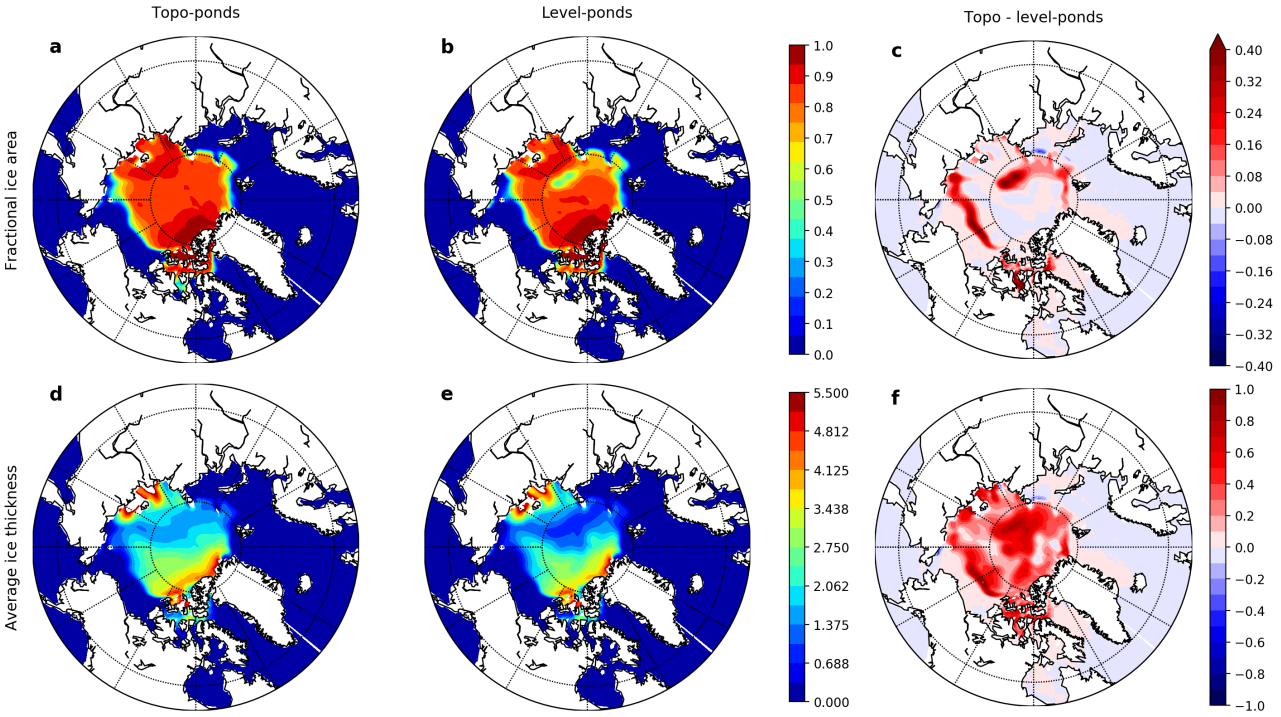

Figure A.10 | September 1998 simulated fractional ice area and ice thickness for a simulations using the topo-pond scheme and the level-pond scheme. a,b) give the fractional ice area and **c)** the difference in fractional ice area between the two simulations. Similarly, **d,e)** show the average ice thickness and **f** gives the difference in ice thickness between the two simulations.